ISSN 2078-7405

МІНІСТЕРСТВО ОСВІТИ ТА НАУКИ УКРАЇНИ

РІЗАННЯ ТА ІНСТРУМЕНТИ

В ТЕХНОЛОГІЧНИХ СИСТЕМАХ

103 ' 2025

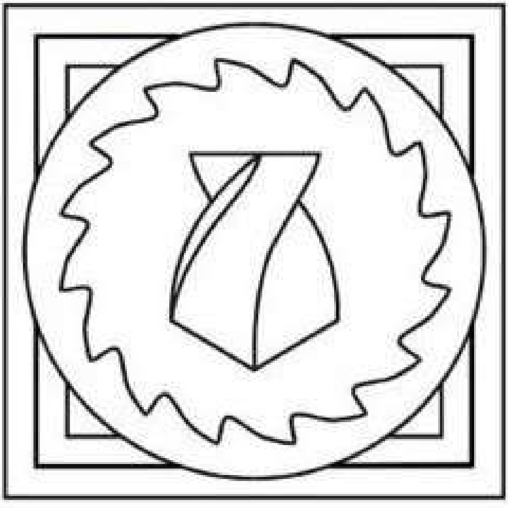

МІНІСТЕРСТВО ОСВІТИ ТА НАУКИ УКРАЇНИ

НАЦІОНАЛЬНИЙ ТЕХНІЧНИЙ УНІВЕРСИТЕТ
«ХАРКІВСЬКИЙ ПОЛІТЕХНІЧНИЙ ІНСТИТУТ»

Ministry of Education & Science of Ukraine
National Technical University
«Kharkiv Polytechnic Institute»

РІЗАННЯ ТА ІНСТРУМЕНТИ в технологічних системах

CUTTING & TOOLS IN TECHNOLOGICAL SYSTEM

Збірник наукових праць
Collection of scientific papers

Заснований у 1966 р. М. Ф. Семко
Found by M. F. Semko in 1966

ВИПУСК № 103
Edition № 103

Харків НТУ «ХПІ» – 2025 – Kharkiv NTU «KhPI»

ISSN (print) 2078-7405
УДК 621.91

Ідентифікатор медіа R30-02559, згідно з рішенням Національної ради
України з питань телебачення і радіомовлення від 27.07.2023 р. №598
Друкується за рішенням Вченої ради НТУ "ХПІ",
протокол № 13 від 26 грудня 2025 р.

У збірнику представлені наукові статті, в яких розглядаються актуальні питання в області механічної обробки різних сучасних матеріалів із застосуванням високопродуктивних технологій, нових методик, вимірювальних приладів для контролю якості оброблених поверхонь і високоефективних різальних інструментів. Розглядаються аспекти оптимізації та математичного моделювання на різних етапах технологічного процесу.

Для інженерів і наукових співробітників, що працюють в області технології машинобудування, різання матеріалів, проектування різальних інструментів в технологічних системах.

Збірник наукових праць «Різання та інструменти в технологічних системах» включений в Перелік фахових видань України категорії «Б», наказ МОН України від 17.03.2020 р., № 409

Різання та інструменти в технологічних системах/Cutting and Tools in Technological Systems: Збірник наукових праць. – Харків: НТУ «ХПІ», 2025. – Вип. 103. – 155 с.

Адреса редакційної колегії: вул. Кирпичова, 2, Харків, 61002, Національний технічний університет «Харківський політехнічний інститут», кафедра «Інтегровані технології машинобудування» ім. М.Ф. Семка, тел. +38 (057) 706-41-43.

УДК 621.91
Матеріали відтворені з авторських оригіналів
НТУ «ХПІ», 2025

ISSN 2078-7405 Cutting & Tools in Technological System, 2025, Edition 103

UDC 621.923: **doi:10.20998/2078-7405.2025.103.01**

DIAMOND ABRASIVE TREATMENT: TRIBOLOGICAL ASPECT (REVIEW OF MODERN RESEARCH)

Valerii **Lavrinenko**[1][0000-0003-2098-7992], Volodymyr **Solod**[2][0000-0002-7516-9535], Yevgeniy **Ostroverkh**[3][0000-0002-8926-1324], Vladimir **Fedorovich** [3][0000-0001-7015-8653], Predrag **Dašić**[4][0000-0002-9242-274X]

[1]V. Bakul Institute for Superhard Materials NAS Ukraine, Kyiv, Ukraine
[2]Dniprovsk State Technical University, Kamianske, Ukraine
[3]National Technical University «Kharkiv Polytechnic Institute», Kharkiv, Ukraine
[4]Engineering Academy of Serbia (IAS), Belgrade, Serbia
lavrinenko@ism.kiev.ua

Received: 29 October 2025 / Revised: 16 November 2025 / Accepted: 29 November 2025 / Published: 15 December 2025

Abstract. *The importance of developments to overcome friction and wear is largely due to the fact that the energy consumed by the manufacturing industry is almost a third of the total energy consumed. That is, the tribological aspect in the processes of diamond-abrasive processing is quite significant and must be taken into account. Recently, new modern developments have appeared in the literature that somewhat clarify this direction, both from the point of view of the diamond abrasive tool and the tribological behavior of various diamonds, including those with coatings. It is these developments that are covered further in our review of modern publications. Additive manufacturing (AM) methods have significant advantages for obtaining individual products and prototypes, allow to reduce costs, and also speed up the release of products to the market. Nowadays, this direction has begun to be used for diamond-abrasive tools. Of course, new binders for the working layer of the diamond tool have been developed for such energy-efficient AM technology. It is shown that the cutting forces and friction coefficients of microtextured diamond tools are significantly reduced. The tribological behavior of diamonds against various materials is fundamental for their use in the abrasive and bearing industries. It has been proven that, in comparison with ordinary diamond grains, porous diamond grains with an increased number of microedges effectively reduce the cutting force and heat generation. It is shown that the application of the effect of further mechanochemical influence during the coating of diamond abrasives, both on the diamond-bond boundary and on the contact of the surface of the diamond grain with the processed material, allows to increase the efficiency of the use of the diamond-abrasive tool. Attention is drawn to what kind of impurities are introduced into the contact zone during diamond-abrasive processing to change the tribological parameters. At the same time, the most widely used is h–BN, which with a layered crystal structure is one of the types of effective solid lubricants, especially at elevated temperatures. Attention has been paid to emerging materials such as graphene oxide and carbon dots (CD), a kind of carbon-based nanomaterials, which have been widely used as highly effective lubricant additives.*

Keywords: *diamond abrasive treatment; tribological behavior; diamond tool; diamonds; coatings; solid lubricants; graphene oxide.*

At one time, in the article [1], the energy consumption in diamond abrasive processing processes was analyzed and it was proved that the share of friction energy in the total processing energy can be from 17 to 45 % for the processing of hard alloys, from 29 to 42 % for the processing of non-tungsten solids alloys, from 20 to 29 % when grinding oxide-carbide ceramics and from 52 to 98 % when grinding oxide ceramics. The importance of developments to overcome friction and wear is also shown in a modern article [2], where it is indicated that the energy consumed by the manufacturing industry makes up almost a third of the total energy consumed. Wherein 20 % of the energy is used to overcome friction, and 14 % of the energy loss is caused by friction that is a wear-related energy loss, including the energy for making new parts and equipment downtime. In addition, taking into account the cost of maintenance work due to wear, the overall cost of wear represents 35 % of the cost of friction. The industrial production field causes a lot of energy consumption due to overcoming friction and wear. That is, the tribological aspect in the processes of diamond-abrasive processing is quite significant and must be taken into account. Recently, new modern developments have appeared in the literature that somewhat clarify this direction, both from the point of view of the diamond abrasive tool and the tribological behavior of various diamonds, including those with coatings, especially such coatings that contain additives to reduce friction, primarily the newest – graphene and h-BN. It is precisely these developments that we will highlight in our review of modern publications.

DIAMOND ABRASIVE TOOL WITH CHANGED TRIBOLOGY CHARACTERISTICS

The article [3] presents a new, modern, in contrast to the traditional, but energy-consuming, technology of pressing and sintering, a strategy for manufacturing grinding tools with conventional crystalline structure by 3D printing using multi-jet fusion technology (MJF), and five structures were selected to evaluate its feasibility and achieve grinding performance. The analysis of the results shows that the crystalline structure ensures the same macroscopic rigidity of the tools and introduces a microscopic anisotropy of compliance (Fig. 1). The crystalline structure resulted in a reduction of the grain pullout ratio by more than 82.60%, and also facilitated adhesion and prevented the abrasive layer from falling off, resulting in longer tool life. In addition, the grinding tools with crystalline structure achieved better material removal capacity, lower surface roughness, and higher energy efficiency, and they used only 29.06% to 36.22% of the materials compared to the tool with dense structure. It is noteworthy that the material removal rate of a tool with a star structure can reach 94.72% of a tool with a dense structure.

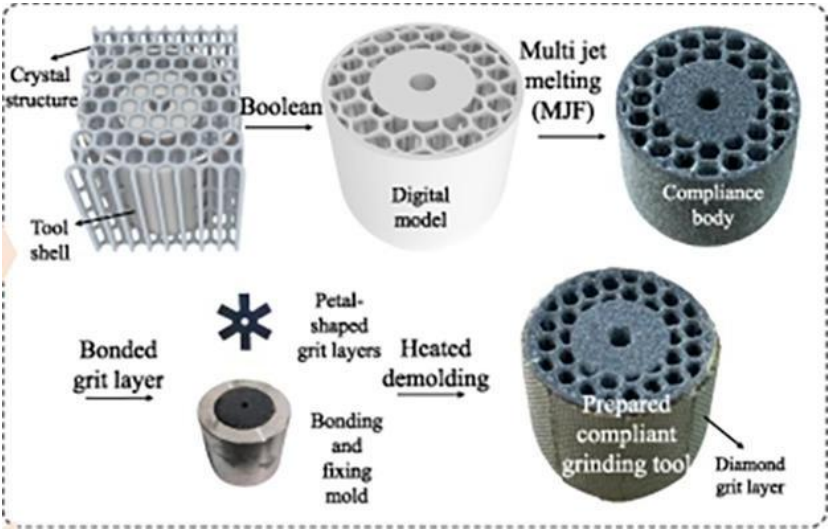

Fig. 1. Schematic sequence of obtaining a diamond tool with a crystal structure by the method of 3D printing [3].

Of course, such an energy-efficient technology of additive manufacturing (AM) also requires new binders for the working layer of the diamond tool. AM production methods have significant advantages for obtaining individual products and prototypes, allow to reduce costs, as well as accelerate the release of products to the market. The purpose of the article [4] was to study binders based on acrylate resin with different mechanical and thermal characteristics for 3D printing of grinding wheels. A noticeable improvement in grinding characteristics was achieved due to the use of a heat-resistant bond, both for mild aluminum and hardened steel. It was established that the use of a bond with higher mechanical and thermal characteristics allows for good grain retention at elevated temperatures, which contributes to reducing the grinding effort (up to 58 % and 18 % for soft and hard metals, respectively). As a result, it allows you to significantly extend the service life of the tool, for example, up to 80 % for hardened steel, and also to increase the accuracy of dimensions.

To improve the retention of diamond grains in the working layer of a diamond tool in the study [5], the surface of diamond grains was modified by applying a layer of SiO_2 by the method of isothermal hydrolysis. The results show that due to the presence of hydrate ions on the surface of the diamond grains, a thin film of SiO_2 was uniformly grafted to the surface of the diamond and this significantly increased the adhesion to the bond.

In order to mitigate the problems of low processing quality, short tool life, and low processing efficiency in the processing of 2.5D needle-like C/SiC composites, a bionic idea was adopted in research [6] to develop a new single-layer galvanic ordered tool (Fig. 2). The influence of ordered grinding wheels on surface roughness, microstructure, grinding force, grinding temperature and wear conditions was investigated. Compared with the unordered grinding wheel, the A-type and B-type ordered grinding wheels can reduce the surface roughness of the bottom surface of the C/SiC composite groove by 40.7 % and 35.8 %, respectively. In addition, they can reduce the grinding force Fy to 68.3 % and 53.2 %, respectively, and the grinding force Fz to 70.4 % and 46.9 %, respectively.

Fig. 2. Variants of the ordered end layer of a single-layer galvanic tool based on the bionic idea [6].

In work [7], another new production process was used for the development of a single-layer diamond wheel using bulk metallic glass (BMG) as a matrix and diamond particles as abrasives. BMG effectively prevents graphitization and damage to diamond abrasives due to the lower forming temperature. The coating of titanium (Ti) on the surface of diamond abrasives contributed to the formation of diffusion between the two components, creating a mechanical bond at the BMG-diamond interface. In addition, the fabricated BMG-bonded single-layer diamond wheel was preferentially worn uniformly instead of abrasives falling out during grinding of Al_2O_3 ceramics. Compared to modern electroplated grinding wheels, the developed diamond wheel demonstrated a reduction in normal and tangential grinding forces by 32.64 % and 35.86 %, respectively, and an increase in the grinding coefficient by

28.22 %, making it an excellent solution for grinding conditions of hard and brittle materials.

Grinding of railway rails can effectively remove their defects, such as cracks and corrugations, to ensure the safety and stability of railway vehicles, because the heat generated during grinding becomes a critical cause of pre-fatigue or burn on the rail surface. In work [8] rail grinding wheels with different porosity were produced. The results show that the pore structure can reduce the previous fatigue caused by grinding. Importantly, grinding efficiency improves and grinding effort/heat decreases with increasing porosity (Fig. 3). That is, such softer porous wheels significantly reduce friction and temperature in the grinding zone.

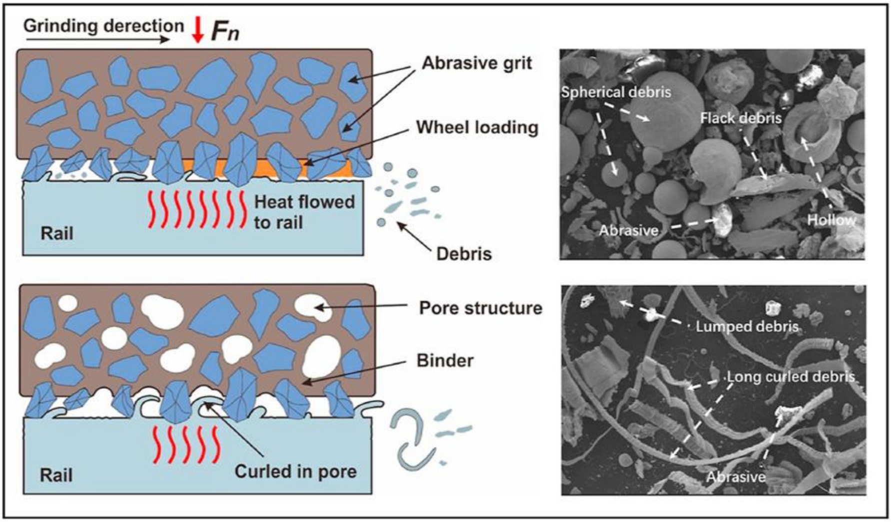

Fig. 3. Comparison of the structure and differences of chips when using solid and porous wheels for grinding rails [8].

Soft tool grinding is known for its advantages, such as large contact areas, conforming to curved surfaces based on deformation and effective vibration absorption, resulting in increased efficiency and good surface quality. In the article [9], a model of elastic extrusion was proposed, developed to calculate the pressure distribution between soft tools and hard complex surfaces of the processed workpiece (Fig. 4). The proposal lays new foundations for setting parameters during precise grinding with a soft tool.

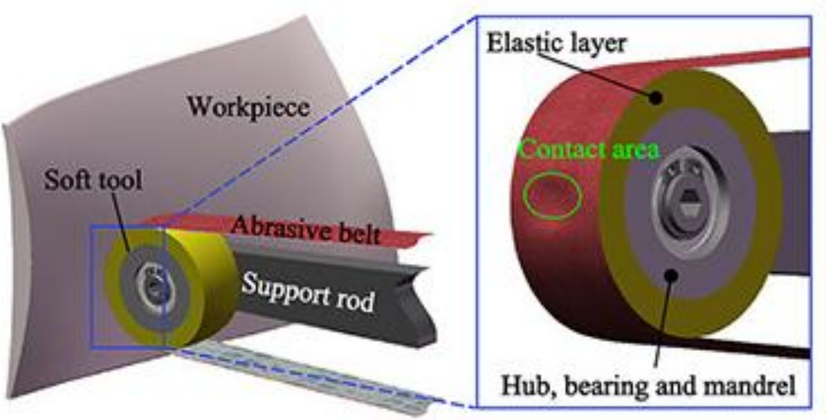

Fig. 4. Towards an elastic model of elastic extrusion in contact between soft tools and complex hard surfaces [9].

At the same time, discontinuity and elasticity can cause friction force fluctuations, which is analyzed in the article [10]. A real-time Coefficient of Friction (COF) analysis method combined with an *in-situ* contact area measurement method is used here to determine friction behavior and material removal. The results show that the material removal rate (MRR) is not correlated with the average friction coefficient, but shows a strong relationship with the frictional force fluctuations, i.e. the intermittent sliding phenomenon. In addition, a wavy topography is observed on the treated surface, which is caused by the phenomenon of intermittent sliding.

The above indicates that, among other things, it is necessary to pay attention to the condition of the cutting edge, which performs the cutting process, which was done in the article [11]. An abrasive wheel for solid phase chemical mechanical polishing (SPCMP) and effective sharpening of the cutting edge of a carbide tool (WC–Co) was developed here. X-ray diffraction and electron backscatter diffraction measurements showed that the SPCMP method removes latent scratches from the surface of WC–Co materials applied by a diamond wheel. The 100 mm diameter grinding wheel developed for SPCMP was produced in a phenolic binder using green silicon carbide (GC) as the abrasive component. This made it possible to avoid the transition from the WC phase to the W2C phase during the processing of the hard alloy, and to provoke the oxidation of the WC phase and its removal by GC. When cutting with WC–Co tools with cutting edges sharpened by SPCMP treatment, the cutting resistance was low and the degree of wear was reduced. In addition, the cutting speed of WC–Co tools when cutting Ti–6Al–4V and Inconel 718 after SPCMP wheel sharpening was about two times higher than before SPCMP.

Similarly, diamond grains must be sharp in order to obtain good dry grinding performance. In the article [12], monocrystalline synthetic diamond grains with different strength and fragility were used for the development of diamond circles with a random and patterned distribution of grains (Fig. 5). Grinding wheels containing loose diamond grains with an irregular grain structure showed better results during dry grinding experiments on WC-6Co hard alloy than high-strength cubo-octahedral grains.

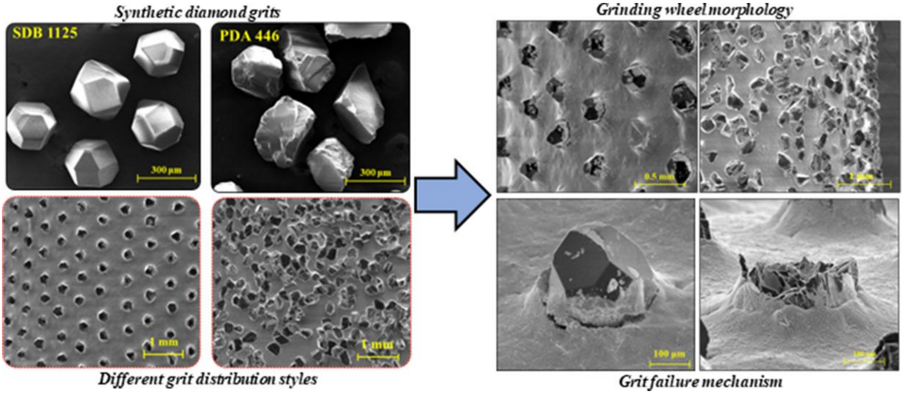

Fig. 5. High-strength (SDB 1125) and loose (PDA 446) diamonds in a single-layer tool and the difference in their destruction during grinding [12].

The article [13] presents a new grinding wheel containing the porous (loose) diamonds we mentioned above to improve ultra-precision processing. Thermochemical etching is used to obtain porous diamond grains with varying degrees of corrosion, and the cutting and wear mechanisms of these grains are investigated using MD modeling and scratch tests with individual grains. Compared to ordinary diamond grains, porous diamond grains with an increased number of microedges effectively reduce the cutting force and heat generation. It is interesting that the sizes of corrosion pores in the range from 2 to 5 µm reduce their damage during cutting. Conventional diamond grains are primarily damaged due to graphitization of the crystal surface and block crushing, while porous diamond abrasive grains are damaged primarily due to microcrushing and microfracture. Tests during final grinding of 4H-SiC showed that ordinary diamonds here give cracks and punctures on the polished surface. Meanwhile, diamonds with corrosion pores of 2 μm showed mostly ductile removal with minimal cracks and pitting. Diamond abrasives with corrosion pores of 5 μm also demonstrated satisfactory performance.

At the end of this part of the review, let's pay attention to the features of the latest processing methods with the use of additional influence on the processing process.

Elastic Emission Machining (EEM) is one of the most effective technologies for obtaining an ultra-smooth surface. A polishing particle is fed to a certain place on the surface of the part by means of a polishing wheel and enters into a chemical reaction with the workpiece, ensuring the removal of material. In the study [14], the mutual dynamic interaction between the polishing wheel and the suspension is considered in a three-dimensional state, and the rolling model is developed to analyze the energy transfer during the removal of atoms. The rolling model explains how a particle can disrupt the feedback of atoms on the workpiece surface to achieve material removal. The results of the study indicate that the energy needed to remove atoms is primarily supplied by the liquid. This understanding of the energy source provides valuable information for proposals for methods to increase material removal rates. Finally, in an experiment on surface polishing, the application of EEM leads to the retention of an ultra-smooth surface with an rms roughness of 0.1 nm, which demonstrates the excellent ability of EEM to effectively reduce surface roughness [14].

In the article [15], a new technology of dynamic friction polishing of diamonds with a low rotation speed using now ultraviolet irradiation is proposed. This method is based precisely on the effect of ultraviolet radiation and the surface of the diamond in combination with the friction between the diamond and the metal disc to realize material removal. The process of phase transformation and oxidation, which is facilitated by ultraviolet light, is the main mechanism for achieving effective material removal at low rotation speed (Fig. 6). That is, under the synergistic effect of ultraviolet light and frictional heating, the diamond can undergo oxidation and interaction with iron at a low rotation speed of 8 m/s and, finally, this allows to obtain an ultra-smooth diamond surface with a surface roughness of R_a=0.18 nm.

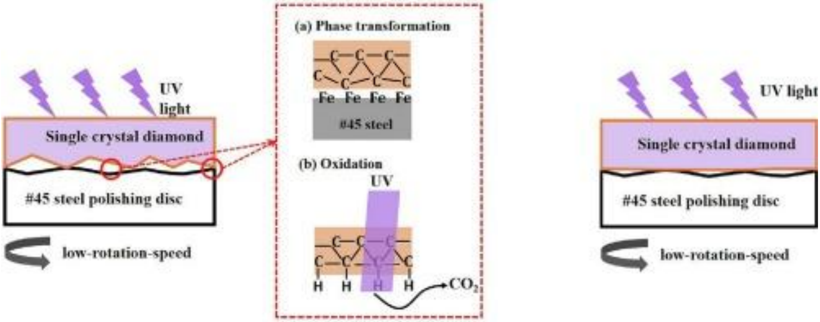

Fig. 6. Illustration of the mechanism for achieving effective diamond polishing when applying ultraviolet irradiation [15].

TRIBOLOGICAL BEHAVIOR OF DIAMONDS DURING DIAMOND ABRASIVE PROCESSING

The tribological behavior of diamonds against various materials is fundamental to their application in the abrasive and bearing industries. In the article [16], friction and wear on GCr15 steel and Si_3N_4 ceramics of two types of diamonds were investigated: HFCVD - hot filament chemical vapor deposition and PCD polycrystalline diamonds - sintered under high pressure and high temperature (HPHT). It was established (Fig. 7) that, firstly, the coefficient of friction (COF) increased with an increase in the roughness of the diamond surface; second, both the COF and wear rate (k) of the Si_3N_4 ceramic balls were generally lower than those of the GCr15 steel balls, except for the COF of the HFCVD sample; third, the wear rate (k) increased with increasing PCD grain size, which was accompanied by a decrease in residual cobalt content. As we can see from fig. 7 CVD diamond has the lowest coefficient of friction, and in terms of wear rate it is inferior only to polycrystalline diamond with a grain size in the structure of 2 µm.

Modified diamond tools (MDT) with the help of a focused ion beam (FIB) have to a certain extent reduced wear during dry single-point diamond turning, which was proved in the article [2]. The reason why MDT cutting performance is better than that of unmodified diamond tools is the reduced surface energy of modified diamonds. It was found that the implantation of Ga ions (Fig. 8) reduces the surface energy by 33% compared to pure diamond.

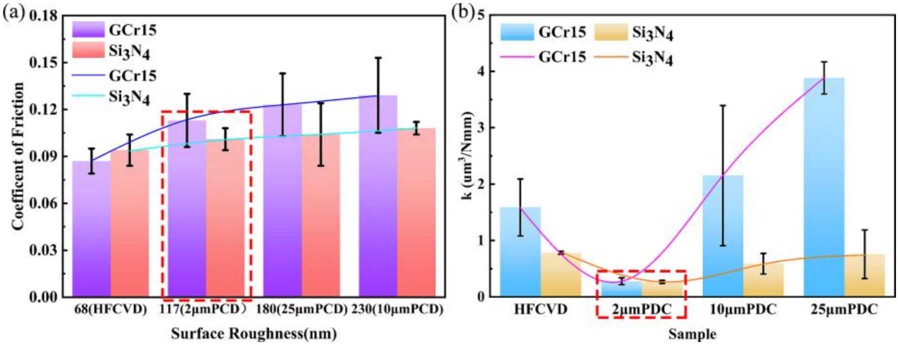

Fig. 7. Change in coefficient of friction (COF) of PCD and HFCVD samples with increasing roughness (a) and change in wear rate (k) of Si_3N_4 ceramic and GCr15 steel balls with increasing PCD grain size (b) [16].

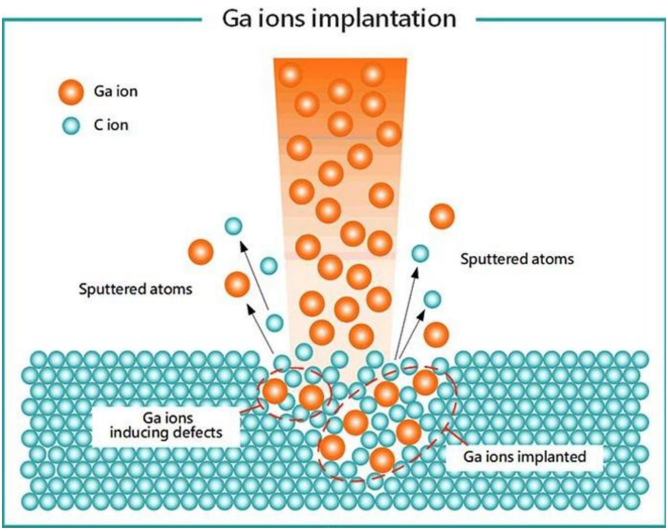

Fig. 8. Scheme of modification of the surface of a diamond tool using a focused ion beam [2].

Under conditions of high friction temperatures, polycrystalline diamond (PCD) can wear due to graphitization. PCD with cobalt removed and, as a friction pair, silicon nitride balls in the article [17] were selected for friction wear experiments at temperatures of 200, 300, and 400 °C, respectively (Fig. 9).

The results showed that the coefficient of friction and the rate of wear increase with increasing temperature. No graphitic phase was found by XRD, indicating that the cobalt pre-removal process itself can effectively inhibit the graphitization of polycrystalline diamond at high temperature. SEM images showed that increasing the temperature does not contribute to the formation of a friction film, which can increase the wear resistance of materials.

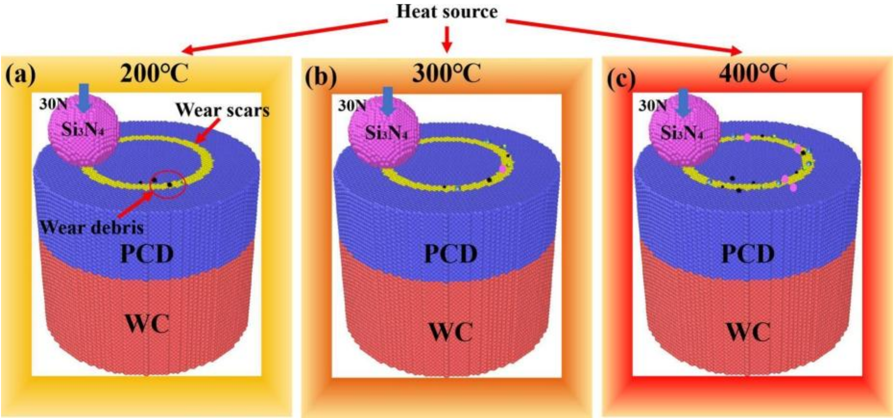

Fig. 9. Scheme of experiments on frictional wear and the difference in wear debris on wear scars [17].

In [18], the high-entropy alloy (HEA) $FeCoCrNiB_{0.15}$ and the diamond composite based on it were produced by the spark plasma sintering (SPS) method at a temperature of 950 °C. For comparison, samples of $FeCoCrNiMo_{0.15}$ and its diamond composite were made and their friction and wear behavior on Si_3N_4 balls under conditions of dry sliding in air on a ball-on-disk tester was compared (Fig. 10). The results showed that in both HEAs, a chromium-rich phase separated from the metastable matrix was observed on the friction surface. The wear resistance of $FeCoCrNiB_{0.15}$ was higher than that of the $FeCoCrNiMo_{0.15}$ alloy, and the Si_3N_4 grinding speed of the $FeCoCrNiB_{0.15}$/diamond composite was higher than that of the $FeCoCrNiMo_{0.15}$/diamond composite. This study shows that the boron-doped HEA matrix in diamond composites is a promising candidate for the manufacture of diamond tools with a long service life and high processing efficiency.

As we have already indicated above, the rubbing behavior of raw surfaces of polycrystalline diamond (PCD) is important for its application. The article [19] shows the influence of the water environment on this. Here, the interfacial capillary adhesion force at the contact surfaces and its effect on the frictional response between the colloidal microsphere and rough PCD films before and after electrochemical corrosion under conditions of immersion in water, low relative humidity, and humid air are quantified (Fig. 11). The combined results convincingly indicate that the observed increase in the frictional force on electrochemically corroded PCD surfaces (for microcrystalline MCD and nanocrystalline NCD) is regulated by the strengthening of the capillary effect on the contact surface, which depends on the hydrophilicity of the surface and the humidity of the environment. Compared to MCD, NCD surfaces, which have a larger intercrystalline area, experience more intense electrochemical corrosion and exhibit higher observed frictional forces as a result of lower surface roughness and greater surface hydrophilicity. The increased adhesion force of the capillaries contributes to normal loading and reduces the interfacial gap (increases the contact area of the solid body), thus increasing the frictional force. That is, the presence of water under conditions of high humidity changes the contact conditions, increasing the force of friction.

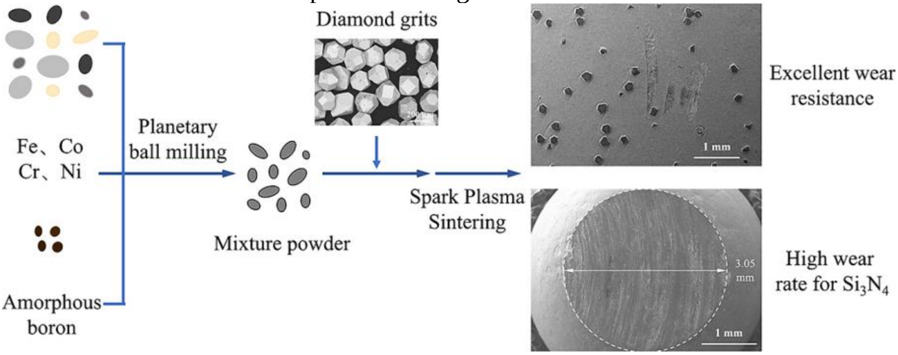

Fig. 10. Scheme of obtaining a diamond composite based on the high-entropy $FeCoCrNiB_{0.15}$ alloy [18].

As we can see above, the microrelief of the diamond surface plays an important role in evaluating its frictional characteristics. In [20], the effect of special microtextures on the frictional and cutting characteristics of monocrystalline diamond tools was considered. Four types of microtextures, including an array of straight grooves, a concentric circular texture, a ring sequence, and a mesh texture, were created on their front surface using a femtosecond laser. The results of the experiments showed that the cutting forces and friction coefficients of the microtextured diamond tools decreased significantly, except for the concentric round texture. At the same time, the cutting characteristics of monocrystalline diamond tools were significantly improved.

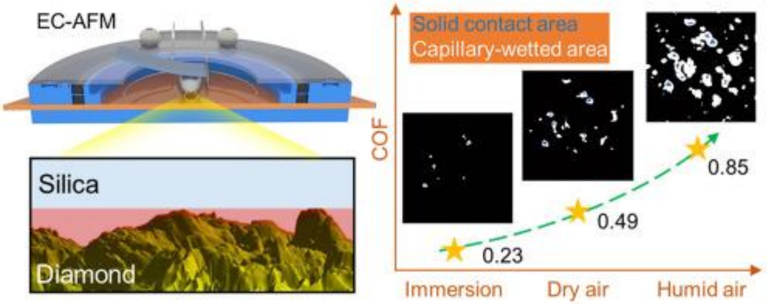

Fig. 11. Scheme of the electrochemical-atomic-force microscopy (EC-AFM) installation in section and evaluation of the friction coefficient for the conditions of submerged state, low and high humidity [19].

At the end of this part of the review, let's pay attention to the shape of diamond grains during abrasive processing of brittle materials. Abrasive processing can be simplified by presenting a series of scratches with indenters of various shapes. In the article [21], a model of the stress field caused by scratches was built to analyze the behavior of cracking when brittle materials are scratched. The model takes into account conical, pyramidal and spherical (CPS) indenters. The results show that the scratch load is reduced when a sharper indenter or a spherical indenter with a smaller radius is used. The greater the depth of the scratch, the easier it is for radial, median and lateral (RML) cracks to appear. A side crack easily occurs when the indenter becomes sharp. Radial crack nucleation changes from the position in front of the indenter to the position behind it as the depth of the scratch increases or the angle at the top decreases. RML crack sizes increase with increasing scratch depth or apex angle. The study provides recommendations for choosing the geometry of abrasive grains to increase the speed of material removal and reduce cracks in the process of abrasive processing of brittle materials.

In the study [22], the mechanism of plasticity with a deformation gradient was used to study the dimensional effect in the behavior of single-crystal copper during scratching. The results of this study showed a significant effect of size on scratch hardness values and the amount of layering. This indicates that the degree and nature of the dependence of these two parameters on the size differ significantly and oppositely depending on the direction of scratching. For example, although the [001] direction exhibits the greatest degree of dimensional effect on scratch hardness, it exhibits the least dimensional effect of side layers. Such an opposite effect is explained by the contribution of different sliding systems to the resistance to dislocations and slander. It is also shown that the scratch hardness, which takes into account both the size effect and the dependence on the crystallographic direction, is a suitable material property for wear evaluation.

The hydrogen index (pH) of the process fluid is important for diamond abrasive processing processes. Thus, the article [23] shows the effect of a liquid medium with different pH on the wear of a WC/Co hard alloy with different percentages of cobalt. Diamond scratch tests were conducted on three grades of WC/Co, with a Co content of 6, 11, and 28% by mass and in liquids: distilled (pH6), acidic (pH2), and alkaline (pH10) water. It was established that the cobalt content significantly affects the load in the scratch zone and the coefficient of friction. The latter increases with increasing CO content due to a greater degree of plastic deformation. In addition, it has been proven that at loads less than 62 N, the hydrogen index of the liquid does not affect friction. But at higher loads, the influence of the liquid medium is statistically significant, and distilled water gives a lower coefficient of friction. It should be noted that the influence of the pH of the electrolyte on the change in the composition of the cathode films on the cutting surface of the diamond wheel was also addressed in the article [24]. It was shown that, under such conditions, the polarization of the liquid changes the content of the cathode film on the surface of the wheel in contact with a hard alloy, and with a decrease in the pH of the liquid from 10 to 4, the composition of the film changes dramatically, in which the content of elements of the hard alloy, which is in contact with the grinding medium, increases significantly around. In fact, this means that as the pH value increases, the machinability of the hard alloy deteriorates, since cobalt is less lost from the hard alloy, and therefore, according to [23], not only the loads in the cutting zone, but also the friction coefficient increase.

THE INFLUENCE OF COATINGS ON THE TRIBOLOGICAL BEHAVIOR OF DIAMONDS DURING DIAMOND ABRASIVE PROCESSING

In the article [25], to apply the mechanochemical effect, the diamond film was polished using a grinding wheel containing nickel-plated (Ni) diamond abrasives. The rapid reaction of removing the diamond film is explained by the catalytic effect of the Ni coating, which causes the graphitization of the diamond film at the contact points of the interface under the influence of the high temperature generated during friction; later it can be removed by mechanical action of abrasives (Fig. 12).

Another variant of grinding diamond films (DF) is considered in work [26], based on the application of mechanochemical influence when coating diamond abrasives with titanium (Ti) coatings sprayed in a vacuum. The coating layer forms

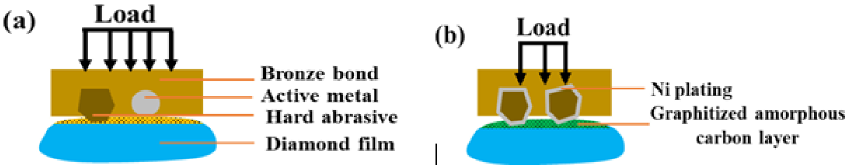

Fig. 12. Scheme describing the interaction of uncoated diamond (a) and nickel-coated diamond (b) with the processed diamond surface [25].

a diamond-TiC-Ti structure extending from the diamond matrix in the direction of the Ti coating. The material removal rate (MRR) of DF is significantly increased as a result of the available active Ti-coating on diamond abrasives, which reacts with DF at the contact points.

In the article [27], another option for accelerating DF grinding based on the mechanochemical effect is proposed. The vacuum evaporation method was used to apply a catalytically active Cr coating on diamond abrasive grains. During grinding, the Cr coating on active abrasives reacted with the diamond film with the formation of Cr_3C_2 or caused graphitization at the contact points at high temperature due to friction. It was shown that the chrome-coated grinding wheel exhibited a higher MRR compared to the uncoated diamond grinding wheel.

In the article [28] thin films of turbostratic boron nitride (t-BN) and cubic boron nitride (c-BN) grown on B-doped polycrystalline and monocrystalline diamond were considered. High-resolution transmission electron microscopy analysis revealed that the cubic boron nitride thin films consist of a mixture of c-BN and t-BN phases, with c-BN being the dominant phase. These findings provide valuable information on the characteristics of c-BN and diamond interfaces and are important for temperature control in their applications.

In work [29], to increase the wear resistance of diamond cutting tools, carbon nanosheets (CNS) were obtained in a strong covalent diamond-graphite structure obtained by laser-induced solid-phase diffusion by electrochemical removal of a graphite layer on a diamond matrix. After 14,400 cycles of reciprocating sliding on a GCr15 ball under a normal load of 2–8 N, friction decreased by 45.9–65.6% with high durability. During this process, the oxygen content is reduced by an order of magnitude, suggesting that CNS can prevent oxidation at the sliding edge. In comparison, the relative wear rate of bare diamond was 4.1–15.4 times higher than that of CNS.

The low interfacial strength between the iron-based matrix and the diamonds causes the diamond particles to fall off prematurely, which significantly affects the cutting efficiency of diamond composites. Work [30] was aimed at optimizing the interfacial microstructure and mechanical properties of diamond/Fe-Ni-WC composites by applying a Mo_2C layer on diamond particles. Mo_2C-coated diamonds were obtained using the molten salt method (Fig. 13). Diamond/Fe-Ni-WC composites were sintered by hot pressing under vacuum. Energy dispersive spectroscopic scanning showed that the Mo_2C coating layer changed the interfacial composition between the matrix and Fe–C alloy diamonds to Mo_2C, improving the interface strength.

That is, the above in [25–30] indicates that the application of the effect of further mechanochemical influence, both on the diamond-bond boundary and on the contact of the surface of the diamond grain with the material being processed, when coating diamond abrasives, allows to increase the efficiency of using diamond abrasives. - abrasive tool.

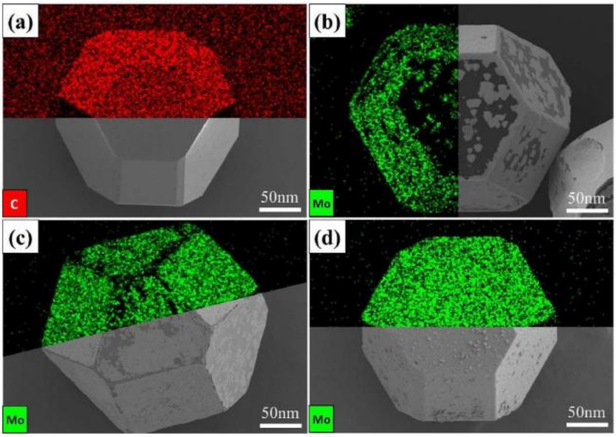

Fig. 13. Micro-morphology of uncoated diamond (a) and Mo_2C-coated diamond prepared at 1050 °C for 15 (b), 30 (c), and 60 min (d) [30].

In the article [31], the microtexture of the CVD-diamond coating was investigated, which, along with the function of retaining wear particles, can to a certain extent reduce the coefficient of friction due to the graphitization of the diamond coating. Graphitization of the textured surface allows to quickly reduce and stabilize the coefficient of friction at the initial stage of friction. After stabilization, the friction coefficient of the diamond coating decreases as the degree of graphitization increases. This is of great importance for expanding the field of application of diamond coatings [31].

In the article [32], the use of solder coating on different types of diamond grains is proposed to improve their retention in the working layer of grinding wheels on a polymer bond. Brazing can successfully cover most of the diamond grains with a layer of additive alloy. Pores and bulges several micrometers in size were observed, as well as the formation of titanium carbide between the coating and the surface of the diamond grains. The viscosities of monocrystalline coated diamond grains (RVD) decreased only slightly, but increased more significantly for polycrystalline coated diamond grains (PDGF1). The wheel containing PDGF1 diamond grains showed the lowest grinding force and the highest performance, while the wheel with RVD coated diamond grains had the highest grinding force and a fairly low grinding ratio.

In the article [33], to determine the features of the reaction of the diamond surface with various types of metals and metal oxides, the activation energy of the reaction between diamond and metals, as well as between diamond and metal oxides, was calculated from the first principles. For the transition metals of the fourth period of the Periodic Table of the Elements, when they react with diamond to form the corresponding metal carbides, the order of increasing activation energy for the metals is: Mn, Fe, V, Ti, Cr, Co, Ni, Zn, and Cu. And when diamond reacts with MnO, FeO, CoO, NiO and CuO to form metals and CO, the calculated activation energy in descending order is: MnO, FeO, CoO, NiO and CuO. Thus, it has been established that NiO and CuO are reduced by diamond to Ni and Cu, which indicates that an oxidation-reduction reaction takes place between diamond and metal oxides.

In [34], a chemical vapor deposition method was proposed, when a diamond coating with CuO particles was applied to a WC/Co substrate. For comparison, a pure diamond coating was produced. The surface morphology proved that the diamond coating can be deposited on a substrate with CuO particles. But CuO particles can lead to the formation of amorphous carbon. Indentation tests showed that the diamond coating with CuO particles showed higher adhesion strength and cracking resistance than the diamond coating without CuO particles. That is, the content of CuO particles affected the crack resistance of the diamond coating. Thus, the dispersion of CuO particles on the surface of the substrate can be considered as a potential technology for adjusting diamond grains due to the inclusion of carbon phases, which, in turn, can increase the crack resistance of the diamond coating to meet industrial requirements.

In work [35], diamond particles were covered with aluminum oxide by the method of atomic layer deposition. As a result, the temperature at which the decomposition of diamond to CO_2 begins shifted towards higher temperatures (≈ 50 K) due to the protective effect of Al_2O_3. It was concluded that the mechanism of diffusion through the protective layers is responsible for this moderate increase in the oxidation temperature. The authors [35] claim that although the amount of improvement is small enough to be used for high-temperature applications, these results indicate that this type of protective coating can be used to protect diamond grains from oxidation.

This was confirmed in [36], where Ti–B–C protective coatings on diamond particles were investigated. The results showed that it is the boron content that is important for the adhesion of the Ti–B–C coating to diamond. Such a coating with a boron content of 60% (at.) protected the diamond from oxidation for more than 1 hour when heated to 1000 °C in air. That is, oxides play a very important role. Thus, in the case of annealing coated diamond in air, the a priori formed B_2O_3 and TiO_2 protected the diamond from oxidation as oxygen-impermeable layers. In addition, with the help of the formation of B_2O_3, it was possible to avoid the delamination of TiO_2 caused by volume expansion during oxidation [36].

INFLUENCE OF ADDITIVES IN THE CONTACT ZONE ON TRIBOLOGICAL INDICATORS DURING DIAMOND ABRASIVE PROCESSING

At the end of this review, let's pay attention to what kind of impurities are introduced into the contact zone during diamond-abrasive processing to change the tribological indicators. At the same time, the most widely used is h–BN, which with a layered crystal structure is one of the types of effective solid lubricants, especially at elevated temperatures.

Obtaining a surface of fused silica at the atomic level with a high MRR with the help of chemical mechanical polishing (CMP) is a difficult task. To solve this, a new suspension for CMP was developed based on potassium oleate and deionized water using CeO_2 abrasive coated with hexagonal boron nitride (h-BN), which reduces friction in the contact zone [37]. Cerium abrasives have implemented a new superlubrication function during CMP thanks to this coating, preventing damage and achieving an ultra-smooth surface (Fig. 13).

In the article [38], the formation energy and stability of h-BN clusters on 10 types of transition metal surfaces were investigated. The results show that h-BN clusters on different metal substrates can undergo a transition to the most stable structure at a critical size, but it is different for metal substrates. The most stable structures for BN clusters on Cu, Pd, and Co surfaces change from chain-like to sp^2-cell at critical size $n = 8$, 7, and 8, respectively. After that, the cellular structure becomes the most energetically beneficial and continues to grow until it covers the entire substrate. The study of BN nucleation at the atomic scale can be useful for planning experiments on the fabrication of h-BN films.

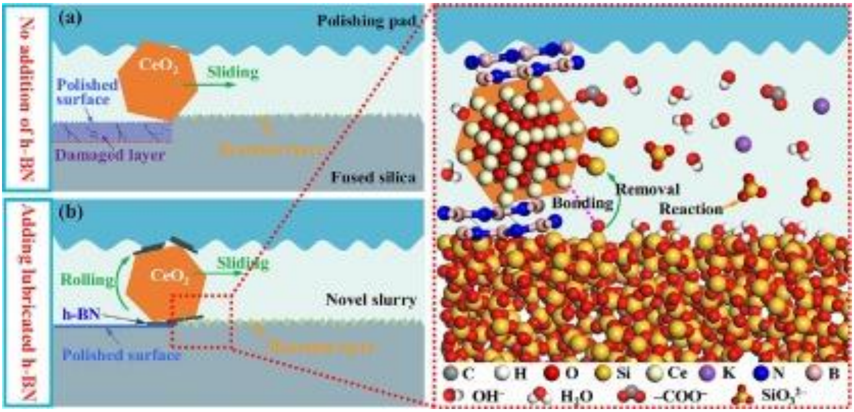

Fig. 13. Schematic representation of the mechanism of superlubrication using h-BN during CMP of fused silica [37].

In [39], the interfacial interaction between diamond and hexagonal boron nitride (hBN) is considered. The weak van der Waals (vdW) interaction between hBN and hydrogen-terminated diamond (H-diamond) provides the basis for introducing the twist angle as a new degree of freedom to modulate the properties of heterostructures. The results showed that the additional free orbitals, which are formed due to the spontaneous relaxation of hBN at higher deformation caused by twisting, can strengthen the vdW bond between hBN and H-diamond, which will promote charge transfer at the interface, thereby weakening the surface scattering of impurities and increasing the accumulation of holes on the H-diamond surface.

In [40] h-BN with a relative density of about 91% was obtained by spark plasma sintering (SPS) technology and its tribological behavior at 1200 °C was investigated. The results showed that the coefficient of friction of h-BN was relatively stable in combination with Si3N4 and remained in the range of 0.215–0.305. It is believed that the low coefficient of friction at 1200 °C is mainly a consequence of weaker interlaminar bonding of h-BN and easier sliding of h-BN plates at high temperature.

The article [41] presents the self-lubricating material Al_2O_3-cBN-hBN. The influence of the cBN/hBN additive on the mechanical and thermal properties of sintered composites was analyzed, and friction and wear tests were conducted. It was established that the addition of cBN particles significantly improves the mechanical and thermal properties of composites. Different hBN content can change the wear mechanism of composites. The release efficiency of hBN particles in the composites was enhanced due to the larger difference in moduli between cBN and hBN. The hardness of Al_2O_3-cBN-hBN composites is improved by at least 54% compared to traditional self-lubricating materials due to the provision of crack resistance and lubricating properties.

The improvement of thermal conductivity is crucial for tribological performance. In [42], a three-dimensional structure with layered elements is obtained by electrostatic assembly of h-BN and graphene oxide (GO) nanosheets. Such a structure helps reduce friction and increase wear resistance based on "synergistic lubrication". As a result, this affects excellent self-lubricating and wear-resistant properties and a noticeable increase in thermal conductivity (1039.16%) of the composite.

Gallium nitride (GaN) is a modern material used for the production of chip boards and powerful devices. In work [43], molecular dynamics modeling was used to study the mechanism of removal of gallium nitride crystals during diamond-abrasive processing using graphene lubrication. The results show that graphene can significantly increase the wear resistance of GaN substrates due to the reduction of surface wear and subsurface damage. That is, graphene has a lubricating and protective effect on the substrate when cutting GaN single crystals with diamond abrasives.

The study [44] studied the nanofriction characteristics of composite thin films of graphene oxide (GO) and cellulose nanocrystals (CNC), as well as reduced graphene oxide (rGO) and CNC, namely GO/CNC and rGO/CNC thin films, under an applied electric potential and humidity using an atomic force microscope (AFM). For all films, the coefficient of friction (COF) depended on the applied electric potential. In addition, the friction force with electric potential increased at low humidity (relative humidity (RH) < 40%) due to the effect of electrostatic force. At high humidity (RH>40%) and high electric potentials (>4 V), the friction force decreases as the electric potential increases due to the phenomenon of electron leakage.

Attention was also paid to the influence of humidity in the article [45], where the characteristics of friction and wear resistance of C/C-CuNi composites under conditions of different humidity were investigated. Lower humidity levels (30–50% RH) led to the formation of a lubricating layer consisting mainly of graphite and CuO, which was manifested in the adhesive wear of the composites together with stable and low coefficients of friction (~0.144) and low wear rates (Fig. 14). While at a relative humidity higher than 70%, there was an increased tendency to form a brittle layer, mainly consisting of $Cu(OH)_2$ and $Cu_2(OH)_2CO_3$ compounds, due to tribochemical reactions between the composites and H_2O and CO_2 in humid air. In the future, this brittle oxide layer led to abrasive wear, which was accompanied by fluctuations in the coefficient of friction and an increase in the rate of wear.

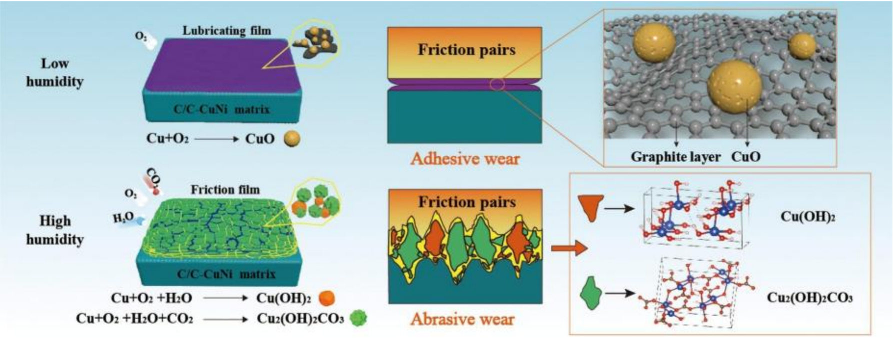

Fig. 14. Schematic presentation of wear mechanisms of C/C-CuNi composites under conditions of different humidity [45].

In the article [46], the microtexture of the CVD-diamond coating has the function of retaining wear particles and can to a certain extent reduce the coefficient of friction due to graphitization. It was established that the degree of graphitization of the microtexture of the diamond coating decreases by an order of magnitude within concentric circles. At the same time, it correlates with the density of the microtexture. Texture depth has a weak positive effect on the degree of graphitization. Graphitization of the textured surface allows you to quickly reduce and stabilize the coefficient of friction at the initial stage of friction (Fig. 15). After stabilization, the friction coefficient of the diamond coating decreases with an increase in the degree of graphitization. A layer of graphite on a microtextured surface with a diamond coating can improve dry friction characteristics. This is of great importance for increasing the accuracy of processing diamond-coated tools.

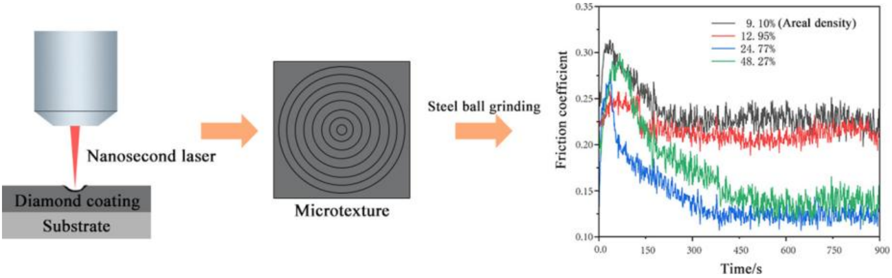

Fig. 15. Schematic representation of the formation of the microtexture of the CVD-diamond coating and the change in the coefficient of friction over time [46].

The above indicates that it is carbon materials that are particularly suitable for reducing friction. Attention is also drawn to this in the article [47], where it is shown that carbon dots (CD), a kind of carbon-based nanomaterials, were widely used as highly effective lubricant additives. Studies show that doping the surface with heteroatoms, especially several heteroatoms, can significantly improve their tribological characteristics. Moreover, it was established [47] that the tribological behavior of N,B,P-CD is better than that of N,B-CD and P-CD under identical test conditions, demonstrating a multiatomic synergistic lubrication effect. The excellent tribological characteristics of N,B,P-CD are explained by their favorable film-forming ability and effect of nanolubrication at various stages of friction.

In [48], a multilayer composite coating of cBN/NCD (cubic boron nitride and nanocrystalline diamond) with modulation periods of 1 µm, 1.5 µm, and 3 µm was deposited using a linear ion source of radio frequency magnetron sputtering and microwave plasma chemical vapor deposition (MPCVD) on tungsten cobalt hard alloys (YG6) and silicon substrates. It was found that as the modulation periods decreased, the surface roughness of cBN/NCD multilayer composite coatings tended to increase, but the mechanical properties improved significantly. Friction and wear tests proved that the wear resistance of the cBN/NCD multilayer composite coating is related to residual stresses and fracture toughness, the friction coefficient remains stable at about 0.12–0.15, and the rate of wear decreases significantly with a decrease in the modulation period. Thus, the tribological behavior of the N,B,P-CD described above in the article [47] was confirmed in [48].

However, as shown in the article [49], diamond-like carbon (DLC) films quickly lose lubricity due to oxidation and mechanical breakdown when used at temperatures higher than 300 °C. Doping with molybdenum disulfide (MoS_2) is considered as a possible method of improving the high-temperature properties of DLC films. The results showed that MoS_2 was successfully incorporated into the DLC matrix, and the Mo content in the films ranged from 0 to 6.15 at. %. It was established that MoS_2-DLC composite films with 3.78–6.15 at. % Mo retain good anti-friction and anti-wear properties in the temperature range of 25–450 °C. The friction mechanism of the films changed depending on the temperature. At 25 °C, MoS_2-DLC composite films showed good lubricating and antiwear properties, since the carbon bond is passivated by H_2O molecules. At 250 °C, the MoS_2 phase was deposited on the surface of the films, which led to low friction. At 350 °C, a solid solution of $MoS_{2-x}O_x$ was formed on the surface of the wear track, which ensured low values of the coefficient of friction and wear even up to 450 °C.

In work [50], Cu–Sn matrix composites were prepared by the sintering method with the addition of MoS_2, graphite, and the MoS_2/graphite mixture, respectively. Frictional wear characteristics and contact resistance of these composites at different currents were investigated. The results showed that MoS_2 and graphite have a synergistic lubricating effect. The Cu-Sn-graphite-MoS_2 composite showed low wear rates and contact resistance. That is, MoS_2 can effectively promote the formation and integrity of the friction film and optimize the friction wear characteristics.

In the article [51], to enhance the lubricating effect and stimulate the development of methods for manufacturing self-lubricating cutting tools, powders based on Ni, dispersed with MoS_2 and Al_2O_3 particles, were previously planted on the substrate of the tool; subsequently self-lubricating coatings (SLCs) were applied using laser powder melting additive manufacturing (AM) with a nanosecond fiber laser for cutting. The results showed that the developed SLC tools reduced the coefficient of friction by 8.8–11.7%, the cutting forces by 17.6–29.6%, and the cutting power by 17.3–22.0% compared to with conventional high-speed steel (HSS) cutting tools.

Thus, from the above review, dedicated to the features of tribological processes during diamond-abrasive processing and the behavior of diamonds and other carbon-containing materials during friction and wear, it is possible to draw the following conclusions:

Additive manufacturing (AM) methods have significant advantages for obtaining individual products and prototypes, allow to reduce costs, and also accelerate the release of products to the market. Nowadays, this direction has begun to be used for diamond-abrasive tools. Of course, new binders for the working layer of the diamond tool have been developed for such energy-efficient AM technology. It is shown that the cutting forces and friction coefficients of microtextured diamond tools are significantly reduced.

The tribological behavior of diamonds against various materials is fundamental for their use in the abrasive and bearing industries. It has been proven that, in comparison with ordinary diamond grains, porous diamond grains with an increased number of microedges effectively reduce the cutting force and heat generation. It is shown that the application of the effect of further mechanochemical influence during the coating of diamond abrasives, both on the diamond-bond boundary and on the contact of the surface of the diamond grain with the processed material, allows to increase the efficiency of the use of the diamond-abrasive tool.

Attention is drawn to what kind of impurities are introduced into the contact zone during diamond-abrasive processing to change the tribological parameters. At the same time, the most widely used is h–BN, which with a layered crystal structure is one of the types of effective solid lubricants, especially at elevated temperatures. Attention has been paid to such new materials as graphene oxide and carbon dots (CD), a kind of carbon-based nanomaterials, which have been widely used as highly effective lubricant additives.

References: **1.** *Lavrinenko V.I. and Solod V.Yu.* The process of abrasive machining as a friction interaction between dissimilar materials. Journal of Superhard Materials, 2018, Vol. 40, No. 2, pp. 138–142. doi: 10. 3103/s1063457618020090 **2.** Modification of diamond tool by focused ion beam in dry single-point diamond turning / *Jianbiao Du, Hanzhong Liu, Ning Yang, Xiaozhou Chen, Wenjun Zong.* Applied Surface Science. Volume 637, 15 November 2023, 157882. https://doi.org/10.1016/j.apsusc.2023.157882 **3.** A novel 3D printed compliant ball-end grinding tool with crystal structure: Feasibility and performance analysis / *Mingcong Li, Yun Huang, Wenxi Wang, Shengbo Yan, Yingjie Liu, Lai Zou.* Materials & Design. Volume 237, January 2024, 112591. https://doi.org/10.1016/j.matdes.2023.112591 **4.** Influence of bond thermal and mechanical properties on the additively manufactured grinding wheels performance: Mechanical, wear, surface integrity, and topography analysis / *Mohsen Barmouz, Felix Steinhäuser, Bahman Azarhoushang, Jahangir Khosravi.* Wear. Volumes 538–539, 15 February 2024, 205215. https://doi.org/10.1016/j.wear.2023.205215 **5.** The effects of SiO_2 coating on diamond abrasives in sol-gel tool for SiC substrate polishing / *Jing Lu, Yongchao Xu, Yunhe Zhang, Xipeng Xu.* Diamond and Related Materials. 2017. V. 76. pp. 123–131. https://doi.org/10.1016/j.diamond.2017.05.003 **6.** Experimental study on grinding 2.5D C/SiC composites by electroplated grinding wheel with ordered abrasive clusters / *Ye Guo, Bing Chen, Xiaojing Fu, Hu Xu, Shiwei Sun.* Diamond and Related Materials. Volume 142, February 2024, 110838. https://doi.org/10.1016/j.diamond.2024.110838 **7.** Development of a novel bulk metallic glass bonded single-layer diamond wheel / *Dandan Wu, Zijun Liu, Yufu Yan, Qiaosen Liang, Liyan Luo, Chengyong Wang.* International Journal of Machine Tools and Manufacture. Volume 197, April 2024, 104146. https://doi.org/10.1016/j.ijmachtools.2024.104146 **8.** Porous grinding wheels toward alleviating the pre-fatigue and increasing the material removal efficiency for rail grinding / *Yongjie Yuan, Wulin Zhang, Pengfei Zhang, Xiaoqiang Fan, Minhao Zhu.* Tribology International. Volume 154, February 2021, 106692. https://doi.org/10.1016/j.triboint.2020.106692 **9.** Accurate modeling of material removal depth in convolutional process grinding for complex surfaces / *Haoyuan Zhou, Huan Zhao, Xiangfei Li, Zairan Xu, Han Ding.* International Journal of Mechanical Sciences. Volume 267, 1 April 2024, 109005. https://doi.org/10.1016/j.ijmecsci.2024.109005 **10.** Micro-scale contact behavior and its effect on the material removal process during chemical mechanical polishing / *Lin Wang, Ping Zhou, Ying Yan, Changyu Hou, Dongming Guo.* Tribology International. Volume 156, April 2021, 106831. *https://doi.org/10.1016/j.triboint.2020.106831* **11.** *Yayoi Tanaka, Hisashi Sato, Osamu Eryu.* Improved cemented carbide tool edge formed by solid phase chemical–mechanical polishing. Journal of Materials Research and Technology. Volume 20, September–October 2022, Pages 606–615. https://doi.org/10.1016/j.jmrt.2022.07.077 **12.** *Trilochan Prasad Nanda, Amitava Ghosh.* Influence of grit friability and grit distribution pattern on dry grindability of WC-6Co by single layered brazed diamond wheels. Diamond and Related Materials. Volume 147, August 2024, 111300. https://doi.org/10.1016/j.diamond.2024.111300 **13.** Grain wear properties and grinding performance of porous diamond grinding wheels / *Wei Li, Xiaolong Hu, Gui Long, Aoshuang Shang, Bing Guo.* Wear. Volumes 530–531, 15 October 2023, 204993. https://doi.org/10.1016/j.wear.2023.204993 **14.** *Weihao Ma, Jiahui Li, Xi Hou.* Rolling model analysis of material removal in elastic emission machining. International Journal of Mechanical Sciences. Volume 258, 15 November 2023, 108572. https://doi.org/10.1016/j.ijmecsci.2023.108572 **15.** A novel low-rotation-speed dynamic friction polishing of diamond / *Xiaowei Jiang, Geng Wu, Shiyu Guan, Yuanhao Mao, Zeya Yang, Xingwu Long,* *Lishan Zhao, Qing Qi, Zhongqi Tan.* Diamond and Related Materials. Volume 136, June 2023, 109932. https://doi.org/10.1016/j.diamond.2023.109932 **16.** Comparing the tribological behavior of polycrystalline diamonds against steel GCr15 and ceramic Si_3N_4: friction and wear / *Xiwei Cui, Yue Qin, Xin Han, Huanyi Chen, Xinxin Ruan, Hui Zhang, Chengcheng Jiao, Rongqi Mao, Jinglin Hao, Sizhuang Zhao, Shuai Hou, Xiaoxuan Pian, Yandong Wang, Kazuhito Nishimura, Lifen Deng, Nan Jiang.* Diamond and Related Materials. Volume 141, January 2024, 110550. https://doi.org/10.1016/j.diamond.2023.110550 **17.** *Ruyi Gou, Jiawang Zhao, Xun Luo.* Tribological behavior of PDC-CR at different temperatures. Diamond and Related Materials. Volume 144, April 2024, 110950. https://doi.org/10.1016/j.diamond.2024.110950 **18.** *Junxin Chen, Ying Long, Hua-Tay Lin, Fenglin Zhang.* Friction and wear behaviors of boron-containing high entropy alloy/diamond composites. Diamond and Related Materials. Volume 144, April 2024, 110998. https://doi.org/10.1016/j.diamond.2024.110998 **19.** Capillary adhesion governs the friction behavior of electrochemically corroded p olycrystalline diamond / *Chen Xiao, Liang Peng, Cyrian Leriche, Feng-Chun Hsia, Bart Weber, Steve Franklin. Carbon.* Volume 205, 5 March 2023, pp. 345–352. https://doi.org/10.1016/j.carbon.2023.01.050 **20.** Friction and cutting characteristics of micro-textured diamond tools fabricated with femtosecond laser / *Qingwei Wang, Ye Yang, Peng Yao, Zhiyu Zhang, Shimeng Yu, Hongtao Zhu, Chuanzhen Huang.* Tribology International. Volume 154, February 2021, 106720. https://doi.org/10.1016/j.triboint.2020.106720 **21.** *Huapan Xiao, Shenxin Yin, Chi Fai Cheung, Chunjin Wang.* Cracking behavior during scratching brittle materials with different-shaped indenters. International Journal of Mechanical Sciences. Volume 268, 15 April 2024, 109041. https://doi.org/10.1016/j.ijmecsci.2024.109041 **22.** *Jinxuan Zhu, Ramin Aghababaei.* On the size effect in scratch and wear response of single crystalline copper. Tribology International. Volume 186, August 2023, 108573. https://doi.org/10.1016/j.triboint.2023.108573 **23.** Liquid media effect on the abrasion response of WC/Co hardmetal with different cobalt percent / *R.V. Magnol, T. Gatti, M.C. Romero, A. Sinatora, C. Scandian.* Wear. Volume 477, 18 July 2021, 203815. https://doi.org/10.1016/j.wear.2021.203815 **24.** *Lavrinenko, V.I.* The impact of the hydrogen index of the process fluid on diamond abrasive wheel performance // Journal of Superhard Materials, 2024, Vol. 46, No. 1, pp. 76–79. doi: 10.3103/s1063457624010064 **25.** Rapid grinding diamond film using a grinding wheel containing nickel-plated diamond abrasives based on mechanochemical effect / *Yingke Zhou, Yanhui Wang, Shengyao Su, Lixiang Zhao, Menghui Zhao, Yungang Yuan, Jianbing Zang, Jing Lu, Xipeng Xu, Pingwei Zhang.* Diamond and Related Materials. Volume 139, November 2023, 110389. https://doi.org/10.1016/j.diamond.2023.110389 **26.** Mechanochemical grinding diamond film using titanium-coated diamond active abrasives prepared by vacuum micro-evaporation coating / *Yingke Zhou, Jianbing Zang, Shengyao Su, Chaoyang Zhang, Lixiang Zhao, Yungang Yuan, Yanhui Wang, Jing Lu, Xipeng Xu, Pingwei Zhang.* Applied Surface Science. Volume 638, 30 November 2023, 158094. https://doi.org/10.1016/j.apsusc.2023.158094 **27.** Efficient grinding diamond film using chromium-coated diamond grinding wheel based on mechanochemical effect / *Yingke Zhou, Jianbing Zang, Shengyao Su, Lixiang Zhao, Chaoyang Zhang, Yungang Yuan, Yanhui Wang, Jing Lu, Xipeng Xu, Pingwei Zhang.* Journal of Materials Processing Technology. Volume 320, November 2023, 118123. https://doi.org/10.1016/j.jmatprotec.2023.118123 **28.** Optical and acoustic phonons in turbostratic and cubic boron nitride thin films on diamond substrates / *Erick Guzman, Fariborz Kargar, Avani Patel, Saurabh Vishwakarma, Dylan Wright, Richard B. Wilson, David J. Smith, Robert J. Nemanich, Alexander A. Balandin.* Diamond and Related Materials. Volume 140, Part A, December 2023, 110452. https://doi.org/10.1016/j.diamond.2023.110452 **29.** Inhibition effect of covalent carbon nanosheets on mechanochemical wear of diamond / *Ni Chen, Junyi Zhao, Runkai Wang, Bo Yan, Yang Wu, Liang Li, Nan Yu, Ning He.* Materials & Design. Volume 237, January 2024, 112573. https://doi.org/10.1016/j.matdes.2023.112573 **30.** Mo_2C interface layer: effect on the interface strength and cutting performance of diamond/Fe-Ni-WC composites / *Xinyue Mao, Qingnan Meng, Mu Yuan, Sifan Wang, Shiyin Huang, Baochang Liu.* Journal of Materials Research and Technology. Volume

25, July–August 2023, Pages 2029–2039. https://doi.org/10.1016/j.jmrt.2023.06.098 **31.** Research on the influence of diamond coating microtexture on graphitization law and friction coefficient/ *Fan Wu, Niu Liu, Yuping Ma, Xingxing Zhang, Yuan Han*. Diamond and Related Materials. Volume 127, August 2022, 109153. https://doi.org/10.1016/j.diamond.2022.109153 **32.** Preparation and performance of resin-bonded grinding wheel with braze-coated diamond grits / *Ming-cong Li, Feng-lin Zhang, Yu-mei Zhou, Wei-xiong Li, Shixiong Wu, Shanghua Wu*. Diamond and Related Materials. Volume 101, January 2020, 107619. https://doi.org/10.1016/j.diamond.2019.107619 **33.** Exploring the activation energy of diamond reacting with metals and metal oxides by first-principle calculation / *Ao Deng, Jing Lu, Dongxu Li, Yanhui Wang.* (2021) Diamond and Related Materials. V. 118. 108522. https://doi.org/10.1016/j.diamond.2021.108522 **34.** Growth and characterization of chemical vapor deposition diamond coating incorporated amorphous carbon with high Raman bands induced by CuO particles / *Naichao Chen, Fasong Ju, Fan Zhou, Shuai Chen, Kun Wei, Ping He*. (2021) Diamond and Related Materials. V. 116. 108387. https://doi.org/10.1016/j.diamond.2021.108387 **35.** Enhancing the oxidation resistance of diamond powder by the application of Al_2O_3 conformal coat by atomic layer deposition / *D.Dominguez , H.Tiznado, H.A.Borbon-Nuñez, F.Muñoz-Muñoz, J.M.Romo-Herrera, G.Soto.* (2016) Diamond and Related Materials. V. 69. Pages 108–113. https://doi.org/10.1016/j.diamond.2016.08.005 **36.** Enhancement of oxidation resistance via titanium boron carbide coatings on diamond particles / *Youhong Sun, Chi Zhang, Jinhao Wu, Qingnan Meng, Baochang Liu, Ke Gao, Linkai He.* Diamond and Related Materials. Volume 92, February 2019, Pages 74–80. https://doi.org/10.1016/j.diamond.2018.12.019 **37.** Novel green chemical mechanical polishing of fused silica through designing synergistic CeO_2/h-BN abrasives with lubricity / *Jie Liu, Zhenyu Zhang, Chunjing Shi, Zheng Ren, Junyuan Feng, Hongxiu Zhou, Zhensong Liu, Fanning Meng, Shuming Zhao.* Applied Surface Science. Volume 637, 15 November 2023, 157978. https://doi.org/10.1016/j.apsusc.2023.157978 **38.** *Hongxia Zhu, Chong Chen, Jitai Niu, Ruiqi Zhao.* Revealing the nucleation mechanism of CVD-prepared hexagonal boron nitride on transition metal surfaces: A study from DFT calculations. Diamond and Related Materials. Volume 140, Part A, December 2023, 110402. https://doi.org/10.1016/j.diamond.2023.110402 **39.** Twist angle modulated electronic properties and band alignments of hydrogen-terminated diamond (111)/hexagonal boron nitride heterostructures / *Boyu Wang, Jing Ning, Jincheng Zhang, Chi Zhang, Dong Wang, Yue Hao.* Applied Surface Science. Volume 614, 30 March 2023, 156245. https://doi.org/10.1016/j.apsusc.2022.156245 **40.** Tribological behavior under 1200°C elevated temperature of spark plasma sintered *h*-BN bulk / *Juanjuan Chen, Jun Cheng, Shengyu Zhu, Qichun Sun, Jiao Chen, Huwei Sun, Benbin Xin, Jun Yang.* Tribology International. Volume 193, May 2024, 109420. https://doi.org/10.1016/j.triboint.2024.109420 **41.** High-Pressure synthesis of Al_2O_3-cBN-hBN Self-lubricating ceramic / *Jiakun Wu, Haikuo Wang, Chao Wang, Zhicai Zhang, Yao Tang, Zhiqiang Hou, Shun Wan, Dazhuan Wu, Zhongjun Tan, Xiaoping Ouyang.* Materials & Design. Volume 217, May 2022, 110638. https://doi.org/10.1016/j.matdes.2022.110638 **42.** 3D structurally advanced graphene oxide/*h*-BN hybrid for solid self-lubrication with enhanced thermal conductivity / *Nan Zhang, Yaoming Zhang, Song Li, Lihe Guo, Zenghui Yang, Xinrui Zhang, Tingmei Wang, Qihua Wang.* Tribology International. Volume 176, December 2022, 107918. https://doi.org/10.1016/j.triboint.2022.107918 **43.** Removal mechanism of double-diamond-abrasive-grinding GaN single crystals under graphene lubrication / *Mei Xu, Tinghong Gao, Lianxin Li, Bei Wang, Qian Chen, Jin Huang, Qingquan Xiao.* Diamond and Related Materials. Volume 148, October 2024, 111381. https://doi.org/10.1016/j.diamond.2024.111381 **44.** *Hyeonho Cho, ChaBum Lee, Sangmin Lee, Sunghan Kim.* Effect of applied electrical potential and humidity on friction of Graphene-Based thin films. Applied Surface Science. Volume 672, 1 November 2024, 160802. https://doi.org/10.1016/j.apsusc.2024.16080 **45.** Effect of humidity on the friction and wear behavior of C/C-CuNi composites / *Haibo Ouyang, Peng Wang, Cuiyan Li, Ruinan Gao, Tianzhan Shen, Yanlei Li.* Diamond and Related Materials. Volume 146, June 2024, 111144. https://doi.org/10.1016/j.diamond.2024.111144 **46.** Research on the influence of diamond coating microtexture on graphitization law and friction coefficient / *Fan Wu, Niu Liu, Yuping Ma, Xingxing Zhang, Yuan Han.* Diamond and Related Materials. Volume 127, August 2022, 109153. https://doi.org/10.1016/j.diamond.2022.109153 **47.** *Wei Zhu, Yuhui Tan, Weiwei Tang, at al.* (2023) Late-model N, B, and P-co-doped carbon dots as additives for friction-reduction and anti-wear. Diamond and Related Materials. Volume 139, November, 110315. https://doi.org/10.1016/j.diamond.2023.110315 **48.** Effect of the modulation periods on the mechanical and tribological properties of CBN/NCD multilayer composite coating / *Shuai Tian, Feng Xu, Zhenyu Ma, Qian Zhou, Yanchao Zhao, Zheng Li, Dong Wang, Guang Zeng, Dunwen Zuo.* Diamond and Related Materials. Volume 132, February 2023, 109628. https://doi.org/10.1016/j.diamond.2022.109628 **49.** Friction and wear behavior of molybdenum-disulfide doped hydrogen-free diamond-like carbon films sliding against Al_2O_3 balls at elevated temperature / *Yanjun Chen, Haichao Li, Fenghua Su, Guozheng Ma, Qiang Li, Jianfang Sun, Songsheng Lin.* Wear. Volumes 544–545, 15 May 2024, 205296. https://doi.org/10.1016/j.wear.2024.205296 **50.** Electrical sliding friction wear behaviors and mechanisms of Cu–Sn matrix composites containing MoS_2/graphite / *Tao Zhou, Xu Wang, Liu-xin Qin, Wen-ting Qiu, Shi-fang Li, Yan-bin Jiang, Yan-lin Jia, Zhou Li.* Wear. Volumes 548–549, 15 June 2024, 205388. https://doi.org/10.1016/j.wear.2024.205388 **51.** Assessment of self-lubricating coated cutting tools fabricated by laser additive manufacturing technology for friction-reduction / *Youqiang Xing, Cheng Luo, Mingyu Zhu, Yanhua Zhao, Kornel Ehmann, Ze Wu, Lei Liu.* Journal of Materials Processing Technology. Volume 318, September 2023, 118010. https://doi.org/10.1016/j.jmatprotec.2023.118010

.

Валерій Лавріненко, Київ, Україна, Володимир Солод, Кам'янське, Україна, Євгеній Островерх, Володимир Федорович, Харків, Україна, Предраг Дашич, Бєлград, Сербія

АЛМАЗНО-АБРАЗИВНА ОБРОБКА: ТРИБОЛОГІЧНИЙ АСПЕКТ (ОГЛЯД СУЧАСНИХ ДОСЛІДЖЕНЬ)

Анотація. *Попередньою практикою інструментального виробництва та застосування різального інструменту у промисловості доведено, що для досягнення ефективного та економного використання цього сучасного високовартісного інструменту треба не тільки забезпечити високоякісну шліфовану їх поверхню, але і мати доведену різальну крайку. Досягнути цього можливо лише доведенням після шліфування різальної крайки, а і навіть її поліруванням, коли шорсткість передньої та задньої поверхонь інструменту доводиться до R_a 0,05 мкм, а іноді навіть менше, що значно підвищує зносостійкість різального інструменту та якість обробленої ним поверхні. Сучасні дослідження свідчать про ефективність застосування при поліруванні абразивних і хіміко-механічних методів та врахуванні при цьому особливостей абразивів, які застосовуються, тому метою даної статті було дослідити найновіші (2024–2025 рр.) розробки в технологіях доведення та полірування поверхонь широкої гами сучасних матеріалів та визначити напрямки підвищення ефективності таких розробок. При цьому для хіміко-механічного полірування (СМР) дослідниками розглядається два напрямки: вплив різного абразиву, тобто наголос на механічній складовій СМР, та вплив суспензії, тобто наголос на хімічній складовій. Дослідження в напрямку пріоритетності абразивної складової представлені новою стратегією застосування інтерметалічної сполуки Cu_6Sn_5 у якості зв'язки в алмазному шліфувальному крузі для шліфування і доведення пластин SiC з високим терміном служби і обробки з низьким рівнем пошкоджень. Досліджено новий метод двостороннього шліфування із* *застосуванням алмазних плівкових накладок для обробки циліндричних роликів* Si_3N_4*. Запропонований екологічно чистий метод поліпшення продуктивності поліровки із застосуванням змішаної абразивної суспензії церію і алмаза. Дослідження , як перехідне від механічної до хімічної складової, розкриває хімічну роль абразивної* Al_2O_3*–частинки при CMP рутенію шляхом порівняння властивостей і продуктивності поліровки* Al_2O_3–SiO_2 *змішаними частинками і чистими –* SiO_2*. Представлені нові розробки з виготовлення абразивів типу ядро-оболонка* SiO_2@A-TiO_2 *в новій суспензії для реалізації високоефективної фотокаталітичної хіміко-механічної поліровки при опроміненні штучним сонячним світлом. Досліджені характеристики CMP за нової суспензії, що містила Fe,* Al_2O_3 *і новітній матеріал – оксид графена, оскільки останній є чудовим матеріалом-носієм, характеристики якого можуть значно поліпшити каталітичні характеристики суспензії. Окремо звернено увагу на застосування при CMP деіонізованої води, оскільки це є певним сучасним трендом досліджень.*

Ключові слова: *доведення поверхні; хіміко-механічне полірування; алмазні абразиви; оксид графена; деіонізована вода.*

ISSN 2078-7405 Cutting & Tools in Technological System, 2025, Edition 103

UDC 62.971 **doi: 10.20998/2078-7405.2025.103.02**

PERFORMANCE ANALYSIS OF ROTATING LATENT HEAT STORAGE SYSTEM

A.G. **Guna** [0009-0002-3765-8992], M. **Sudharshan** [0009-0003-9692-9681],

Government College of Engineering Salem, Salem, India
agguna.cad@gmail.com

Received: 06 October 2025 / Revised: 01 November 2025 / Accepted: 20 November 2025 / Published: 15 December 2025

Abstract. *In recent years, shell and tube latent heat thermal energy storage system (LHTESS) with phase changing materials (PCM) are used to store energy. The major drawback of latent heat storage system is due to low thermal conductivity of PCM the heat transfer is low. In this study, a 2-dimensional horizontal shell and tube latent heat storage system is considered, the rotation is implemented to accelerate charging process of the system. ANSYS FLUENT 2022 R2 software is used for the simulation and calculation. Paraffin wax (n-octadecane) and water are used as PCM and hot fluid (HTF) respectively. The simulation and calculation are carried out for 0.5 rpm, 1 rpm and 1.5 rpm and these results are compared with stationary counterpart. The result show that rotation accelerate melting process. The percentage thermal enhancement between rotation and stand stand still for 0.5 rpm, 1 rpm and 1.5 rpm are 8%, 18.61% and 25.38% respectively.*

Keywords: *Rotating latent heat storage system; ANSYS; Paraffin wax (n-octadecane).*

1. Introduction

A rotating latent heat storage system (RLHSS) is an innovative thermal energy storage technology that utilizes phase change materials (PCMs) to store and release thermal energy. Rotating latent heat storage system consist of a cylindrical container filled with PCMs that is rotate around its axis to enhance heat transfer during charging cycle. The PCMs undergo phase change (solid-liquid or liquid-solid) during thermal energy storage and release, resulting in high energy density and efficient heat transfer. RLHSS has potential application in various fields, such as solar energy storage, waste heat recovery and thermal management of buildings. The Latent heat storage system stores heat in a storage medium in the form of potential energy between the particles of the substance. The conversion between the heat and the potential energy within the substance involves a phase change thus heat storage occurs without significant temperature changes in the storage medium. Digant S.Metha, Bhavesh Vaghela, Manish K. Rathod studied about the heat transfer intensification technique by imparting eccentricity and imparting rotation and providing multi hot fluid tube [1]. Stearic acid (5.57–56.6º C) is the melting time is reduced by 47.75%. Binjian Nie, Xiaohuishe studied about compact thermal storage device containing phase change material is designed and experimentally investigated two types of fins were used serrated and perforated fins. The efficiency is increased by 43.3%[2]. Teng Xiong, Long Zhung Flat plate collector and evacuated tube collectors are used Phase changing material used is Ethylene glycol and Aluminium fins were used [3]. Lihar Asipkhan, Muhammad Khan investigated the heat of latent heat storage system with shell and tube heat exchange. The shell consist of annular fin Performance is increased by 10% [4]. Alberto Pizzolato (2017): This paper presents a unique solution to the problem of heat transfer in shell-and-tube latent heat thermal energy storage units by means of high conducting _ns [5]. We developed a design approach using topology optimization and multi-phase computational fluid dynamics. No assumption is made about the _ns layout, which freely evolves along the optimization process resulting in more efficient non-trivial geometries. At each optimization iteration, the fluid-dynamic response in the phase change material is computed by solving the transient Navier-Stokes equations augmented with a phase-change porosity term. Coupling large design freedom to detailed physics modeling allowed studying the effect of convective transport on both design and performance of latent heat thermal storage units. Results indicate that accounting for fluid design optimization studies is crucial for performance. It is shown that melting and solidification can be enhanced remarkably through natural convection by using well engineered with specific design features, that could hardly be revealed with alternative design routes. These features make designs optimized for melting fundamentally from those optimized for solidification. Mr. K. Manikandan (2021): Convective heat transfer between a surface and the surrounding has been a major issue and a topic of study for a long time [6]. In this project, the heat transfer performance of fin is analyzed by ANSYS workbench. Various design configuration are performed such as Cylindrical configuration, Square configuration, and Rectangular configuration. The heat transfer performance of fin with same base temperature having various geometry is compared. In this thermal analysis Aluminium was used as the base metal for the fin material and for various configuration. Fin is major component used in many systems for increasing the rate of heat transfer. In order to cool the system fins are provided on the surface of the system to increase the rate of heat transfer. By doing thermal analysis on the fins , It is helpful to know the heat dissipation and rate of heat transfer in different types of fins. By increasing the surface area of fin configuration we can increase the heat dissipation rate of this process, so designing the large complex is very difficult. A fin for the Circular, Square, Rectangular and conical surface that extends from a fin configuration to increase the rate of heat transfer. Azeem Anzar (2016): The present work is a numerical study consisting of thermal analysis of various configurations of finned heat sink with PCM [7]. The configurations considered are finned heat sink with PCM and without PCM, fin filled with half PCM material, towards the fin tip side and cases which includes forced convection for systems which continuously operates. The transient nature of problems were recorded for performing unsteady analyses. Evaluation of design operational time and characteristics of PCM are carried out. By analyzing these different configurations and valid picture of the physics of heat transfer in PCM based heat sink is imaged out. Pawar Shreekant Prabhakar (2015): Modern portable electronic devices are becoming more compact in space, the exponential increase in thermal load in air cooling devices require the thermal management system (i.e. heat sink) to be optimized to attain the highest performance in the given space [8]. In this work, experimentation is performed for high heat flux condition. The heat sink mounted on the hot component for cooling the component under forced convection. The two different orientation of fan i.e. “fan-on-top” and “fan-on-side” are tested for different air mass flow rate and cooling rate is validated with numerical results for the same amount of heat flux. The numerical simulation are performed using computational fluid dynamics (CFD). The primary goal of this work is to do the thermal analysis and comparison of fan orientation on cooling efficiency and to find the optimum parameters for a natural air-cooled heat sink at which the system will continue its operation in natural convection mode (i.e. fan-failed condition). The CFD simulations are performed for optimization of heat sink parameters with objective function of maximization of heat transfer coefficient. In this study, CPU cooling has been investigated in the acrylic cabinet with chosen heat sink and the performance of the heat sink is investigated experimentally and then validated using CFD. P. M. Deshpande & Dr. S. Dawande studied horizontal zigzag coil tube (HSTC) for various forces (viscous, buoyancy and centrifugal force) acting on fluid element in coil; of which the centrifugal force is predominant and results in secondary flow [9]. This phenomenon also depends on the physical fluid at a given temperature. They also concluded that as the coil diameter reduces the curvature ratio increase that increases the pressure drop. [10]Yan Ke, G. P. Qi, et al. [10]. They had analyze transverse vibration of conical zigzag tube bundle. The effect of the external fluid flow on the transverse vibration of tube bundle is studied with the combination of experimental data, empirical correlations and FEM. The external fluid flow has a significant effect on the frequency of the tube’s transverse vibration, which are decreased by about 18% to 24% when the external fluid flow speed is 0.3 m/s. [11]Dr. M. S. Tandale & S. M. Joshi provided analytical model to design of zigzag tube heat exchanger and experiments were performed [11]. The experimental results show that the deviation between calculated values of overall heat transfer coefficient from the experimental results and theoretical values obtained from the analytical model are within 12%. Also, the accuracy is found to be within ±8 % in approximation. The pressure drop estimated is also compared with actual values observed during experimentation, which is found in acceptable range. R. K. Patil, & B. W. Shende et al. proposed that heat transfer rate of helical coil heat exchanger is better to compare another types of heat exchanger [12]. In the helical coil heat exchanger space is limited so not enough straight pipes should be laid. The helical tube heat exchangers consist of helical coil fabricated out metal pipe that is fitted in the annular portion of two concentric cylinders. M. P. Nueza & G. T. Polley provides the design space where the available options that meet the heat duty and allowable pressure drops are displayed for the various geometrical parameters. the design space is determined considering standard exchanger by a set of set of three curves: a curve that represents the heat duty (thermal length) and two curves that represent the pressure drop on the hot and cold streams [13]. They conclude that the graphical representation of the design parameters that fulfil the process heat load and pressure drops. They refer to the selection of the exchanger dimensions that will meet the heat duty within the limitations of pressure drop and the space between the streams is same.

2. Need of the study

The major drawback of latent heat storage system is due to low thermal conductivity of PCM, heat transfer is low. So PCM takes more time to melt. To overcome this rotation is implemented to accelerate the charging process of the system. Simulation and calculation are carried out for three different rotational speed such as 0.5 rpm, 1 rpm and 1.5 rpm.

3. Research methodology

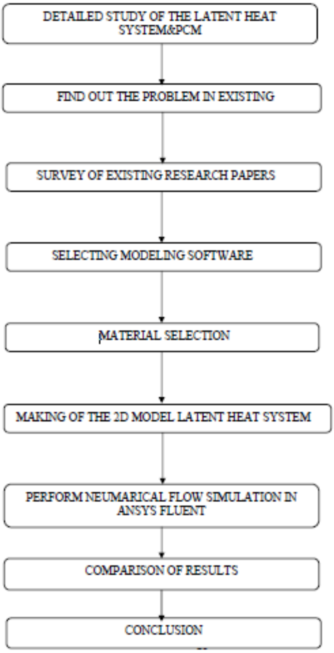

Fig. 1 Research methodology

4. Design configuration

A cross section of the shell-and-tube LHTES unit is considered. LHTES is made of copper. Water flows through the inner pipe while the PCM fills the external shell. The pipe has an external diameter of 13 mm, while the shell has a diameter of 30 mm. The charging process was considered in the analysis. That is, the PCM melting process. In such a case, PCM is initially solid and at temperature below the melting point. When water flows through the pipe at a temperature higher than the PCM melting point then heat is transfer to the PCM delivered. The process proceeds until PCM is completely melts and the energy is stored in PCM. A paraffin wax (n-octadecane) was considered as PCM. Its thermo-physical properties are listed below Design of the latent heat storage system is created with help of Ansys design modeler.

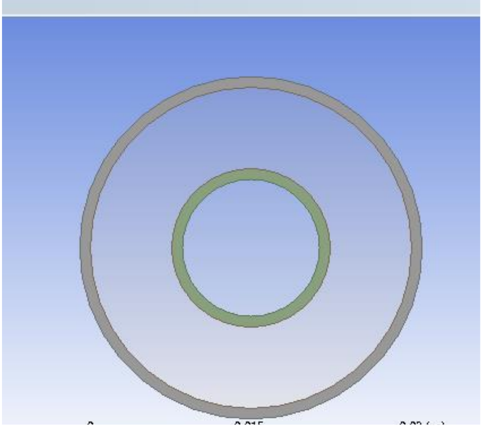

Fig 2. Design of latent heat storage system

Properties of phase changing material (PCM) are treated as temperature dependent by adopting polynomial and power law functions. The temperature dependent properties are PCM are taken from J.C.Kuria et al. /Applied Thermal Engineering 50 (2013) 896-907 [14].

4.1 Properties of Paraffin Wax:

- The density **ρpcm** is given by **$\rho pcm = 750/(0.001(T-319.15)+1)$** ,where T is the temperature of PCM.
- Thermal conductivity of PCM is estimated by **K_{pcm} = [0.21 if $T<Tsolidius$ or 0.12 if $T>Tliquidius$].**
- The PCM viscosity is defined as **$\mu pcm = 0.001\exp(-4.25+1790/T)$.**
- Specific heat **C_p = 2890 J/Kg K.**

- Melting point of PCM = **28 to 30ºC.**

Properties that depend on temperature were fed as user defined function.

4.2 Assumptions for Simulation:

For carrying out numerical simulations, some assumptions are made and simplifications are applied to the system. The liquid phase of PCM is considered as incompressible, Newtonian, homogenous, and isotropic medium, and the radiation heat transfer is considered negligible as compared to natural convection heat transfer. The buoyancy force due to temperature-dependent density variations during the melting of PCM is modeled by Boussinesq approximation. Considering Boussinesq approximation, the volume expansions of the PCM are also neglected, and natural convection is assumed laminar . The two-dimensional enthalpy porosity method is used to solve the problem numerically.

Set of under relaxation factors that is suitable to avoid divergence, for pressure, density, body forces were 0.3, 0.8, 1, while momentum, liquid fraction and energy were 0.3, 0.1, and 0.9. (from soibam J 2017) .

At step of solution the pressure was corrected using PRESTO scheme and pressure velocity coupling is implemented by semi implicit pressure linked equation (SIMPLE) algorithm .

4.3 Boundary conditions:

The initial temperature of the system for all cases was assumed to be298k. The outer wall is assumed to thermally insulated. Hot fluid(water) enters the storage at 305k.

5. Liquid Fraction Contours for Stationary Case:

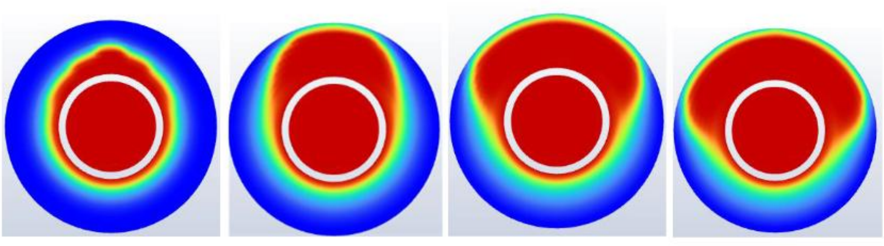

Time = 500 s. Time = 1000 s. Time = 2000 s. Time = 3000 s.

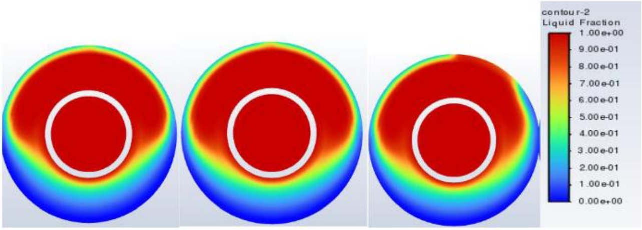

Time = 4000 s. Time = 5000 s. Time = 6000 s.

Fig. 3 Liquid Fraction Contours for Stationary Case

Temperature Contours for Stationary Case:

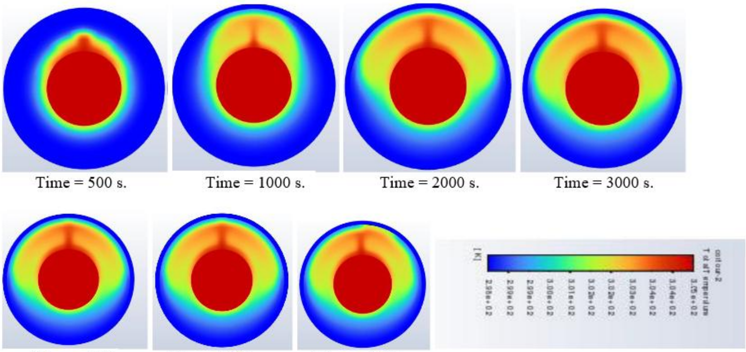

Time = 500 s. Time = 1000 s. Time = 2000 s. Time = 3000 s.

Time = 4000 s. Time = 5000 s. Time = 6000 s.

Fig 4. Temperature Contours for Stationary Case

Liquid Fraction Contours for 0.5 Rpm Rotation Case:

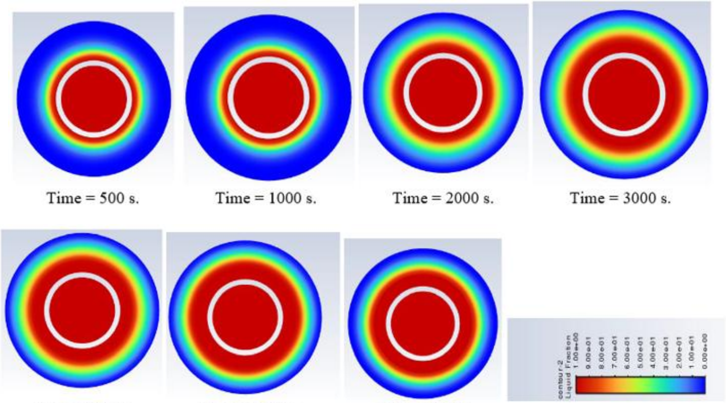

Time = 500 s. Time = 1000 s. Time = 2000 s. Time = 3000 s.

Time = 4000 s. Time = 5000 s. Time = 6000 s.

Fig. 5 Liquid Fraction Contours for 0.5 rpm Rotation Case

Temperature Contours for 0.5 rpm Rotation Case:

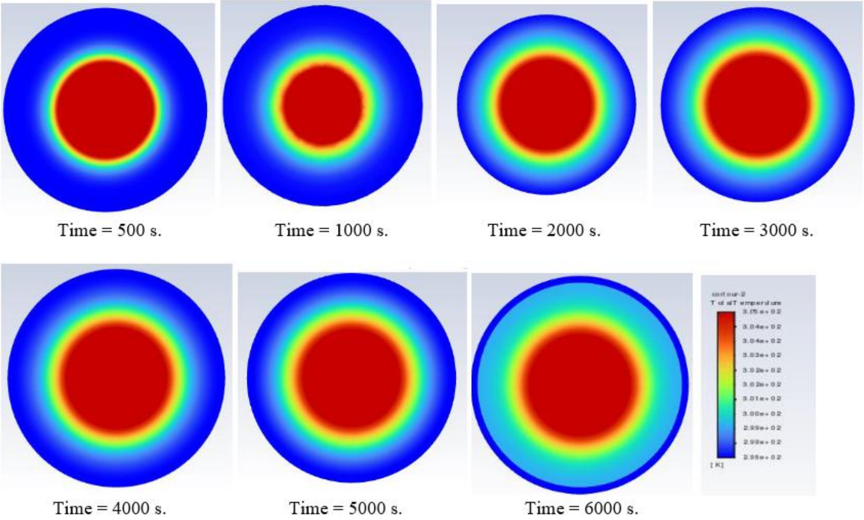

Time = 500 s. Time = 1000 s. Time = 2000 s. Time = 3000 s.

Time = 4000 s. Time = 5000 s. Time = 6000 s.

Fig. 6 Temperature Contours for 0.5 rpm Rotation Case

Liquid Fraction Contours for 1rpm Rotation Case:

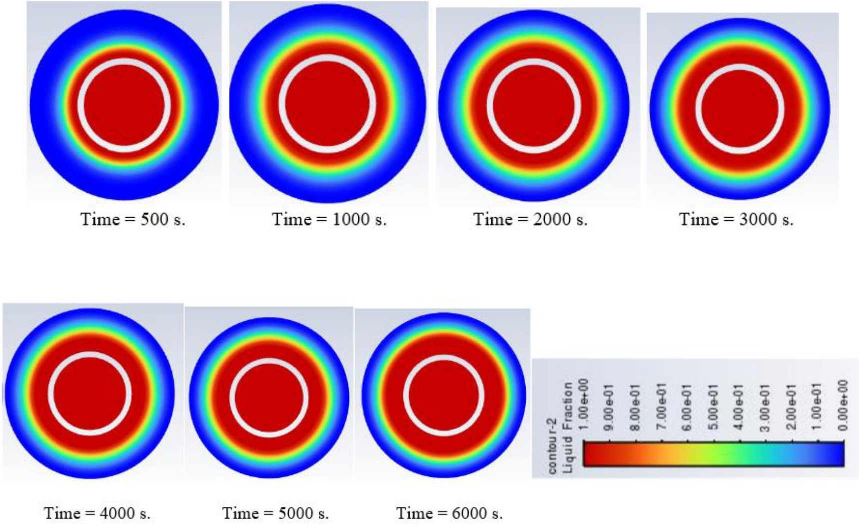

Time = 500 s. Time = 1000 s. Time = 2000 s. Time = 3000 s.

Time = 4000 s. Time = 5000 s. Time = 6000 s.

Fig. 7 Liquid Fraction Contours for 1rpm Rotation Case

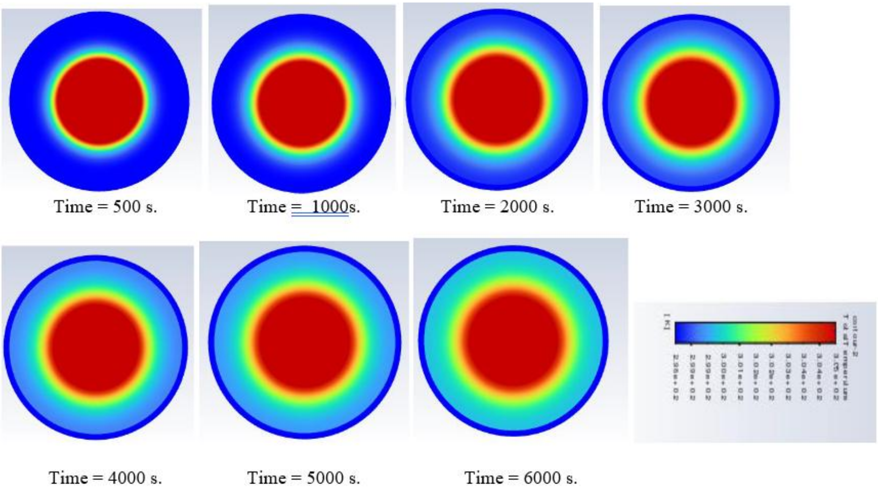

Time = 500 s. Time = 1000s. Time = 2000 s. Time = 3000 s.

Time = 4000 s. Time = 5000 s. Time = 6000 s.

Fig. 8 Temperature Contours for 1 rpm Rotation Case

Liquid Fraction Contours for 1.5 rpm Rotation Case:

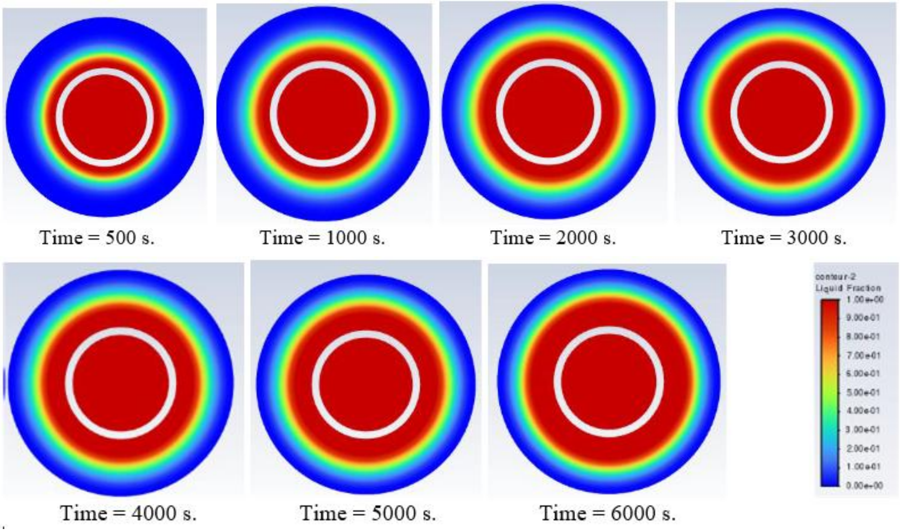

Time = 500 s. Time = 1000 s. Time = 2000 s. Time = 3000 s.

Time = 4000 s. Time = 5000 s. Time = 6000 s.

Fig. 9 Liquid Fraction Contours for 1.5 rpm Rotation Case

Temperature Contours for 1.5 rpm Rotation Case:

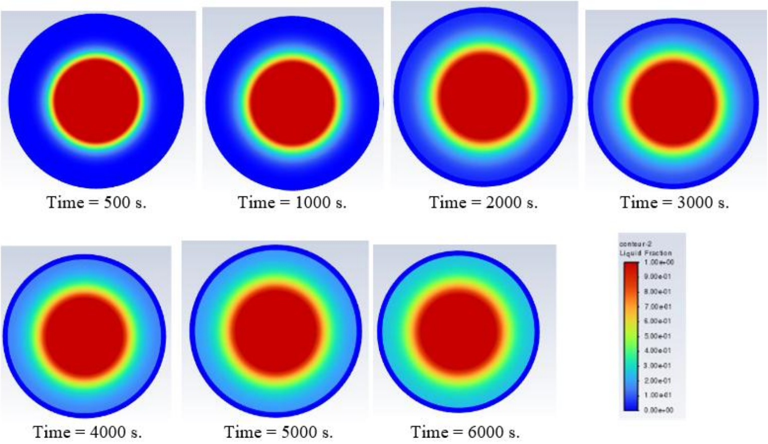

Time = 500 s. Time = 1000 s. Time = 2000 s. Time = 3000 s.

Time = 4000 s. Time = 5000 s. Time = 6000 s.

Fig. 10 Temperature Contours for 1.5 rpm Rotation Case

6. Table1: Volume Average of Liquid Fraction for Different Rotation Speed and Stand still Case:

S.No	Time (s)	Stand still case (0 rpm)	Rotation With (0.5 rpm)	Rotation With (1rpm)	Rotation With (1.5 rpm)
1	500	0.240	0.200	0.222	0.232
2	1000	0.343	0.318	0.328	0.331
3	2000	0.411	0.442	0.463	0.487
4	3000	0.515	0.528	0.530	0.613
5	4000	0.573	0.637	0.658	0.672
6	5000	0.641	0.662	0.715	0.746
7	6000	0.650	0.702	0.771	0.815

7. Calculation of Percentage of Thermal Enhancement

Percentage of Thermal Enhancement = liquid fraction of rotation - liquid fraction of stand still/liquidfraction of stand still*100

- Volume average of liquid fraction for stand stand still case = 0.650
- Volume average of liquid fraction for rotation with 0.5 rpm= 0.702
- Volume average of liquid fraction for rotation with 1 rpm = 0.771
- Volume average of liquid fraction for rotation with 1.5 rpm = 0.815

Percentage enhancement between stand still and rotation with 0.5 case = 0.702–0.650 *100/ 0.650

Percentage enhancement between stand still and rotation with 0.5 rpm case = 8%

Percentage enhancement between stand still and rotationwith1rpm case = 0.771–0.650 *100 /0.650

Percentage enhancement between stand still and rotation with 1 rpm case = 18.61%

Percentage enhancement between stand still and rotationwith1.5 rpm case = 0.815–0.650 *100 /0.650

Percentage enhancement between stand still and rotation with 1.5 rpm case = 25.38%

8. Graph:

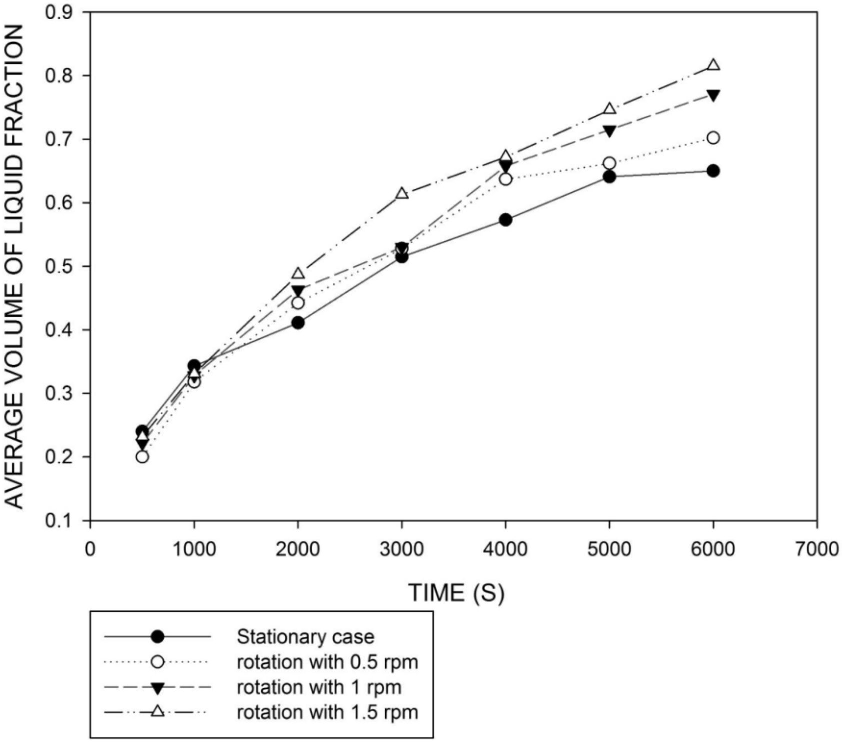

Fig. 11 Time Vs Volume Average of Liquid Fraction

9. Result and Discussion:

Stand stand still case

From the contours , when the hot water flows through hot fluid tube, the phase changing material starts melting. At, the beginning small layer of molten PCM is formed around the hot fluid tube. As, the melting goes on PCM is heated, it expands and become less dense, causing it to rise. As it rise, it carries heat away from the heat source and transfer it to cooler regions of the PCM. At the same time ,cooler, denser PCM sinks down to replace the rising molten PCM. This result in faster melting of PCM in the upper region of storage unit. The effect of buoyancy is negligible in the lower region of storage unit. The heat transfer in the lower region of the system is mainly due to conduction. Hence the melting is slow in region below the hot fluid tube. In stand still case the natural convection makes the molten PCM to rise on the upper region of latent heat storage unit. Thus a high rise in temperature is noted on the upper half of latent heat storage unit .

Rotation case

Rotation is implemented to enhance the heat transfer. In this study three rotational speeds are evaluated 0.5 rpm, 1 rpm,1.5 rpm. Performances of these cases are compared with stationary case. Rotation seems to have negative effect on the beginning of melting of PCM. In rotation latent heat storage system, the phase changing material (PCM) is subjected to centrifugal forces due to rotation of system. This can result in an angular component of the PCM, which affects the heat transfer and melting process of the PCM. Because of centrifugal forces on PCM, the PCM is pushed outwards towards the outer wall of the system. Once the sufficient melted liquid PCM available (time = 2000 s.) because of rotation, molten PCM starts circulating in the system. The rotation promote mixing of PCM. This helps to eliminate any regions of PCM that are cooler or denser than others. This result in more uniform melting of PCM in the latent heat storage system. The effectiveness of this method is calculated by percentage of thermal enhancement between stand still case and rotation case. The percentage of thermal enhancement between stand still case and rotation case for 0.5 rpm, 1 rpm and 1.5 rpm are 8%, 18.61% and 25.38% respectively. When the faster rotational speed is given the parasitic load will be higher and the advantage of having rotation may vanish. Hence the rotational speed should be maintain low to minimize parasitic load for rotating latent heat storage system.

10. Conclusion

A shell and tube latent heat storage system was numerically studied to inspect the effect of rotation in the melting process. The system was simulated as 2D model. ANSYS FLUENT 2022 VERSION R2 was used to simulate and calculate the solution. The system was studied with three different rotational speeds 0.5 rpm, 1 rpm and 1.5 rpm as well as stand still case. Paraffin wax (n-octadecane) was used as PCM while the water is used as hot tube fluid. The conclusions drawn from the study are:

- Rotation will have negative effect until sufficient amount of molten PCM is formed.
- When enough molten PCM is formed because of rotation the molten PCM starts circulating, this promotes of mixing of PCM. This helps to eliminate any regions of PCM that are cooler or denser than others.
- This result in more uniform melting of PCM in the latent heat storage system.
- The percentage of enhancement for 0.5 rpm,1 rpm and 1.5 rpm are 8%, 18.61% and 25.38% respectively for 6000 seconds of charging process.

References: **1.** *Digant S. Mehta, Bhavesh Vaghela, Manish K. Rathod & Jyotirmay Banerjee* (2019): Heat transfer intensification in horizontal shell and tube latent heat storage unit, Numerical Heat Transfer **2.** *Jundika Candra Kurnia, A. Sasmito* (2017); Investigation of heat transfer on rotating latent heat storage system. **3.** *Rathod M.K., Banerjee J.*, Thermal performance enhancement of shell and tube Latent Heat Storage Unit using longitudinal fins, Appl. Therm. Eng. 2015; **75**:1084–1092. **4.** *Ranjbar A.A., Kashani S., Hosseinizadeh S.F., Ghanbarpour M.*, Numerical heat transfer studies of a latent heat storage system containing nano-enhanced phase change material, Therm. Sci. 2011; **15(1)**;169–181. **5.** *Kurnia J.C., Sasmito A.P., Jangam S.V., Mujumdar A.S.*, Improved design for heat transfer performance of a novel phase change material (PCM) thermal energy storage (TES), Appl. Therm. Eng. 2013; **50(1)**: 896–907. **6.** *Kurnia J.C., Sasmito A.P., Mujumdar A.S.* Evaluation of heat transfer performance of helical coils of non-circular tubes. J. Zhejiang. Univ-Sci. A. (Appl Phys. & Eng.) 2011;.**12(1)**:63–70. **7.** *Alireza Jaberi Khosroshahi, Siamak Hossainpour* (2021): Investigation of storage rotation effect on phase change material charging process in latent heat thermal energy storage system **8.** *M.M. Joybari, F. Haghighat, S. Seddegh, A.A. Al-Abidi*, Heat transfer enhancement of phase change materials by fins under simultaneous charging and discharging, Energy Convers. Manag. 152 (2017) 136–156, **9.** *M. Al-Jethelah, S.H. Tasnim, S. Mahmud, A. Dutta*, Nano-PCM filled energy storage system for solar-thermal applications, Renew. Energy **10.** *M. Gorzin, M.J. Hosseini, M. Rahimi, R. Bahrampoury*, Nano-enhancement of phase change material in a shell and multi-PCM-tube heat exchanger, J. Energy Storage 22 (2019) 88–97 **11.** *Soibam, J.*, 2017. Numerical Investigation of a Heat Exchanger using Phase Change Materials (PCMs), (October). **12.** *Senthil, R., and Cheralathan, M.*, 2016. Melting and Solidification of Paraffin Wax in a Concentric Tube PCM Storage for Solar Thermal Collector, International Journal of Chemical, 14(4), pp. 2634–2640. Available at: http://www.tsijournals.com/abstract/melting-and-solidification-of-paraffin-wax-in-a-concentric-tube-pcm-storage-for-solar-thermal-collector-12762.html. **13.** *Selimefendigil, F., and Öztop, H. F.*, 2020. Mixed convection in a PCM filled cavity under the influence of a rotating cylinder, Solar Energy, Elsevier, 200(March), pp. 61–75. DOI: 10.1016/j.solener.2019.05.062. **14.** *Li, W., and Kong, C.*, 2014. Numerical study on the thermal performance of a shell and tube phase change heat storage unit during melting process, Advances in Mechanical Engineering, 2014. DOI: 10.1155/2014/360283.

А.Г. Гуна, М. Судхаршан, Салем, Індія

АНАЛІЗ ПРОДУКТИВНОСТІ ОБЕРТОВОЇ СИСТЕМИ НАКОПИЧЕННЯ ПРИХОВАНОГО ТЕПЛА

Анотація. *В останні роки для зберігання енергії використовуються кожухові та трубчасті приховані теплові системи накопичення теплової енергії (LHTESS) з матеріалами, що змінюють фазу (PCM). Основним недоліком прихованої системи накопичення тепла є те, що через низьку теплопровідність PCM теплопередача низька. У даному дослідженні розглядається 2-вимірна горизонтальна оболонка і трубчаста система прихованого зберігання тепла, обертання якої реалізовано для прискорення процесу зарядки системи. Для моделювання та розрахунку використовується програмне забезпечення ANSYS FLUENT2022 R2. Парафін (n-октадекан) і вода використовуються як PCM і гаряча рідина (HTF) відповідно. Для проведення чисельного моделювання робляться деякі припущення і застосовуються спрощення до системи. Рідка фаза PCM розглядається як нестисливе, ньютонівське, гомогенне і ізотропне середовище, а радіаційна теплопередача вважається незначною в порівнянні з природним конвекційним теплообміном. Сила плавучості через зміну щільності в залежності від температури під час плавлення PCM моделюється за допомогою наближення Буссінеска. З огляду на наближення Буссінеска, обсягними розширеннями PCM також нехтують, і природна конвекція приймається ламінарною. Для розв'язання задачі чисельним способом використовується метод двовимірної ентальпійної пористості. Моделювання та розрахунок проводяться для 0,5 об/хв, 1 об/хв та 1,5 об/хв і ці результати порівнюються зі стаціонарним аналогом . Отримані результати показують, що обертання прискорює процес плавлення. Висновки, зроблені в результаті дослідження свідчать про те, що обертання матиме негативний ефект до тих пір, поки не утвориться достатня кількість розплавленого PCM. Коли в результаті обертання утворюється достатня кількість розплавленого PCM, розплавлений PCM починає циркулювати, це сприяє перемішуванню PCM. Це допомагає усунути будь-які області PCM, які є холоднішими або щільнішими за інші. Це призводить до більш рівномірного плавлення PCM в прихованій системі накопичення тепла. Відсоток посилення для 0,5 об/хв, 1 об/хв та 1,5 об/хв становить 8%, 18,61% та 25,38% відповідно за 6000 секунд процесу заряджання.*

Ключові слова: *обертова система накопичення прихованого тепла; ANSYS; парафін (н-октадекан).*

ISSN 2078-7405 Cutting & Tools in Technological System, 2025, Edition 103

UDC 621.951 **doi: 10.20998/2078-7405.2025.103.03**

RESEARCH OF THE PROCESS OF DRILLING HOLES IN PARTS MADE OF POLYMER CARBON PLASTIC

Victor **Antonyuk** [0000-0003-0690-2411], Sergii **Vysloukh** [0000-0002-2204-2602],
Oksana **Voloshko** [0000-0002-1067- 2615]

National Technical University of Ukraine "Igor Sikorsky Kyiv Polytechnic Institute", Kyiv, Ukraine
victor.antoniuk@gmail.com

Received: 10 November 2025/ Revised: 19 November 2025/ Accepted: 29 November 2025 / Published: 15 December 2025

Abstract. *The article presents analytical models for evaluating the process of drilling holes in parts made of fibrous composite materials by drilling, which is accompanied by unusual defects that are not typical for metal cutting, such as delamination, chips, hairiness, composite chipping, thermal destruction and uncut fibers around the drilled hole, as they affect the service life of composite details. The influence of processing conditions and modes (feed, spindle speed and drill tip angle) of carbon fiber on the drilling quality parameters (delamination coefficient and roughness of the machined surface) and axial cutting force is established. The delamination coefficient (K_{sr}) in composite materials was taken into account, for which the critical axial force was determined, the excess of which leads to delamination of the hole surface, by an indirect method - by measuring the axial force. Measurement of the axial force and determination of its parameters were performed using an experimental setup. The machining modes during experimental studies varied within the following limits: the number of revolutions n - from 1250 to 4000 rpm and the feed S - from 50 to 800 mm/min. Drilling was performed on a vertical milling machine with a CNC SMG-300 with a maximum spindle speed of 5000 rpm. carbide drills with a diameter of 5 mm SANDVIK class ISO K20. Analytical dependencies were constructed using modern methods of multivariate statistical analysis - by the method of group consideration of arguments for calculating the quality parameters of holes in composite materials from cutting modes: the number of revolutions of the drill n, the feed S and the angle φ at the tip of the drill. An optimization problem of nonlinear programming was solved where the material removal rate was chosen as the optimality criterion. The value of the optimal mode for drilling holes in carbon fiber with a carbide drill VK8 with a diameter of 5 mm with an angle at the edge $2\varphi = 100°$ ($V = 2.83$ m/min, $S = 406.26$ mm/min) was established, which ensures maximum hole processing performance. The results of the study are the practical importance for mechanical engineering and the aviation industry, as they allow to increase the stability and productivity of technological processes for manufacturing products from composite materials.*

Keywords: *Composite materials; drilling; carbon fiber plastics; quality parameters; delamination; roughness; experimental researches; experimental setup; axial cutting force; modeling; optimization.*

1. Introduction

Fibrous polymer composite materials, such as carbon fiber and fiberglass, are widely used in various branches of modern instrument and mechanical engineering, in particular in the aircraft industry [1, 2], due to their unique physical and mechanical properties.

Composite materials are characterized by high strength, stiffness, corrosion resistance, low coefficient of thermal expansion, improved fatigue performance during operation, electrical insulation properties and anisotropy, which allows you to control the properties of the final product by changing the number of fibers, their orientation and the type of layer arrangement. Polymer composite materials with carbon fibers and a flexible epoxy resin matrix have become particularly widespread [3].

2. Problem statement

Despite the high physical and mechanical performance of multilayer composite materials, their use in various industries, especially in aircraft construction, requires taking into account the peculiarities of drilling polymer composite materials, which is accompanied by the occurrence of specific geometric defects, including uncut fibers, delamination, hairiness, chipping of the composite, shrinkage of the material, as well as thermal destruction and high roughness of the machined surface.

Therefore, an urgent task is to study the process of processing composite materials by modeling the quality parameters of the process of drilling holes in details made from polymer composite materials for its optimization.

3. Literature review

For critical structures made from composite materials, drilling is used, which is accompanied by unusual defects inherent in metal cutting, such as delamination, chips and uncut fibers around the drilled hole. The presence of such defects leads to the formation of gaps between parts, as a result of which the connections of structures are weakened, which is unacceptable for the general requirements of mechanical engineering [4]. This is due to such characteristics of the material as heterogeneity, anisotropy, the presence of highly abrasive reinforced fibers, the combination of hard abrasive fibers with a soft matrix [5].

The widespread use of composite materials in obtaining holes for fasteners requires ensuring high-quality holes for connections between details and increasing the efficiency of the drilling process, which is possible by determining the optimal cutting modes [6].

The machinability of composite materials can be analyzed using: axial cutting force, torque, roughness of the machined surface, delamination of the hole, the degree of uncut fibers and tool wearing out [7].

These parameters are influenced by cutting modes (feed and speed), properties of the workpiece material and tool material. Intensification of these modes leads to an increase in cutting force and increased tool wearing out. In the process of drilling composite materials, axial force can lead to delamination and interlayer cracking at the exit of the hole, where the low thickness of the layered material provides less resistance to tool penetration [8]. At the same time, a higher cutting speed allows for better hole quality.

Surface roughness is one of the main characteristics in the drilling process of composite materials, which is used to analyze the quality of the machined surface by studying the microroughness of the detail's surface, which is most often estimated by the parameters R_a and R_z [7, 8].

4. Materials and Methods

To implement the tasks of researching the quality of machined hole surfaces in polymer composite materials, drilling efficiency indicators were considered, since they affect the service life of composite details. During the drilling of polymer composite materials, various defects can be formed, such as delamination, damage to the surface layer, high roughness of the machined surface, dimensional error and deviation from roundness [9].

Delamination is the most common defect during drilling of composite materials. This quality parameter is divided into delamination at the entrance of the cutting tool into the material and delamination at the exit from it. There are many ways to assess the quality of the hole for fiber-reinforced polymers, including delamination and uncut fibers. One of the methods for non-destructive assessment of the drilled holes quality is the analysis of the hole exit in carbon fiber plastics, which is a simple measured variable that reflects the quality of the hole. [10].

The most common characteristic of the delamination parameter when drilling composite materials is the delamination coefficient (K_{sr}), proposed by Chen [11], the value of which is determined by the formula:

$$K_{sr} = \frac{D_{max}}{D}$$

where $D_{\max}$ is the maximum diameter of the hole with the damaged area; D is the nominal diameter of the hole. To analyze delamination in composite materials, Ho-Cheng used a fracture mechanics approach [12]. To do this, they determine the critical axial force P_{caf} , exceeding which leads to delamination of the hole surface.

This parameter relates delamination to the properties of the composite material according to the following formula:

$$P_{caf} = \pi\sqrt{\frac{8G_{Ic}E_1h^3}{3(1-\upsilon_{12}^2)}}$$

where G_{Ic} is the interlayer fracture toughness, J/m^2; E_1 is the modulus of elasticity, N/m^2; h - the thickness of the uncut layer of the workpiece, mm; υ_{12} - Poisson's ratio. Compared to other fibrous polymer composite materials, carbon fiber composites are most prone to delamination, which is accompanied by an excess of the critical axial force, although their interlaminar fracture toughness is lower (Table 1). This is due to the fact that these materials have a higher elastic modulus [13].

Table 1 – Critical axial force for carbon fiber composites, fiberglass composites and hybrid composites at a layer thickness of h = 0.5 mm.

Material	G_{Ic}, J/m^2	E_1, GPa	υ_{12}	P_{caf}, N
Carbon fiber	290	150	0,25	391
Fiberglass	568	25	0,18	220
Hybrid material	299	52,5	0,20	231

To obtain mathematical dependencies of the parameters of the quality of processing holes in composite materials, corresponding experimental researches were conducted.

5. Experiments

In the experimental researches, carbon fiber composite with a carbon fiber content of 50% with an orientation of 0/90° was used as the processing material [14]. The matrix material was epoxy resin LY564 and hardener HY 564 manufactured by Huntsman Co. The total thickness of the composite material was 8±0.1 mm and contained 32 layers with a thickness of 0.25 mm. The carbon fiber composite was manufactured using the transfer molding technology (RTM). The workpiece was a sheet of material 160 mm × 160 mm × 8 mm, which was cut into bars 20 mm wide for further processing. In the experimental researches, carbon fiber composite with a carbon fiber content of 50% with an orientation of 0/90° was used as the processing material.

The total thickness of the composite material was 8±0.1 mm and contained 32 layers with a thickness of 0.25 mm.

The holes were drilled on a vertical milling machine with a CNC SMG-300 with a maximum spindle speed of 5000 rpm. As a cutting tool, carbide drills with a diameter of 5 mm SANDVIK class ISO K20 were used.

The angles at the apex 2φ of the drills were 60º, 100º and 140º, they were formed by the grinding operation.

To measure the axial force signal, the workpiece was mounted on a four-component piezoelectric dynamometer Kistler 9272, which in turn was fixed on the machine table. The experimental data were transmitted via an RS-232C data interface using three Kistler 5070A amplifiers and processed on a PC using the corresponding DynoWare software from Kistler. The surface roughness of the machined holes, according to the parameter R_a, was measured using a Perthometer M2. The base length value was 0.8 mm..

The value of the delamination coefficient was determined by photographing the drilled hole using a microscope with a 500-fold magnification, on which a camera was installed.

The maximum diameter of the hole was calculated by processing images using the LabView v. 6 system.

The study of the process of drilling holes with measurement of axial force and determination of its parameters was performed using an experimental machine. The general scheme of the experimental machine for studying the process of drilling carbon fiber parts is shown in Figure 1

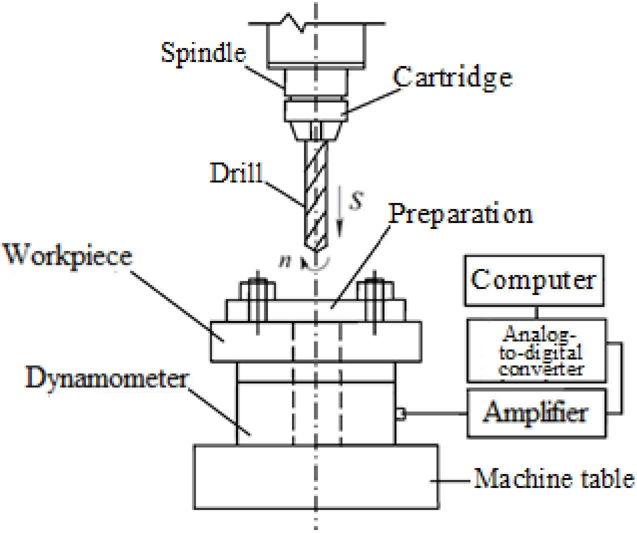

Figure 1 – Scheme of the experimental machine for studying the drilling process of carbon fiber parts

The purpose of experimental research on the drilling process of carbon fiber parts is to study the influence of processing conditions and modes (feed, spindle speed and drill tip angle) on the parameters of carbon fiber drilling quality (layering coefficient and roughness of the machined surface) and axial cutting force. The processing modes during the research varied within the following limits: speed n – from 1250 to 4000 rpm and feed S – from 50 to 800 mm/min.

6. Results

Processing of the results of experimental studies to obtain the corresponding mathematical models was performed using modern effective methods of multivariate statistical analysis [15].

Using the GMDH Shell DS software, which implements the advantages of group argument accounting methods (MGAA), mathematical dependences of quality parameters on the number of revolutions of the drill n, feed S and sharpening angle φ at the tip of the drill were obtained [16].

When obtaining the mathematical dependence of the axial force $P = f(n, S, \varphi)$ on the number of rotations, feed and angle at the tip of the drill, 25% of the initial data were used as a test sample to assess its accuracy.

As a result, the following dependence was obtained with a coefficient of determination R^2 = 0.994 on the test sample:

$$\begin{gathered}
P = 0{,}37403531 \cdot S + 0{,}80636969 \cdot \varphi - 0{,}042552536 \cdot n + \\
+2{,}5174804 \cdot 10^{-3} \cdot S \cdot \varphi - 1{,}1838289 \cdot 10^{-4} \cdot S \cdot n \\
- 2{,}8640392 \cdot 10^{-4} \cdot \varphi \cdot n - \\
-6{,}6437653 \cdot 10^{-7} \cdot S \cdot \varphi^2 + 1{,}5512999 \cdot 10^{-8} \cdot S \cdot n^2 + \\
+3{,}7530623 \cdot 10^{-8} \cdot \varphi \cdot n^2 + 7{,}5583524 \cdot 10^{-8} \cdot \varphi^2 \cdot n - \\
-1{,}983767 \cdot 10^{-4} \cdot \varphi^2 + 5{,}5761222 \cdot 10^{-6} \cdot n^2 - 9{,}9045321 \\
\cdot 10^{-12} \cdot \varphi^2 \cdot n^2 - \\
-2{,}7554812 \cdot 10^{-14} \cdot S \cdot \varphi^2 \cdot n^2 - 7{,}9678736 \cdot 10^{-7} \cdot S \cdot \varphi \cdot n \\
+ \\
+1{,}0441172 \cdot 10^{-10} \cdot S \cdot \varphi \cdot n^2 + 2{,}1027644 \cdot 10^{-10} \cdot S \cdot \varphi^2 \cdot n \\
+ 99{,}778598
\end{gathered}$$

Since it is practically impossible to measure the value of the delamination coefficient during the machining process, it is proposed to determine this parameter by an indirect method - by measuring the axial force. For this purpose, the dependence $K_{del}=f(P)$ was obtained, which allows determining the value of the delamination of the hole in the processed material by the value of the axial cutting force.

A similar approach is also proposed to be performed to determine the roughness of the hole surface.

To obtain an analytical dependence of the delamination coefficient, a 5th order polynomial regression was used based on the results of experimental studies:

$$K_{del} = 1{,}58379455006 \cdot 10^{-12}P^5 - 1{,}7774707523 \cdot 10^{-9}P^4 + \\ +7{,}0153442442 \cdot 10^{-7}P^3 - 1{,}17101594923852 \cdot 10^{-4}P^2 + \\ +8{,}83914402978316 \cdot 10^{-3}P + 0{,}788058618989498$$

The quality of the obtained dependence $K_{del}=f(P)$ is confirmed by the accuracy parameters: average absolute error – 0.0351; average square error – 0.003; average relative error – 2.8941%; coefficient of determination R^2 – 0,9296.

To control the roughness parameter of the machined surface by the value of the axial cutting force, based on the results of experimental studies, a mathematical model of the dependence of roughness on the axial force $Ra = f(P)$ was obtained,

By the SPSS Statistics software, the curves of graphical dependences were compared using the regression module to obtain an analytical dependence that best describes the statistical data [17]. It was determined that the power form of the regression equation most accurately approximates this dependence best describes

$$Ra = 0{,}0898P^{0{,}5064}$$

statistical data with the following accuracy parameters: average absolute error – 0,2031; average square error – 0.069; average relative error – 15.6206%; coefficient of determination R^2 – 0,7419.

The developed mathematical dependencies of the quality parameters of the hole surfaces (delamination and roughness) are convenient to use for predicting these parameters when drilling holes in carbon fiber parts and as a constraint in the general mathematical model of the drilling process when solving the optimization problem. At the same time, these mathematical dependencies are adequate for the following processing modes: the number of rotations n - from 1250 to 4000 rpm and the feed S - from 50 to 800 mm/min.

Optimization of the conditions and modes of processing of composite materials involves solving various technological, structural, economic and organizational problems. For this, the following optimality criteria are used: the criterion of minimum cost; the criterion of maximum efficiency (productivity), which ensures the minimization of the time spent on mechanical processing; criteria of quality and accuracy of processing, etc.

As an example of solving the optimizing problem the drilling process in carbon fiber parts, which provides the necessary parameters of the quality of the holes, the maximum productivity N of this process was chosen as the criterion.

Therefore, the task of solving the optimization problem of nonlinear programming, which is built on a model where the material removal rate is chosen as the optimality criterion [17].

$$max \quad N = \frac{(m_w - m_p)}{\rho \cdot t}, \quad t = \frac{l \cdot n}{S} \quad \rightarrow \quad max \quad N = \frac{(m_w - m_p)S}{\rho \cdot t},$$

where m_w – mass of the workpiece, kg;

m_p – weight of the part, kg;

ρ – material density, kg/mm^3;

t – processing time, min.

l – cutting path when drilling one hole, mm;

n – number of holes;

S – drill feed, mm/min.

In this case, a set of restrictions is set on the parameters of the quality of the hole surfaces and the capabilities of the equipment used:

$$P=f(n,S,\varphi)\leq 138;$$

$$K_{sr}=f_1(n,S,\varphi)\leq 1,1;$$

$$R_a=f_2(n,S,\varphi)\leq 1,6;$$

$$50\leq S\leq 800;$$

$$1250\leq n\leq 4000$$

Thus, as a result of experimental research and solving the problem of optimizing the process of drilling holes in carbon fiber with a VK8 carbide drill with a diameter of 5 mm and an angle at the apex of 2φ = 100°, the value of the optimal drilling mode (V = 62.83 m/min, S = 406.26 mm/min) was obtained, which ensures maximum hole processing performance.

7. Discussion

According to the results of experimental researches, it was found that the roughness of the machined surface of the holes increases with increasing feed and decreases with increasing drill speed. In addition, by comparing the obtained models, it can be concluded that the angle at the tip of the tool does not have a clearly defined effect on the R_a parameter.

The studies have shown that the values of the axial force and the delamination coefficient can be minimized at high spindle speeds and reduced feed values.

Modern production is focused not only on the quality of the finished product, but also on its manufacture with the lowest possible costs in the shortest possible time and in accordance with the specified quality indicators.

With adequate mathematical models of the parameters of the drilling process in carbon fiber parts, it is possible to determine the influence of cutting modes and conditions on the stability of the cutting process and establish optimal values of modes that provide the necessary dynamic properties.

It has been established that increasing the thickness of the material layer leads to an increase in the critical value of the axial force, which accordingly requires an increase in the values of the optimal cutting modes. The use of fiberglass or hybrid composite material as the processed material reduces the feed value and the number of revolutions of the drill, which negatively affects the productivity of the process.

Conclusions

Based on the results of the research and modeling of the parameters of the drilling process in carbon fiber parts, the following conclusions can be made.

1. As a result of the analysis of the drilling process in carbon fiber parts, it was established that the criterion parameters of the quality of the process are the delamination coefficient and the roughness of the machined surfaces, which can be determined by the magnitude of the axial cutting force.

2. A scheme of the machine for conducting experimental reserches is proposed, which allows obtaining the necessary information for creating mathematical models of quality parameters when drilling holes.

3. As a result of processing the experimental research data, mathematical dependences of the axial force, delamination coefficient and roughness of the treated surface on the cutting modes and conditions were obtained, which allow forming a mathematical model of the drilling process in carbon fiber.

4. The developed mathematical model of the process of drilling holes in carbon fiber parts makes it possible to solve the problem of optimizing cutting modes, which ensures obtaining the specified quality parameters of the resulting surfaces with the highest productivity.

References: **1**. *Abrão A.M., Faria P.E., Rubio J.C.C., Reis P., Davim J.P.* (2007) Drilling of fiber reinforced plastics: a review. J Mater Process Technol 186:1–7. https://doi.org/10.1016/j.jmatprotec.2006.11.146 **2.** *A. Mohan Kumar, R. Parameshwaran, R. Rajasekar, C. Moganapriya* & *R. Manivannan* A Review on Drilling of Fiber-Reinforced Polymer Composites Mechanics of Composite Materials Aims and scope Vol. 58, pages 97–112, (2022) https://doi.org/10.1007/s11029-022-10014-5 **3.** Formation of the quality of holes obtained by drilling inaviation structures made from polymer composite materials *Borys Lupkin, Oleksii Andrieiev, Kateryna Maiorova, Victor Antonyuk, Sergii Vysloukh* // Eastern-European Journal of Enterprise Technologies,

№3/1 (123) 2023. pp. 59–67. https://doi.org/10.15587/1729-4061.2023.279618. **4.** Recognition of drilling-induced defects in fiber reinforced polymers using machine learning *A. Hrechuk* Procedia CIRP Vol. 117, 2023,384–389 https://doi.org/10.1016/j.procir.2023.03.065 **5.** *Borys Lupkin, Oleksii Andrieiev, Kateryna Maiorova, VictorAntonyuk, Serhii Tolstoi* Experimental studies of the holes quality parameters in polymer composite materials / New Technologies, Development and Application VII.NT 2024. Lecture Notes in Networks and Systems, 2024, p. 589–602. DOI https://doi.org/10.1007/978-3-031-66268-3_60. **6.** *Olexandr Matoshyn, Sergii Vysloukh, Victor Antonyuk, Oksana Voloshko* Modelingand Optimization of the Process of Drilling holesin Carbon Fiber Reinforced Polymer Parts //Advanced Manufacturing Processes VI., 2024, pp. 300 – 310. https://doi.org/10.1007/978-3-031-82746-4_27 **7.** Recognition of drilling-induced defects in fiber reinforced polymers using machine learning *A. Hrechuk* Procedia CIRP Vol. 117, pages 384–389 (2023) https://doi.org/10.1016/j.procir.2023.03.065 **8.** Research solution for automatic hole quality analysis when drilling fiber-reinforced composites *A. Hrechuk, M. Hörndahl, F Schultheiss* The International Journal of Advanced Manufacturing Technology Vol. 127 (7), pages 3315–3324, (2023) https://doi.org/10.1007/s00170-023-11696-4 **9.** Novel metric "Implenarity" for characterization of shape and defectiveness: The case of CFRP hole quality *A Hrechuk, V Bushlya, JE Ståhl, V Kryzhanivskyy* Composite Structures Vol. 265, 113722 13 2021 https://doi.org/10.1016/j.compstruct.2021.113722 **10.** *Voß R, Henerichs M, Rupp S, Kuster F, Wegener K* (2016) Evaluation of bore exit quality for fibre reinforced plastics including delamination and uncut fibres. CIRP J Manuf Sci Technol 12:56–66. https://doi.org/10.1016/j.cirpj.2015.09.003 **11.** *Chen W.-C.* Some experimental investigations in the drilling of carbon fiber-reinforcedp lastic (CFRP) composite laminates. International Journal of Machine Toolsand Manufacture. 1997. Vol. 37, no. 8. pp. 1097–1108. URL: https://doi.org/10.1016/S0890-6955(96)00095-8 **12.** *Ho-Cheng H., Dharan C. K. H.* Delamination During Drillingin Composite Laminates. Journal of Engineering for Industry. 1990. Vol. 112, no. 3. pp. 236–239. URL: https://doi.org/10.1115/1.2899580 **13.** Mekhanichna obrobka kompozytsiinykh materialiv pry skladanni litalnykh aparativ (analitychnyi ohliad): monohrafiia / *Kryvoruchko D. V., Zaloha V. O., Kolesnyk V. O. ta in.*; pid zahalnoiu red. prof. *V. O. Zalohy*. – Sumy: Universytetska knyha, 2013. – 272 s. (in Ukrainian). https://essuir.sumdu.edu.ua/bitstream/123456789/36673/3/KryvoruchkoKomposity.pdf **14.** *Shahrajabian H., Farahnakian M.* Modeling and multi-constrained optimization in drilling process of carbon fiber reinforced epoxy composite. International Journal of Precision Engineeringand Manufacturing. 2013. Vol. 14, no. 10. pp. 1829–1837. URL: https://doi.org/10.1007/s12541-013-0245-1 **15.** *Vysloukh S.P.* Determination of process parameters of newtool, J. Superhard Mater., 2001, vol. 23, no. 5, pp. 65–69. https://www.scopus.com/pages/publications/0035550254 **16.** Informatsiini tekhnolohii v zadachakh tekhnolohichnoi pidhotovky prylado- ta mashynobudivnoho vyrobnytstva: monohr. / *S.P. Vysloukh*. – K.: NTUU „KPI", 2011. – 488 s. (in Ukrainian) https://ela.kpi.ua/bitstream/123456789/32767/3/Information_technology.pdf **17.** *Matoshyn O. V., Vysloukh S. P.* Systema avtomatyzovanoho keruvannia protsesom sverdlinnia otvoriv u detaliakh z vuhleplastyku. Seriia: Tekhnichni nauky. 2024. Tom 35 (74), №1. Ch.1. pp. 237-244. (in Ukrainian) https://doi.org/10.32782/2663-5941/2024.1.1/36.

Віктор Антонюк, Сергій Вислоух, Оксана Волошко, Київ, Україна

ДОСЛІДЖЕННЯ ПРОЦЕСУ СВЕРДЛІННЯ ОТВОРІВ В ДЕТАЛЯХ З ПОЛІМЕРНОГО ВУГЛЕПЛАСТИКУ

Анотація. *В статті представлені аналітичні моделі для оцінки процесу свердління отворів в деталях з волокнистих композиційних матеріалів свердлінням, що супроводжується незвичайними дефектами, які невластиві різанню металу, такі як розшарування, сколи, ворсистість, викришування композиту, термічна деструкція та нерозрізані волокна навколо просвердленого отвору, оскільки вони впливають на термін експлуатації композитних деталей. Встановлено вплив умов та режимів оброблення (подачі, кількості обертів шпинделя та кута при вершині свердла) вуглепластику на параметри якості свердління (коефіцієнт розшарування та шорсткість обробленої поверхні) та осьову силу різання. Враховано коефіцієнт розшарування (Ksr) в композиційних матеріалах, для чого визначали критичну осьову силу, перевищення якої призводить до розшарування поверхні отвору, непрямим методом – шляхом вимірювання осьової сили. Вимірювання осьової сили та визначення її параметрів виконували за допомогою експериментальної установки. Режими оброблення при проведенні експериментальних досліджень варіювались в межах: кількість обертів n – від 1250 до 4000 об/хв та подача S – від 50 до 800 мм/хв. Свердління виконували на вертикально-фрезерному верстаті з ЧПК SMG-300 з максимальною частотою обертання шпинделя 5000 об/хв. твердосплавними свердла діаметром 5 мм SANDVIK класу ISO K20. Побудовані аналітичні залежності з використанням сучасних методів багатовимірного статистичного аналізу – методом групового врахування аргументів для розрахунку параметрів якості отворів композиційних матеріалів від режимів різання: числа обертів свердла n, подачі S та кута φ при вершині свердла. Розв'язана оптимізаційна задача нелінійного програмування де критерієм оптимальності вибрана швидкість знімання матеріалу. Встановлено значення оптимального режиму свердління отворів у вуглепластику твердосплавним свердлом ВК8 діаметром 5 мм з кутом при вершині 2φ = 100° (V = 2,83 м/хв , S = 406,26 мм/хв), який забезпечує максимальну продуктивність оброблення отворів. Результати дослідження мають практичне значення для машинобудування та авіаційної промисловості, оскільки дозволяють підвищити стабільність та продуктивність технологічних процесів виготовлення виробів з композиційних матеріалів.*

Ключові слова: *композиційні матеріали; свердління; вуглепластики; параметри якості; розшарування; шорсткість; експериментальні дослідження; експериментальна установка; осьова сила різання; моделювання; оптимізація.*

ISSN 2078-7405 Cutting & Tools in Technological System, 2025, Edition 103

UDC 621.7 **doi: 10.20998/2078-7405.2025.103.04**

INFLUENCE OF MACHINING-BASED POST-PROCESSING ON THE SURFACE TOPOGRAPHY OF DMLS 316L STAINLESS STEEL FOR FUSION-RELEVANT APPLICATIONS

István **Sztankovics**[1*][0000-0002-1147-7475], Gábor **Veres**[2,3] [0009-0000-0708-9405], Csaba **Felhő**[1] [0000-0003-0997-666X], Antal **Nagy**[1] [0000-0001-6160-4973], Péter **Figeczki-Mélykuti**[2] [0009-0001-5454-0913]

[1]Institute of Manufacturing Science, University of Miskolc,
H-3515, Miskolc – Egyetemváros, Hungary
[2] HUN-REN Centre for Energy Research,
H-1121 Budapest, Konkoly-Thege Miklós út 29-33., Hungary
[3] Institute of Nuclear Technics, Budapest University of Technology and Economics, H-1111 Budapest, Műegyetem rkp. 3., Hungary
*istvan.sztankovics@uni-miskolc.hu

Received: 10 November 2025/ Revised: 19 November 2025/ Accepted: 29 November 2025 / Published: 15 December 2025

Abstract. *This study investigates the effect of machining-based post-processing on the surface topography of Direct Metal Laser Sintered (DMLS) 316L stainless steel intended for fusion-relevant applications. Cubic samples (30 × 30 × 30 mm) were produced by additive manufacturing and subsequently finished by face milling and surface grinding under two parameter settings each. The surface topography was characterized using an AltiSurf 520 optical system in accordance with ISO 25178. The as-printed surface exhibited high roughness (S_a = 8.899 μm, S_z = 79.427 μm), while all post-processed surfaces showed significant improvements. The lowest roughness (S_a = 1.346 μm) was obtained after grinding at 7 m/min feed rate. Skewness and kurtosis analysis indicated that machining transformed the peak-dominated surface into a more uniform, near-Gaussian texture. The results confirm that controlled milling and grinding operations can effectively enhance the surface integrity of DMLS 316L components. These findings demonstrate the potential of hybrid additive–subtractive manufacturing to produce surfaces suitable for the vacuum and functional requirements of fusion technology applications.*

Keywords: *additive manufacturing; DMLS 316L stainless steel; surface topography; post-processing; fusion technology applications.*

1. Introduction

Additive manufacturing (AM) has emerged as one of the most transformative technologies in modern engineering, enabling the production of complex components with high design freedom and material efficiency [1,2]. Among the various AM techniques, Direct Metal Laser Sintering (DMLS) has gained particular importance for producing metallic components with intricate geometries that are difficult or impossible to fabricate using traditional subtractive manufacturing methods [3,4]. In DMLS, a high-energy laser beam selectively melts fine layers of metallic powder, such as stainless steel, titanium, or nickel-based alloys, to build a part layer by layer directly from a digital model. This layer-wise approach allows for the realization of lightweight structures, internal channels, and functional gradients that are highly advantageous for advanced engineering applications [5-8]. However, despite these benefits, DMLS parts often exhibit intrinsic challenges, such as high surface roughness, porosity, and residual stresses, which can limit their use in critical technological environments [9,10].

One of the most promising areas for applying additive manufacturing is the field of fusion technology [11]. In experimental fusion devices and future reactors, such as ITER and DEMO, component design must meet demanding mechanical, thermal, and vacuum performance criteria [12,13]. The extreme conditions inside the fusion environment – characterized by high temperatures, cyclic thermal loads, radiation exposure, and ultra-high vacuum – place strict constraints on material selection and manufacturing quality. Structural and functional components within the vacuum chamber must not only maintain mechanical integrity but also exhibit low outgassing rates and high surface density to ensure vacuum compatibility [14,15]. Any surface irregularities, porosity, or contamination can significantly impair vacuum tightness and introduce sources of gas emission, thereby compromising operational stability. Therefore, before AM parts can be reliably implemented in fusion systems, their surface and subsurface characteristics must be optimized to meet these stringent requirements.

316L stainless steel is among the most widely used materials for both additive and conventional fabrication of components in vacuum and fusion environments [16,17]. It combines good mechanical strength, corrosion resistance, and non-magnetic properties with excellent weldability. When processed through DMLS, 316L retains these beneficial features but often exhibits a characteristic rough, layered surface and microstructural inhomogeneity [18,19]. These as-built surface conditions are typically unsuitable for vacuum applications, where smoothness and compactness are crucial for ensuring adequate sealing and minimizing gas entrapment. Therefore, appropriate post-processing methods must be employed to refine the surface topography, eliminate near-surface defects, and improve functional performance.

Machining-based post-processing methods, such as face milling and face grinding, represent practical and effective approaches for improving the surface quality of additively manufactured metal components [8,20]. These techniques enable the controlled removal of the rough outer layers, reducing waviness, asperity peaks, and partially melted particles originating from the DMLS process. The resulting modifications in surface topography can significantly influence the mechanical behaviour, wear resistance, and vacuum performance of the components.

However, the interaction between the machined surface and the underlying additively manufactured microstructure remains complex, as the anisotropy, porosity, and hardness variations within DMLS parts may affect machining efficiency and surface finish outcomes [21,22]. Consequently, systematic evaluation of machining-based post-processing is necessary to identify optimal processing parameters that produce surfaces suitable for fusion-related applications.

Recent literature demonstrates that post-processing is essential to render DMLS 316L surfaces suitable for demanding applications. Powder-bed fusion parts typically show high as-built roughness, partially fused particles and near-surface porosity, which can degrade fatigue performance and surface-dependent functional properties; several studies quantify these effects and show that controlled machining or polishing substantially reduces roughness and improves fatigue and breakdown behaviour [16,23]. Experimental and review papers indicate machining and other mechanical finishing methods are effective at removing the superficial, layer-induced defects, while thermal or HIP treatments can additionally close internal porosity and homogenize microstructure when required [9,24]. Importantly for fusion or accelerator vacuum applications, recent targeted evaluations found that DMLS 316L can achieve ultra-high vacuum suitability after appropriate post-processing and baking steps, with some machined samples reaching leak rates near instrument detection limits and showing pump-down behaviour comparable to wrought material [25]. Taken together, these studies motivate systematic comparisons of machining routes such as face milling and face grinding on DMLS 316L to identify parameter sets that reliably produce surface topographies compatible with fusion-relevant requirements.

The present study addresses this challenge by investigating the influence of face milling and face grinding on the surface topography of DMLS 316L stainless steel specimens. By analysing different machining parameters and quantifying their effects on areal roughness characteristics, the study aims to assess the suitability of post-processed DMLS parts for use in fusion environments. The findings contribute to defining process–structure–surface relationships that can guide the future qualification of additively manufactured metallic components in fusion technology.

2. Experimental conditions and methods

Additive manufacturing experiments were carried out using 316L stainless steel specimens produced by Direct Metal Laser Sintering (DMLS). The printing process was performed at VARINEX Zrt. using 316L stainless steel powder. The parts were manufactured in the form of small cubic samples with nominal dimensions of 30 × 30 × 30 mm. A total of five samples were produced to allow systematic comparison of different machining-based post-processing conditions. The DMLS-made parts were divided into five groups: one as-printed reference and four samples subjected to different post-processing combinations of milling and grinding parameters. The aim of this setup was to characterize the influence of machining conditions on the resulting surface topography and to identify trends in surface modification achievable through mechanical finishing. The samples were subjected to two distinct machining methods: face milling and longitudinal peripheral plane grinding. Both techniques were selected because of their industrial relevance and their different material removal mechanisms, which allow a comparative understanding of surface formation in additively manufactured metallic materials.

The face milling operations were performed on a Perfect Jet MCV-M8 vertical machining centre. The tool assembly consisted of a Tungaloy T2845 PM 063.05Z5W tool holder equipped with a BFT Burzoni OFEX 05T3AE cutting insert. The insert was manufactured from KH100-grade carbide, providing sufficient wear resistance and edge stability when cutting stainless steel. During the experiments, one insert was clamped into the toolholder. Milling was carried out under flooded lubrication using CIKS HKF 420 coolant to minimize temperature rise and to assist chip evacuation. Two parameter combinations were investigated for the milling process: both employed a cutting speed of 200 m/min and a constant depth of cut of 0.5 mm, while the feed per tooth (f_z) was varied between 0.5 mm/rev and 0.8 mm/rev. This variation allowed the assessment of feed influence on the surface texture and material removal characteristics.

The grinding operations were conducted on a Metallkraft FSM 4080 precision surface grinding machine, which ensured high rigidity and fine controllability of process parameters. A grinding wheel with an outer diameter of 343.4 mm was used. The process was performed under flooded cooling with the same CIKS HKF 420 coolant to maintain consistent lubrication and thermal conditions across both machining technologies. For grinding, the main process parameters included a rotational speed of 1450 RPM, a depth of cut of 0.05 mm, and a stroke width of 1.5 mm per pass. The feed rate (v_f) was varied at two levels, 7 m/min and 9 m/min, to evaluate its effect on the achieved surface topography. These conditions were chosen to represent typical fine-finishing operations applicable to stainless steel components.

As a result, the complete set of experiments included five surface conditions: one as-printed, two milled, and two ground surfaces. After machining, all samples underwent careful cleaning to remove coolant residues and any loosely adhered particles. No heat treatment, density testing, or vacuum qualification procedures were carried out in the present phase of the study, but these investigations are planned as part of future work to establish correlations between surface finish and vacuum compatibility. Similarly, detailed microscopic analyses, including optical or scanning electron microscopy, are also intended for the next research stage to complement the quantitative topography measurements.

Surface characterization was performed using an AltiSurf 520 three-dimensional topography measurement system. This instrument enables non-contact areal surface measurement based on optical scanning principles, providing high-resolution topographic data suitable for areal roughness parameter evaluation. The surface measurements were analysed using the AltiMap Premium v6.2.7487 software package. Each sample was measured once over an area of 4 × 4 mm, with a resolution of 1 μm times 10 μm. The evaluation of the acquired surface data followed the ISO 25178 standard for areal surface texture analysis, which allows the quantification of both amplitude and functional characteristics of surface morphology. The parameters investigated in this study included the arithmetic mean height (S_a), maximum height (S_z), skewness (S_{sk}), and kurtosis (S_{ku}). These parameters collectively describe the average roughness, the extreme height difference, and the statistical distribution of surface peaks and valleys, offering comprehensive insight into the effectiveness of post-processing operations. No averaging or statistical repetition was applied at this stage, as the study aimed primarily to identify qualitative trends and establish methodological feasibility for subsequent, more extensive experiments.

The selected methodology ensures that the observed differences in surface topography can be directly attributed to the applied machining conditions. By maintaining consistent coolant, tool, and machine configurations, while varying only the feed per tooth or feed rate, the influence of process dynamics on the surface structure of DMLS 316L stainless steel can be systematically assessed. The combination of high-precision surface measurement and controlled machining conditions provides a robust basis for understanding how additive manufactured surfaces respond to traditional subtractive finishing. The obtained data serve as the foundation for developing optimized post-processing protocols that could make additively manufactured stainless steel components suitable for integration into fusion-relevant environments, where both surface quality and structural integrity are of critical importance.

3. Results and Discussion

The corresponding quantitative roughness parameters extracted from the areal measurements are summarized in Table 1: the arithmetical mean height (S_a), the maximum height (S_z), the skewness (S_{sk}), and the kurtosis (S_{ku}).

Table 1 – Summary of the surface roughness measurement results

Process	3D printed	Milling 0.5 mm/rev.	Milling 0.8 mm/rev.	Grinding 7m/min	Grinding 9 m/min
S_a [µm]	8.899	1.726	2.244	1.346	1.666
S_z [µm]	79.427	10.246	13.936	12.045	19.023

S_{sk} [-]	0.147	-0.168	0.308	-0.261	-0.487
S_{ku} [-]	3.090	1.925	1.922	2.927	3.305

Figure 1 presents the representative 3D surface topography maps obtained from each surface preparation method: (a) as-printed, (b) milling with 0.5 mm/rev feed, (c) milling with 0.8 mm/rev feed, (d) grinding at 7 m/min, and (e) grinding at 9 m/min.

a) 3D printed

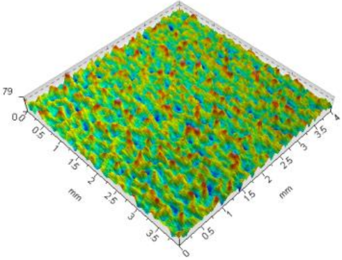

b) milled, 0.5 mm/rev.

c) milled, 0.8 mm/rev.

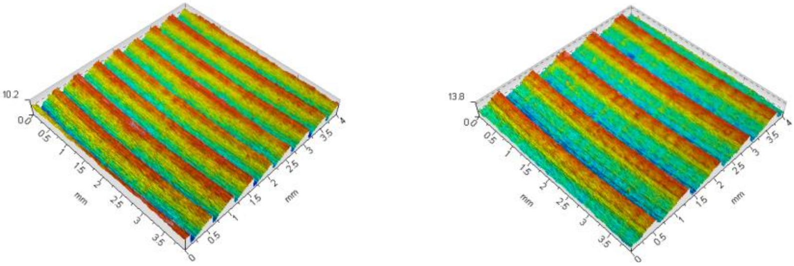

d) ground, 7 m/min

e) ground, 9 m/min

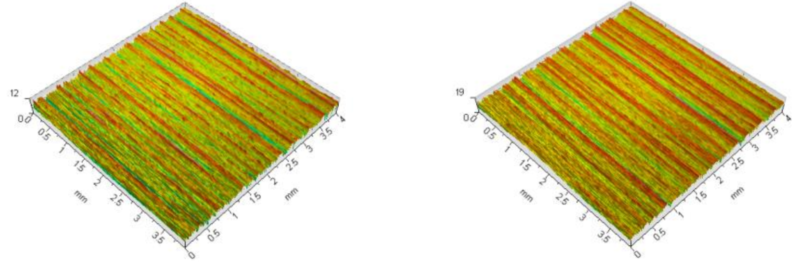

Figure 1 – Variation of the Average Height of the Waviness profile in the studied range

3.1 General trends and surface morphology

The surface topographies reveal a clear transition from the highly irregular and layered morphology of the 3D printed surface to smoother and more uniform textures obtained after milling and grinding. The as-printed surface exhibits pronounced waviness and asperities, resulting from the layer-by-layer deposition inherent in the additive manufacturing process. These height variations are quantitatively reflected in its S_a value of 8.899 µm and S_z value of 79.427 µm, both significantly higher than those of any of the subsequent subtractive processes. Such values are characteristic of typical fused deposition or powder-bed printed metallic or polymeric surfaces, where partially melted particles, stair-step effects, and inter-layer ridges dominate the microgeometry.

When the printed surfaces were subjected to milling and grinding, substantial reductions in both S_a and S_z were observed, confirming the strong smoothing effect of material removal. Among the milled samples, the surface milled at a lower feed of 0.5 mm/rev achieved the smallest S_a value (1.726 µm), while the higher feed of 0.8 mm/rev resulted in a slightly rougher texture (S_a = 2.244 µm). This trend is consistent with general machining theory, as higher feed per revolution increases the uncut chip thickness and the feed marks left by the cutting tool, thereby amplifying the surface roughness amplitude. Nevertheless, both milled surfaces exhibit an order-of-magnitude reduction in S_a compared to the as-printed sample, demonstrating the capability of milling to significantly improve surface quality in post-processing of additively manufactured parts.

The ground surfaces further improved smoothness, reaching S_a values of 1.346 µm and 1.666 µm for the 7 m/min and 9 m/min cutting speeds, respectively. The lower feed rate thus provided the finest finish, consistent with the notion that slower feed rates in abrasive processes generally allow for more controlled material removal and reduced thermal damage. The slightly higher roughness at 9 m/min may be attributed to increased thermal softening or local wheel loading, which can alter the effective cutting edges and cause ploughing rather than pure abrasion. Despite these differences, both grinding conditions resulted surfaces with S_a below 2 µm, marking a substantial refinement compared with the printed and milled conditions.

3.2 Amplitude parameters

The evolution of S_a and S_z values across the five setups reveals the dominant role of surface generation mechanisms in determining the overall amplitude characteristics. The highest values observed in the printed sample (S_a = 8.899 µm, S_z = 79.427 µm) confirm the presence of tall peaks and deep valleys. The ratio between S_z and S_a is approximately 8.9, suggesting that extreme height features significantly contribute to the overall texture, a common feature of layer-based manufacturing. The subsequent milling and grinding processes not only reduced the average height deviations but also compressed the peak-to-valley range, leading to S_z values between 10.246 and 19.023 µm.

A closer comparison of the milling results indicates that increasing feed from 0.5 to 0.8 mm/rev raised S_z from 10.246 to 13.936 μm, a roughly 36% increase, which aligns with the increased feed mark depth and the larger cusp height expected from a coarser toolpath spacing. However, even the rougher milled surface exhibits an S_z value that is only about one-sixth of that of the printed surface, highlighting the remarkable flattening effect of milling.

Grinding introduced another level of surface refinement. The lowest S_z value (12.045 μm) was achieved at 7 m/min, while the higher feed rate (9 m/min) produced a noticeably higher S_z of 19.023 μm. This indicates that increasing the wheel speed may promote instability in the contact zone, potentially due to thermal effects or insufficient coolant efficiency. Such sensitivity of S_z to process parameters emphasizes the need for optimized grinding conditions when targeting ultra-smooth functional surfaces.

Overall, both S_a and S_z parameters follow the expected trend: 3D printing > milling (0.8 mm/rev) > milling (0.5 mm/rev) > grinding (9 m/min) > grinding (7 m/min), demonstrating the progressive improvement of surface finish through successive mechanical removal steps.

3.3 Material distribution parameters

While S_a and S_z describe the amplitude of surface deviations, the skewness and kurtosis provide insight into the shape of the height distribution, revealing whether the surface is dominated by peaks or valleys, and whether it has sharp or flat features. These parameters are crucial for predicting the tribological and functional performance of surfaces, such as bearing capacity, lubrication retention, and contact behaviour.

The as-printed surface shows a slightly positive skewness (S_{sk} = 0.147), suggesting a peak-dominated structure where asperities project above the mean plane. This morphology is typical for additively manufactured parts, in which partially fused particles and ridges create a surface rich in isolated high spots. Such peak-dominated textures can lead to poor contact conformity and rapid wear if used in sliding applications without post-processing.

After milling, the S_{sk} values changed notably. At 0.5 mm/rev, S_{sk} became slightly negative (-0.168), while at 0.8 mm/rev it turned positive again (0.308). This alternating behaviour indicates that feed rate significantly affects the distribution of peaks and valleys. The lower feed produced a surface with shallow valleys and flattened peaks, as cutting marks overlap and the tool removes more irregularities per revolution. In contrast, the higher feed increased the tendency toward periodic ridges, reintroducing a peak-dominated profile. These results underline the strong geometric influence of feed per revolution on the material distribution and texture symmetry in milled surfaces.

Grinding further shifted the skewness toward negative values, with S_{sk} equal to -0.261 at 7 m/min and -0.487 at 9 m/min. This indicates valley-dominated surfaces, where the material removal preferentially smooths the high peaks and leaves a plateau structure with residual micro-depressions. Such surfaces are advantageous for functional applications requiring lubricant retention or improved load distribution, as the valleys can serve as micro-reservoirs. The increasingly negative S_{sk} at higher feed rate suggests more pronounced valley features, which might be associated with localized material pull-out or micro-grooving caused by abrasive interactions.

The kurtosis values (S_{ku}) complement this analysis by indicating the sharpness or flatness of the height distribution. An ideal Gaussian surface has S_{ku} = 3, while values below 3 imply a broader, flatter distribution and values above 3 correspond to sharp, spiky textures. The printed surface shows S_{ku} = 3.090, nearly Gaussian but slightly peaked, consistent with its heterogeneous and irregular asperity structure. The milled surfaces, however, display markedly lower S_{ku} values (1.925 and 1.922), indicating flatter, more uniform height distributions. This suggests that milling effectively homogenized the surface texture, reducing the occurrence of extreme peaks or valleys.

In contrast, grinding at both speeds increased S_{ku} to 2.927 and 3.305, respectively. The first case (7 m/min) is still near-Gaussian, implying a balanced texture with moderate peaks and valleys, while the second (9 m/min) clearly shows a more peaked distribution, possibly due to fine grooves or abrasive scratches that introduce localized height variations. The combined S_{sk} and S_{ku} trends indicate that grinding tends to produce negatively skewed, moderately peaked surfaces, favourable for tribological applications where controlled valleys improve lubricant flow, but sharp asperities are undesirable.

3.4 Comparative evaluation and functional implications

The combined analysis of amplitude and distribution parameters reveals that each surface preparation method produces a distinct topographical signature, directly influencing the potential functional performance. The 3D printed surface, while structurally sound, exhibits the roughest and most irregular morphology, making it unsuitable for precision mechanical contact or sealing applications without post-processing. Its high S_a and S_z values, together with a slightly positive skewness, imply limited bearing area and increased risk of high local contact stresses.

Milling effectively removes these irregularities, producing surfaces with S_a below 2.5 µm and balanced S_{sk} and S_{ku} values, particularly at the lower feed rate. The smoother, more isotropic character achieved at 0.5 mm/rev indicates that controlled feed selection can yield near-Gaussian surfaces with improved uniformity. Such textures are well suited for applications requiring moderate friction and wear resistance, as the absence of pronounced peaks minimizes abrasive interactions.

However, the milled surfaces remain slightly directional due to feed marks, as evident from the anisotropic features seen in Figure 1(b–c).

Grinding offers the finest finish and the most functionally advantageous surface structure. The lower-speed grinding condition (7 m/min) produced the best combination of parameters, with low S_a and S_z, negative S_{sk}, and near-Gaussian S_{ku}. This indicates a plateau-like surface with shallow valleys, ideal for applications requiring both smoothness and lubricant retention. Increasing the feed rate to 9 m/min, although still resulting in a relatively fine surface, introduced slightly higher roughness and stronger negative skewness, possibly linked to thermal or wheel–workpiece interaction effects. The findings thus highlight the need to balance process speed and surface integrity in grinding operations, as excessive speed may compromise topographical uniformity.

3.5 Correlation between roughness parameters and process characteristics

The strong correlation between process kinematics and topographical outcomes can be further discussed in terms of material removal mechanisms. In additive manufacturing, surface roughness is primarily determined by melt pool dynamics and powder or filament deposition accuracy, resulting in large-scale irregularities. Milling, dominated by mechanical shearing and chip formation, produces periodic feed marks that depend on the tool geometry and feed per revolution. Grinding, on the other hand, involves micro-scale cutting by abrasive grains, which generates random, isotropic micro-features.

These mechanisms explain the observed progression of S_a and S_z reductions and the corresponding shifts in S_{sk} and S_{ku}. The printed surface peak-dominated texture (positive S_{sk}) arises from deposited ridges, while the milled surfaces exhibit transitional behavior where tool–material interaction alternates between cutting and ploughing, depending on feed rate. Finally, the ground surfaces achieve valley-dominated distributions (negative S_{sk}) due to abrasive flattening of asperities. The variation in S_{ku} values reinforces this interpretation, as flatter distributions occur when material removal is stable and uniform, while peaked distributions reflect localized irregularities.

3.6 Summary of findings

The comparative results demonstrate that both milling and grinding are effective for post-processing additively manufactured surfaces, yet they differ in their ability to modify surface characteristics. Milling significantly improves roughness by removing macro-scale irregularities, but its texture remains influenced by toolpath geometry and feed rate. Grinding achieves finer finishes and more favorable material distributions, producing plateau-like surfaces beneficial for tribological performance. Quantitatively, the total reduction in S_a from 8.899 µm (printed) to 1.346 µm (ground, 7 m/min) represents an 85% improvement in mean height, while S_z decreased by approximately 85% as well, confirming a consistent leveling of the surface profile. The accompanying evolution of S_{sk} from positive to negative values and S_{ku} toward near-Gaussian levels indicates an overall transition from irregular, peak-rich to uniform, valley-balanced textures.

5. Conclusions

This preliminary investigation examined the surface topography of additively manufactured components and their post-processed counterparts produced by milling and grinding. Quantitative 3D surface measurements revealed substantial improvements in surface quality after subtractive finishing operations. The as-printed surfaces exhibited high roughness amplitudes (S_a = 8.899 µm, S_z = 79.427 µm) and a slightly positive skewness, indicating a peak-dominated morphology typical of layer-based fabrication. Subsequent machining operations significantly reduced surface irregularities, confirming their suitability for enhancing the functional properties of 3D printed parts. Among the post-processing methods, milling with a feed of 0.5 mm/rev and grinding at a feed rate of 7 m/min produced the smoothest and most uniform surfaces. These conditions resulted in the lowest S_a values (1.726 µm and 1.346 µm, respectively) and near-Gaussian height distributions. Grinding generated negatively skewed textures characterized by shallow valleys and plateau structures, which are advantageous for applications involving friction, lubrication, or wear contact. The results demonstrated that controlled finishing parameters allow a transition from rough, peak-dominated printed textures to refined, valley-balanced surfaces suitable for functional testing and potential industrial application. The findings indicate that 3D printed parts, when properly finished, can meet the surface quality requirements necessary for the intended purpose of the ongoing research project. The printed base material provided a stable substrate, and the achieved surface characteristics after milling and grinding suggest that additive–subtractive hybrid manufacturing can effectively combine geometric flexibility with surface precision. In this context, the study confirms the viability of integrating 3D printing as a preparatory step in producing components that require specific surface functionality after finishing.

However, as this was a preliminary study, further investigations are needed to fully validate the process chain and to explore the influence of additional variables such as tool geometry, cutting speed, and material hardness on the resulting surface integrity. Future work will focus on extending the analysis to mechanical and tribological testing, fatigue resistance, and microstructural evaluation. These follow-up studies will establish the relationship between surface topography and functional performance, ensuring that additively manufactured and post-processed components can be reliably applied in engineering practice.

Acknowledgement

The authors gratefully acknowledge the financial support provided by the Priority Budgetary Research Program (KKTP) of the HUN-REN Centre for Energy Research (EK) under the 2025 funding scheme. This support made the experimental work and analyses presented in this study possible.

References: 1. *Leung, Y., Kwok, T., Li, X., Yang, Y., Wang, C. C. L., & Chen, Y.* Challenges and status on design and Computation for emerging additive manufacturing Technologies. Journal of Computing and Information Science in Engineering, 19(2). 2018. https://doi.org/10.1115/1.4041913 **2.** *Zhou, L., Miller, J., Vezza, J., Mayster, M., Raffay, M., Justice, Q., Tamimi, Z. A., Hansotte, G., Sunkara, L. D., & Bernat, J.* Additive Manufacturing: A Comprehensive review. Sensors, 24(9), 2668. 2024. https://doi.org/10.3390/s24092668 **3.** *Nandy, J., Sarangi, H., & Sahoo, S.* A review on Direct Metal Laser sintering: process features and microstructure modeling. Lasers in Manufacturing and Materials Processing, 6(3), 280–316. 2019. https://doi.org/10.1007/s40516-019-00094-y **4.** *Maurya, N. K., Sharma, R., Kumar, N., Kumar, A., Anand, P., Rai, P., & Singh, H.* An overview of investigation of Fatigue, tensile strength and hardness of the components fabricated through direct metal laser sintering (DMLS) process. Materials Today Proceedings, 47, 3979–3984. 2021. https://doi.org/10.1016/j.matpr.2021.04.131 **5.** *Babu, A. S., Jaivignesh, M., Srinivasan, S., & Sugavaneswaran, M.* Design of Functional Gradient Porous Structure and its Fabrication using DMLS Process. Materials Today Proceedings, 24, 1561–1569. 2020. https://doi.org/10.1016/j.matpr.2020.04.476 **6.** *Seharing, A., Azman, A. H., & Abdullah, S.* A review on integration of lightweight gradient lattice structures in additive manufacturing parts. Advances in Mechanical Engineering, 12(6). 2014. https://doi.org/10.1177/1687814020916951 **7.** *Tirnovean, A., Csoregi, N., Borzan, C., & Varga, G.* A REVIEW OF ADDITIVE MANUFACTURING TECHNOLOGIES AND THEIR APPLICATIONS IN THE MEDICAL FIELD. Cutting & Tools in Technological System, 101, 3–16. 2024. https://doi.org/10.20998/2078-7405.2024.101.01 **8.** *Mehdiyev, Z., & Felho, C.* Metal Additive Manufacturing in Automotive Industry: A Review of Applications, Advantages, and Limitations. Materials Science Forum, 1103, 49–62. 2023. https://doi.org/10.4028/p-bg0nin **9.** *Ye, C., Zhang, C., Zhao, J., & Dong, Y.* Effects of post-processing on the surface finish, porosity, residual stresses, and fatigue performance of additive manufactured metals: a review. Journal of Materials Engineering and Performance, 30(9), 6407–6425. 2021. https://doi.org/10.1007/s11665-021-06021-7 **10.** *Patterson, A. E., Messimer, S. L., & Farrington, P. A.* Overhanging features and the SLM/DMLS residual stresses problem: review and future research need. Technologies, 5(2), 15. 2017. https://doi.org/10.3390/technologies5020015 **11.** *Neuberger, H., Hernandez, F., Ruck, S., Arbeiter, F., Bonk, S., Rieth, M., ... & Volker, K. U.* Advances in Additive Manufacturing of fusion materials. Fusion Engineering and Design, 167, 112309. 2021. https://doi.org/10.1016/j.fusengdes.2021.112309 **12.** *Giancarli, L., Chuyanov, V., Abdou, M., Akiba, M., Hong, B., Lässer, R., Pan, C., & Strebkov, Y.* Test blanket modules in ITER: An overview on proposed designs and required DEMO-relevant materials. Journal of Nuclear Materials, 367–370, 1271–1280. 2007. https://doi.org/10.1016/j.jnucmat.2007.03.234 **13.** *Bachmann, C., Ciattaglia, S., Cismondi, F., Eade, T., Federici, G., Fischer, U., Franke, T., Gliss, C., Hernandez, F., Keep, J., Loughlin, M., Maviglia, F., Moro, F., Morris, J., Pereslavtsev, P., Taylor, N., Vizvary, Z., & Wenninger, R.* Overview over DEMO design integration challenges and their impact on component design concepts. Fusion Engineering and Design, 136, 87–95. 2018. https://doi.org/10.1016/j.fusengdes.2017.12.040 **14.** *Day, C., & Murdoch, D.* The ITER vacuum systems. Journal of Physics Conference Series, 114, 012013. 2008. https://doi.org/10.1088/1742-6596/114/1/012013 **15.** *Moon, H., Park, S., Kim, H., & Kim, B. S.* Evaluation of the functional acceptability of the ITER vacuum vessel. Nuclear Fusion, 63(1), 016003. 2022. https://doi.org/10.1088/1741-4326/aca1d0 **16.** *D'Andrea, D.* Additive manufacturing of AISI 316L stainless steel: a review. Metals, 13(8), 1370. 2023. https://doi.org/10.3390/met13081370 **17.** *Zhong, Y., Rännar, L., Liu, L., Koptyug, A., Wikman, S., Olsen, J., Cui, D., & Shen, Z.* Additive manufacturing of

316L stainless steel by electron beam melting for nuclear fusion applications. Journal of Nuclear Materials, 486, 234–245. 2017. https://doi.org/10.1016/j.jnucmat.2016.12.042 **18.** *Gu, D., & Shen, Y.* Processing conditions and microstructural features of porous 316L stainless steel components by DMLS. Applied Surface Science, 255(5), 1880–1887. 2008. https://doi.org/10.1016/j.apsusc.2008.06.118 **19.** *Aziz, U., McAfee, M., Manolakis, I., Timmons, N., & Tormey, D.* A review of optimization of additively manufactured 316/316L stainless steel process parameters, Post-Processing Strategies, and defect mitigation. Materials, 18(12), 2870. 2025. https://doi.org/10.3390/ma18122870 **20.** *Ojo, O. O., & Taban, E.* Post-processing treatments–microstructure–performance interrelationship of metal additive manufactured aerospace alloys: A review. Materials Science and Technology, 39(1), 1–41. 2022. https://doi.org/10.1080/02670836.2022.2130530 **21.** *Kaynak, Y., & Kitay, O.* Porosity, Surface Quality, Microhardness and Microstructure of Selective Laser Melted 316L Stainless Steel Resulting from Finish Machining. Journal of Manufacturing and Materials Processing, 2(2), 36. 2018. https://doi.org/10.3390/jmmp2020036 **22.** *Guzanová, A., Ižaríková, G., Brezinová, J., Živčák, J., Draganovská, D., & Hudák, R.* Influence of Build Orientation, Heat Treatment, and Laser Power on the Hardness of Ti6Al4V Manufactured Using the DMLS Process. Metals, 7(8), 318. 2017. https://doi.org/10.3390/met7080318 **23.** *Melia, M. A., Duran, J. G., Koepke, J. R., Saiz, D. J., Jared, B. H., & Schindelholz, E. J.* How build angle and post-processing impact roughness and corrosion of additively manufactured 316L stainless steel. Npj Materials Degradation, 4(1). 2020. https://doi.org/10.1038/s41529-020-00126-5 **24.** *Diniţă, A., Neacşa, A., Portoacă, A. I., Tănase, M., Ilinca, C. N., & Ramadan, I. N.* Additive Manufacturing Post-Processing Treatments, a Review with Emphasis on Mechanical Characteristics. Materials, 16(13), 4610. 2023. https://doi.org/10.3390/ma16134610 **25.** *Romanescu, P., Omidvarkarjan, D., Ferchow, J., & Meboldt, M.* Evaluation of the Ultra-High Vacuum Suitability of Laser Powder Bed Fusion Manufactured stainless steel 316L. In Springer tracts in additive manufacturing (pp. 407–422). 2023. https://doi.org/10.1007/978-3-031-42983-5_27

Іштван Станкович, Мішкольц, Угорщина, Габор Вереш, Будапешт, Угощина,
Чаба Фельхо, Антал Надь, Мішкольц, Угорщина, Петер Фігецькі-Мелюкуті,
Будапешт, Угорщина

ВПЛИВ ПОСТОБРОБКИ НА ОСНОВІ МЕХАНІЧНОЇ ОБРОБКИ НА ТОПОГРАФІЮ ПОВЕРХНІ НЕРЖАВІЮЧОЇ СТАЛІ DMLS 316L ДЛЯ ЗАСТОСУВАНЬ, ПОВ'ЯЗАНИХ З ПЛАВЛЕННЯМ

Анотація. *У цьому дослідженні досліджується вплив постобробки на основі механічної обробки на топографію поверхні нержавіючої сталі Direct Laser Sintered (DMLS) 316L, призначеної для застосувань, пов'язаних із термоядерним синтезом. Кубічні зразки (30 × 30 × 30 мм) виготовлялися методом адитивного виробництва і в подальшому допрацьовувалися торцевим фрезеруванням і шліфуванням поверхні при двох параметричних налаштуваннях кожен. Рельєф поверхні був охарактеризований за допомогою оптичної системи AltiSurf 520 відповідно до стандарта ISO 25178. Надрукована поверхня продемонструвала високу шорсткість (Sa = 8,899 мкм, Sz = 79,427 мкм), тоді як усі поверхні, що пройшли постобробку, показали значне покращення. Найнижча шорсткість (Sa = 1,346 мкм) була отримана після шліфування при швидкості подачі 7 м/хв. Аналіз перекосу та куртозу показав, що механічна обробка перетворила поверхню, в більш однорідну, майже гаусову текстуру. Результати підтверджують, що контрольовані операції фрезерування та шліфування можуть ефективно покращити цілісність поверхні компонентів DMLS 316L. Ці результати демонструють потенціал гібридного адитивно-субтрактивного виробництва для отримання поверхонь, придатних для вакуума та функціональних вимог застосування термоядерних технологій. У цьому контексті дослідження підтверджує* *життєздатність інтеграції 3D-друку як підготовчого етапу у виробництві компонентів, що вимагають специфічної функціональності поверхні після фінішної обробки. Однак, оскільки це було попереднє дослідження, необхідні подальші дослідження, щоб повністю перевірити технологічний ланцюжок і вивчити вплив додаткових змінних, таких як геометрія інструменту, швидкість різання та твердість матеріалу, на результуючу цілісність поверхні. Майбутня робота буде зосереджена на поширенні аналізу на механічні та трибологічні випробування, стійкість до втоми та оцінку мікроструктури. Ці подальші дослідження встановлять взаємозв'язок між топографією поверхні та функціональними характеристиками, гарантуючи, що компоненти, виготовлені адитивно та після обробки, можуть бути надійно застосовані в інженерній практиці.*

Ключові слова: *адитивне виробництво; нержавіюча сталь DMLS 316L; рельєф поверхні; постобробка; застосування технології термоядерного синтезу.*

UDC 621.91.01 **doi: 10.20998/2078-7405.2025.103.05**

FORM ACCURACY AND CUTTING FORCES IN TURNING OF X5CRNI18-10 SHAFTS: ASSESSMENT OF FEED FORCE VARIATION AND ITS RELATION TO FORM DEVIATIONS

Wafae **El Majdoub** [0009-0004-5926-661X], István **Sztankovics** [0000-0002-1147-7475]

University of Miskolc, 3515 Miskolc-Egyetemváros, Hungary
istvan.sztankovics@uni-miskolc.hu

Received: 10 November 2025/ Revised: 19 November 2025/ Accepted: 29 November 2025 / Published: 15 December 2025

Abstract. *The study presented in this paper aims to provide insight into how cutting parameters, including cutting speed, feed, and depth of cut, influence feed force and form deviations during the X5CRNI18-10 shafts machining. Many experiments were carried out at two depths of cut levels (0.5mm and 1mm) to investigate the effects of cutting speed and feed on feed force, roundness, and waviness. The findings showed that increasing the depth of cut has the strongest influence on cutting force and form deviation. In parallel, higher feed affected the roundness and waviness, leading to a reduction in the surface quality due to the tool deflection and vibrations. Cutting speed had a small impact; however, it is still crucial to select cutting parameters carefully to secure a proper balance between dimensional accuracy, surface quality, and machining efficiency.*

Keywords: *cutting parameters; roundness; waviness; form deviations; turning.*

1. Introduction

The turning of austenitic stainless steel X5CrNi18-10 (equivalent to AISI 304) remains a major challenge for the mechanical engineering industry due to its poor machinability, caused by its high ductility, tendency to work harden, and friction between chips and tools. These issues result in high cutting forces, vibrations, and a reduction in the dimensional accuracy of the workpiece. Several studies reveal that variations in feed force can be directly correlated with geometric deviations, particularly circularity and cylindricity [1-4].

Cutting forces are generally broken down into three components: tangential (F_c), radial (F_r) and axial (F_f). Devices such as Kistler dynamometers can be used to measure these components with high precision. Recent investigations have indicated that the feed force varies significantly depending on the feed conditions, tool geometry and rigidity of the mounting, directly influencing shape accuracy [5,6]. Cutting speed (v_c), feed rate (f), and depth of cut (a) play a key role in influencing forces. An increase in feed rate generally causes a linear increase in feed force and a worsening of surface quality. However, a higher cutting speed tends to reduce the average force due to localized heat and reduced friction [7-9].

Varying feed force causes dynamic deflections of the tool and workpiece, resulting in circularity and cylindricity errors. Studies have shown that periodic oscillation of the axial force can generate measurable surface waviness even when the amplitude of variation remains low. FEM models and frequency analyses confirm the direct correlation between feed force instability and geometric deterioration [10,11]. The geometry of the tool, particularly the clearance, cutting and direction angles, significantly influences the feed component. The use of micro-grooved inserts or coated tools (TiAlN, CrN) reduces cutting forces and improves surface smoothness [12-14]. In addition, the rigidity of the tool-workpiece system is crucial for limiting deformation and vibration [15,16].

Force reduction strategies include the use of minimum quantity lubrication (MQL), nanofluids, and multi-objective optimization of cutting parameters tested to improve the quality of machined surfaces, which represents a major challenge in the manufacturing industry. Experimental approaches coupled with FEM simulation enable accurate prediction of forces and final shape [17,18]. Frequency analysis of force and vibration signals also provides reliable indicators for anticipating geometric errors [19]. Research confirms that variations in feed force are a key factor in generating shape errors when turning X5CrNi18-10 steel. A comprehensive understanding of the mechanical and thermal mechanisms involved, combined with real-time force sensors and predictive models, paves the way for adaptive control of machining accuracy [20,21].

This study was conducted to examine the impact of varying cutting parameters on cutting forces and shape error parameters, specifically, roundness and waviness, during the turning operation of X5CrNi18-10 stainless steel shafts. The investigation will focus on feed force as a key parameter that directly affects the surface quality. It represents the resistance subjected by the tool in the feed direction and is influenced by cutting speed, depth of cut, and feed. Evaluating how cutting parameters affect feed force and shape deviation can provide insight into the surface formation and assist in predicting surface imperfections. As well as these analyses can be used to establish the relations between the cutting parameters, force measured, and surface deviations.

2. Experimental conditions and methods

In the aim of investigating the effects of cutting parameters in introducing cutting forces and shape error during the turning operation, theoretical calculations and experimental analysis were performed. For successful evaluation, experiments were carried out using chromium-nickel austenitic stainless-steel (X5CrNi18.10) specimens. The material employed in this study is known for its excellent corrosion resistance, making it suitable for machining applications. During the turning process, the cutting speed was varied between 200 and 300 mm/min, and the feed was varied at two levels, 0.08 and 0.24 mm/rev, while adjusting the depth of cut from 0.5 mm to 1mm.

Five workpieces of 50 mm were used; each workpiece was divided into five equal surfaces of 30 mm separated by grooves. These surfaces were utilized to measure cutting forces and shape deviations. However, to conduct this study, only eight setups were selected and are mentioned in Table 1.

The tests were performed in wet conditions (5% emulsion of “CIKS HKF 420” coolant oil) using a DDJNL2525M15 tool holder with a DNMG150604-MF1 CP500 carbide/ceramic insert, which is a suitable option for hard cuts. Then the tool was fixed on the HAAS ST-20Y-EU lathe. Moreover, a dynamometer and three amplifiers were mounted on the machine to capture cutting force in three directions, such as cutting force, feed force, and passive force. To calculate the force main and standard deviation, the obtained data were processed using Python codes. Furthermore, the Talyrond 365 precision measuring device was adjusted to standard procedures and methodologies from previous research to measure form deviations. However, the paper will focus on studying the influence of cutting variables only on feed force, roundness, and waviness.

Table 1 – Summary of the applied setups in the experiments

Setup	1	2	3	4	5	6	7	8
v_c [m/min]	200	300	200	300	200	300	200	300
f [mm]	0.08	0.08	0.24	0.24	0.08	0.08	0.24	0.24
a [mm]	0.5	0.5	0.5	0.5	1.0	1.0	1.0	1.0

The evaluated parameters were the following:

- F_f – Feed Directional Force [N]
- σ_f – Standard deviation of the Feed Directional Force [N]
- *RONp* –Maximum radial deviation of a peak from the reference circle. [μm]
- *RONv* – Maximum radial deviation of a valley from the reference circle. [μm]
- *SLOPEm* – Maximum value of the changing of the roundness profile [μm]
- W_a – Average Height of the Waviness Profile [μm]

To analyse the variables under evaluation, Equation 1 was formulated according to the Design of Experiments (DoE) approach. The polynomial equation presents the main parameters such as feed rate (*f*), cutting speed (v_c), and depth of cut (*a*), and their correlation. Moreover, to show how these variables affect the cutting force and form deviations, the constant coefficients (k_i) indicate factors with the major impact. This study aims to enhance and optimize the machining conditions with a focus on improving dimensional accuracy and surface quality.

$$y(v_c, f, a) = \mathrm{k}_0 + \mathrm{k}_1 v_c + \mathrm{k}_2 f + \mathrm{k}_3 a + \mathrm{k}_{12} v_c f + \mathrm{k}_{13} v_c a + \mathrm{k}_{23} fa + \mathrm{k}_{123} v_c fa \qquad (1)$$

3. Experimental results

Based on the previous section, evaluations were conducted to investigate the cutting parameters influence on feed force and shape deviations. The calculated equations 2,3,4,5,6, and 7 according to the formula in equation 1 represent the interaction between cutting variables such as feed, depth of cut, and cutting speed with feed force, roundness components, and waviness. In addition, tables 2,3,4,5,6, and 7 indicate the corresponding results of the feed force main, standard deviation, roundness elements (*RONp*, *RONv*, and *SLOPE*), and waviness.

The feed directional force within the investigated region is expressed by Equation 2:

$$F_f(v_c, f, a) = ((8.68\mathrm{a} - 7.538)\mathrm{f} - 0.923\mathrm{a} + 1.02)\mathrm{v_c} + (-872.\mathrm{a} + 404.1)\mathrm{f} + 123.8\mathrm{a} - 28.14 \qquad (2)$$

Its variation in standard deviation can be described using Equation 3:

$$\sigma_f(v_c, f, a) = ((-0.473\mathrm{a} + 0.12)\mathrm{f} + 0.013\mathrm{a} + 0.045)\mathrm{v_c} + (205.2\mathrm{a} - 80.85)\mathrm{f} - 8.98\mathrm{a} - 4.182 \qquad (3)$$

Roundness Peak error is determined according to Equation 4:

$$RONp(v_c, f, a) = ((0.15\mathrm{a} - 0.055)\mathrm{f} - 0.015\mathrm{a} + 0.0061)\mathrm{v_c} + (-34.1\mathrm{a} + 11.3)\mathrm{f} + 3.5\mathrm{a} - 0.39 \qquad (4)$$

Roundess Valley error is evaluated using Equation 5.

$$RONv(v_c, f, a) = ((-0.004\mathrm{a} + 0.049)\mathrm{f} + 0.004\mathrm{a} - 0.005)\mathrm{v_c} + (0.87\mathrm{a} - 11.1)\mathrm{f} - 0.9\mathrm{a} + 2.04 \qquad (5)$$

The mathematical expression for slope error is presented in Equation 6:

$$SLOPEm(v_c, f, a) = 0.0001((-12.5\mathrm{a} + 50.6)\mathrm{f} + 0.2\mathrm{a} - 2)\mathrm{v_c} + (0.4\mathrm{a} - 1.2)\mathrm{f} - 0.01\mathrm{a} + 0.1 \qquad (6)$$

Finally, the average waviness is formulated in Equation 7:

$$W_a(v_c, f, a) = ((-0.00025\mathrm{a} + 0.004)\mathrm{f} + 0.0006\mathrm{a} - 0.0008)\mathrm{v_c} + (0.8\mathrm{a} - 0.9)\mathrm{f} - 0.2\mathrm{a} + 0.23 \qquad (7)$$

Table 2 – Measurement results of the Feed Directional Force

F_f [N]	Setup							
No.	1	2	3	4	5	6	7	8

Result	91.7	122.0	-15.6	-36.4	95.9	114.8	57.9	95.2

Table 3 – Measurement results of the Standard Deviation of the Feed Directional Force

σ_f [N]	Setup							
No.	1	2	3	4	5	6	7	8
Result	1.69	6.00	1.53	4.02	2.95	6.03	11.63	9.10

Table 4 – Measurement results of the Roundness Peak

RON_p [µm]	Setup							
No.	1	2	3	4	5	6	7	8
1	0.90	0.81	0.78	1.70	1.01	1.09	0.64	3.86
2	0.57	0.87	0.72	1.04	0.99	0.90	0.64	1.25
3	1.30	1.11	0.74	0.66	0.96	0.52	0.57	1.20
Avg.	0.92	0.93	0.75	1.13	0.99	0.84	0.62	2.10

Table 5 – Measurement results of the Roundness Valley

RON_v [µm]	Setup							
No.	1	2	3	4	5	6	7	8
1	0.72	1.16	0.83	1.87	0.94	1.28	0.90	2.27
2	0.71	0.87	0.67	1.48	0.78	1.49	0.67	1.51
3	1.29	0.97	0.68	1.39	0.79	0.55	0.45	1.24
Avg.	0.91	1.00	0.73	1.58	0.84	1.11	0.67	1.67

Table 6 – Measurement results of the Maximum Slope

SLOPEm [µm]	Setup							
No.	1	2	3	4	5	6	7	8
1	0.060	0.088	0.060	0.312	0.064	0.088	0.126	0.252
2	0.055	0.088	0.048	0.058	0.078	0.119	0.044	0.109
3	0.076	0.081	0.053	0.070	0.062	0.050	0.041	0.086
Avg.	0.064	0.086	0.054	0.147	0.068	0.086	0.070	0.149

Table 7 – Measurement results of the Average Height of the Waviness profile

W_z [µm]	Setup							
No.	1	2	3	4	5	6	7	8
1	0.039	0.016	0.109	0.098	0.009	0.019	0.137	0.237
2	0.040	0.018	0.081	0.137	0.010	0.020	0.118	0.194
3	0.035	0.022	0.085	0.175	0.007	0.016	0.122	0.160
Avg.	0.038	0.019	0.092	0.137	0.009	0.018	0.126	0.197

4. Discussion

By using the data in the tables mentioned in the previous section, surface plots were generated for each studied parameter. These plots indicate how feed force components and form deviation variables vary while changing cutting parameters.

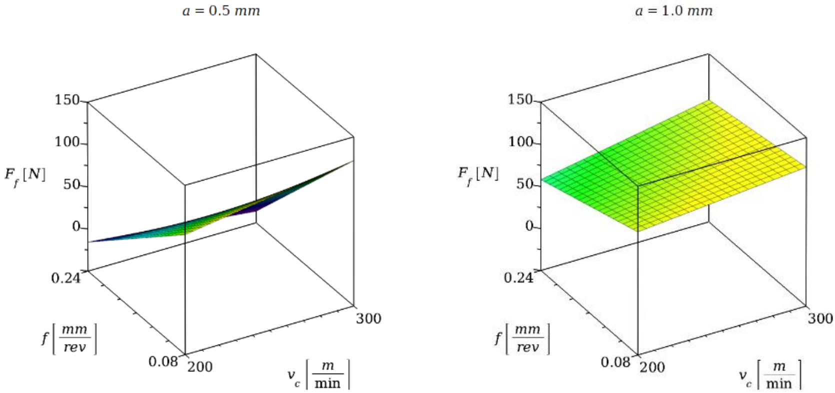

Figure 1 – Variation of the Feed Directional Force in the studied range

Figure 1 shows the changes in the feed force while varying the cutting speed and feed at two levels of depth of cut. At a depth of cut of 0.5 mm, the feed directional force increases progressively with increasing the cutting speed from 200 m/min to 300 m/min, while it decreases noticeably when the feed rate goes from 0.08 mm/rev to 0.24 mm/rev. The analysis suggests that the resistance in the feed direction can be reduced by adjusting the feed rate value, which can enhance the shape removal and minimize the friction effects. However, the rise in the feed force due to the cutting speed can be explained by the interaction between the tool and the workpiece, which can cause thermal effects.

At a cutting depth of 1.0 mm, in the process of increasing the cutting force, the feed force seems to increase slightly due to the introduced friction and temperature at the cutting zone. In parallel, the variation of the feed rate from 0.08 mm/rev to 0.24 mm/rev showed a Modest increase in the feed directional force. In conclusion, the findings suggest that at a smaller depth of cut and higher feed rates value the force remains small. Furthermore, the force range in the 1mm depth of cut is greater compared to the 0.5 mm depth of cut, indicating that the use of more material while machining requires more cutting force, which highlights the need for controlling the cutting parameters to avoid high tool stress.

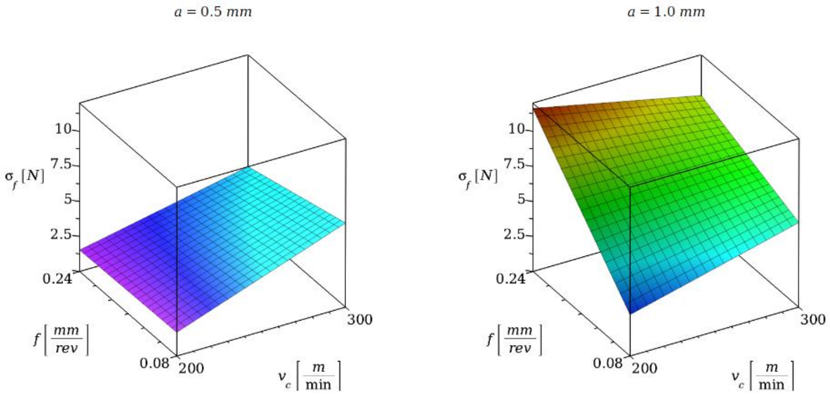

Figure 2 – Variation of the Standard deviation of the Feed Force in the studied range

Figure 2 represents the standard deviation of the feed force (σ_f) as a function of cutting parameters. The plot of 0.5mm depth of cut shows that the standard deviation increases slightly with varying cutting speed from 200 mm/min to 300 mm/min, while changing the feed rate seems to have no effect. However, the results demonstrate that the cutting process was smooth, and less force variation was detected. Compared to the first analysis, the standard deviation at 1.0 mm seems to be more sensitive to both cutting parameters. σ_f rises while increasing the feed, but it is more noticeable at lower speed and higher feed (200 mm/min-0.24 mm/rev). The findings can be clarified by the fact that removing more material can make the process less stable and lead to strong force variation; As a result, the control of cutting speed will be essential to optimize the machining conditions.

The effects of cutting parameters on the roundness peak error (RON_p) were presented in Figure 3. At a small depth of cut of 0.5 mm, the RON_p seems to be stable or to have minor changes, especially at higher cutting speed and higher feed. These results show that the produced surface has a uniform shape and less deformation, which means the tool performed the cutting process under stable conditions.

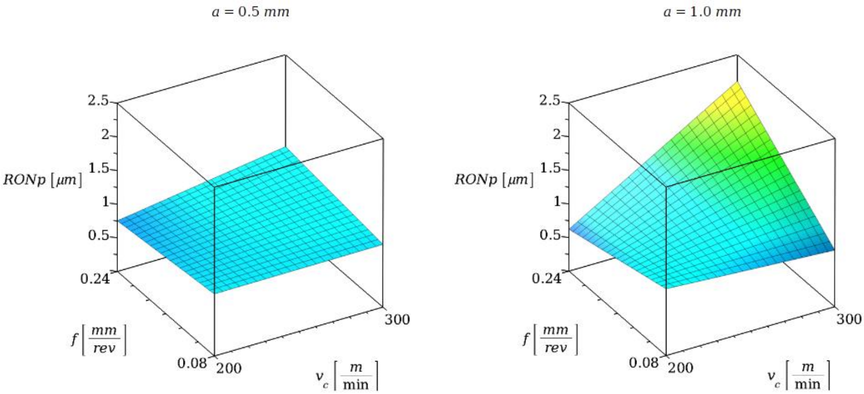

Figure 3 – Variation of the Roundness Peak error in the studied range

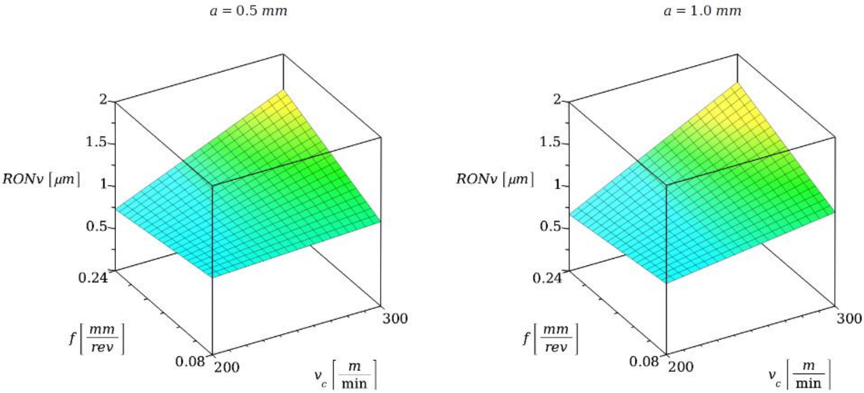

Figure 4 – Variation of the Roundness Valley error in the studied range

Furthermore, the roundness peak error appears to grow with increasing the depth of cut to 1mm, and the effects of cutting speed and feed are more visible. The plot reveals that higher values of cutting variables lead to deviation from the ideal round shape, which can cause less accuracy of the machined part. Therefore, to reduce the roundness errors and enhance the accuracy, it is necessary to keep balanced feed and cutting speed values.

Another parameter of roundness was analysed and presented in Figure 4. At both depths of cut, the Roundness Valley error (RON_v) tends to increase with increasing the cutting speed and the feed, which means that both cutting parameters affect the accuracy of the machined surface. The deviations from the original circle are more pronounced at higher speed (300 mm/min) and higher feed (0.24 mm/rev), which means more mechanical load and heat effects can produce deformation in the machined part. However, the depth of cut seems to have a minor influence on RON_v. As a result, the proper selection of cutting parameters can improve the process conditions and prevent vibrations and deformations to achieve better roundness and dimensional accuracy.

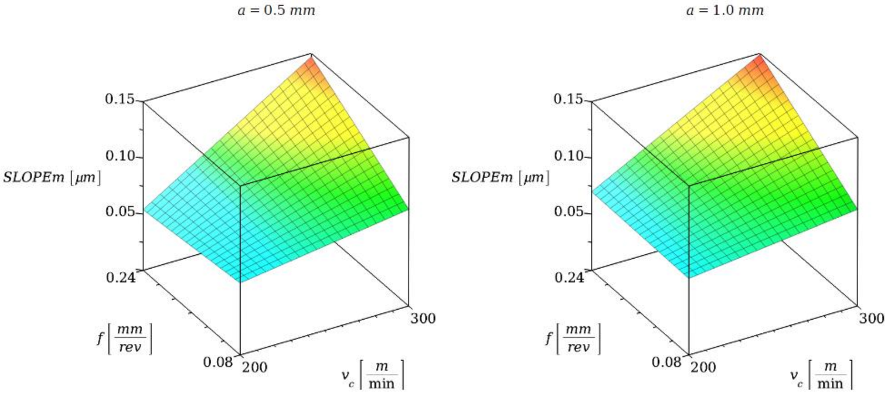

Figure 5 – Variation of the Slope error in the studied range

Figure 5 studies the changes in $SLOPE_m$ as a function of cutting speed, feed, and depth of cut. The plots look similar in both depths of cut and have the same behaviours while changing the speed and the feed. Indicating that the depth of cut may not have a direct relation with the slope. Moreover, $SLOPE_m$ grows significantly with increasing the cutting speed from 200 m/min to 300 m/min and the feed from 0.08 mm/rev to 0.24 mm/rev. But the errors are more visible at higher values of cutting speed and feed. The analysis of roundness components reveals that it is critical to adjust the cutting parameters, especially cutting speed and feed, due to their dominant effects in developing machining errors. That can be illustrated by the heat and tool vibration generated by the interaction between the tool and the workpiece in the cutting zone, which influence the machined part accuracy and surface integrity.

Finally, Figure 6 examines the effect of cutting parameters on surface waviness (W_a). At a depth of cut of 0.5 mm, increasing the cutting speed at a low feed (0.08 mm/rev) slightly reduces the waviness, while at a higher feed rate (0.24 mm/rev), the waviness tends to increase noticeably. In general, an increase in feed values has a direct relationship with higher waviness values.

The second plot represents the waviness variation at 1mm depth of cut when W_a seems to be affected by both parameters, and the changes are more pronounced at higher feed and cutting speed. The findings showed that to reduce surface waviness, it is essential to select optimal cutting parameters.

As a conclusion, all the parameters studied appear to have a direct relation with cutting parameters; these outcomes lead to the development of new methodologies in order to enhance accuracy and efficiency.

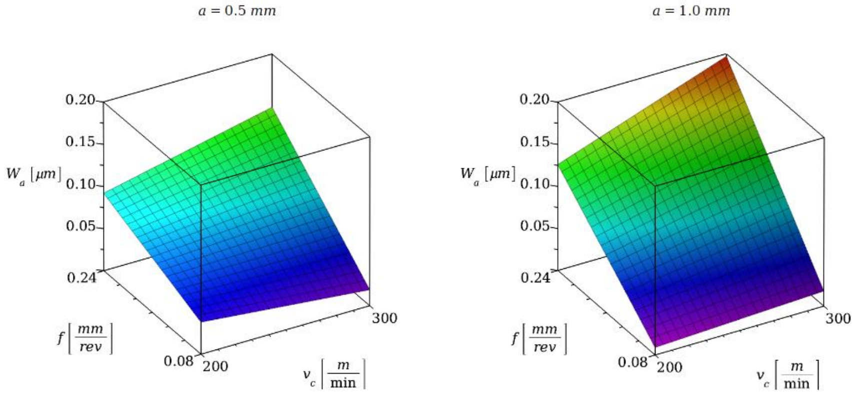

Figure 6 – Variation of the Average Height of the Waviness profile in the studied range

5. Conclusions

This paper discussed the relationship between cutting parameters, feed force, and form deviations, including roundness and waviness, during the turning operation of X5CrNi18-10 stainless steel shafts. The experimental tests were carried out under controlled conditions employing the HAAS ST-20Y-EU turning machine, dynamometer, and shape error measurement instruments to collect the form and shape deviation data.

The results indicated that the depth of cut is the most influential parameter on cutting forces and form deviations. Increasing the depth of cut from 0.5 to 1.0 mm significantly increased the cutting forces and form errors. At the same time, feed rate was strongly correlated with roundness and waviness errors, as higher feed rates increased these errors due to increased tool deflection and vibration. The cutting speed was less influential but still played a role in surface integrity due to thermal and dynamic effects.

In general, this study emphasizes the need for effective control and optimization of the cutting parameters-feed rate and cutting speed-aiming to maintain stability of the process and accuracy at the surface. The approach undertaken in this work, combining experimentation with analysis, thus helps in identifying the role of variables used in the process with respect to dimensional errors and hence establishes some guidelines for obtaining higher precision and better surface quality during the turning of austenitic stainless steel.

References: 1. *Kundrák, J., Karpuschewski, B., Gyani, K., & Bana, V.* Accuracy of hard turning. Journal of Materials Processing Technology, 202(1–3), 328–338. 2007. https://doi.org/10.1016/j.jmatprotec.2007.09.056 **2**. *Agarwal, A., & Desai, K.* Predictive framework for cutting force induced cylindricity error estimation in end milling of thin-walled components. Precision Engineering, 66, 209–219. 2020. https://doi.org/10.1016/j.precisioneng.2020.07.007 **3**. *El Majdoub, W., Daud, M. H., & Sztankovics, I.* Form accuracy and cutting forces in turning of X5CrNi18-10 shafts: Investigating the influence of thrust force on roundness deviation under low-feed machining conditions. Journal of Production Engineering, 28(1), 26–33. 2025. https://doi.org/10.24867/jpe-2025-01-026 **4**. *Sztankovics, I., & El Majdoub, W.* Preliminary study on the cutting force and shape error in turning of X5CrNi18-10 shafts with small feed. Journal of Production Engineering, 27(2), 21–28. 2024. https://doi.org/10.24867/jpe-2024-02-021 **5**. *Dai, Y., Jiang, J., Zhang, G., & Luo, T.* Forced-based tool deviation induced form error identification in single-point diamond turning of optical spherical surfaces. Precision Engineering, 72, 83–94. 2021. https://doi.org/10.1016/j.precisioneng.2021.04.001 **6**. *Rao, C., Rao, D. N., & Srihari, P.* Influence of cutting parameters on cutting force and surface finish in turning operation. Procedia Engineering, 64, 1405–1415. 2013. https://doi.org/10.1016/j.proeng.2013.09.222 **7**. *Laghari, R. A., & Li, J.* Modeling and optimization of cutting forces and effect of turning parameters on SiCp/Al 45% vs SiCp/Al 50% metal matrix composites: a comparative study. SN Applied Sciences, 3(7). 2021. https://doi.org/10.1007/s42452-021-04689-z **8**. *Fu, M., Xiao, G., Chen, H., Zhang, J., Yi, M., Chen, Z., & Xu, C.* Investigation of Surface Integrity of 304 Stainless Steel in Turning Process with Nanofluid Minimum-Quantity Lubrication Using h-BN Nanoparticles. Metals, 14(5), 583. 2024. https://doi.org/10.3390/met14050583 **9**. *Liu, Z., & Wu, J.* Study on Cutting Performance of Micro Groove Tool in Turning AISI 304 and Surface Quality of the Workpiece. Coatings, 12(9), 1326. 2022. https://doi.org/10.3390/coatings12091326 **10**. *Litak, G., Polyakov, Y. S., Timashev, S. F., & Rusinek, R.* Dynamics of stainless steel turning: Analysis by flicker-noise spectroscopy. Physica a Statistical Mechanics and Its Applications, 392(23), 6052–6063. 2013. https://doi.org/10.1016/j.physa.2013.07.079 **11**. *Binali, R., Demirpolat, H., Kuntoğlu, M., & Salur, E.* Different Aspects of Machinability in Turning of AISI 304 Stainless Steel: A Sustainable Approach with MQL Technology. Metals, 13(6), 1088. 2023. https://doi.org/10.3390/met13061088 **12**. *Kónya, G., Takács, J., Miskolczi, I., & Kovács, Z. F.* Investigation of the effects of machining parameters on cutting conditions during orthogonal turning of austenite stainless steel. Production Engineering Archives, 30(1), 86–93. 2024. https://doi.org/10.30657/pea.2024.30.8 **13**. *Zenkin, M., Ivanko, A., & Chernysh, M.* Influence of cutting tool vibrations on the surface quality of cut sheet materials and methods for their minimization. Innovative Technologies and Scientific Solutions for Industries, 2(32), 188–198. 2025. https://doi.org/10.30837/2522-9818.2025.2.188 **14**. *A, N. P., Kumaragurubaran, B., & Kumar, T. S.* Optimization of cutting parameters in CNC turning of AISI 304 and AISI 316 stainless steel. International Journal of Trend in Scientific Research and Development, Volume-2(Issue-4), 955–959. 2018. https://doi.org/10.31142/ijtsrd14185 **15**. *Hanief, M., Wani, M., & Charoo.* Modeling and prediction of cutting forces during the turning of red brass (C23000) using ANN and regression analysis. Engineering Science and Technology an International Journal, 20(3), 1220–1226. 2016. https://doi.org/10.1016/j.jestch.2016.10.019 **16**. *Felhő, C., & Namboodri, T.* Statistical analysis of cutting force and vibration in turning X5CRNI18-10 steel. Applied Sciences, 15(1), 54. 2024. https://doi.org/10.3390/app15010054 **17**. *Wojciechowski, S., Suszyński, M., Talar, R., Černohlávek, V., & Štěrba, J.* Cutting Force—Vibration Interactions in precise—and micromilling Processes: A Critical Review on Prediction Methods. Materials, 18(15), 3539. 2025. https://doi.org/10.3390/ma18153539 **18**. *Trif, A.* Studies on the Cutting Forces in Case of Stainless Steel Turning Operation. Academic Journal of Manufacturing Engineering, 16(2), 143-151. 2018. **19**. *Gutakovskis, V., Gerins, E., Naginevicius, V.,* *Gudakovskis, V., Styps, E., & Sertvytis, R.* Adaptive control for the metal cutting process. International Journal of Engineering Research in Africa, 51, 1–7. 2020. https://doi.org/10.4028/www.scientific.net/jera.51.1 **20**. *Weng, J., Zhuang, K., Xu, D., M'Saoubi, R., & Zhou, J.* A comprehensive study on cutting mechanisms and surface integrity of AISI 304 when turning a curved surface. Materials and Manufacturing Processes, 36(11), 1285–1298. 2021. https://doi.org/10.1080/10426914.2021.1906893 **21**. *Gutakovskis, V., Gerins, E., Naginevicius, V., Gudakovskis, V., Styps, E., & Sertvytis, R.* Adaptive control for the metal cutting process. International Journal of Engineering Research in Africa, 51, 1–7. 2020. https://doi.org/10.4028/www.scientific.net/jera.51.1

Вафає Ель Маджduб, Іштван Станкович, Мішкольц, Угорщина

ТОЧНІСТЬ ФОРМИ І СИЛИ РІЗАННЯ ПРИ ТОКАРНІЙ ОБРОБЦІ ВАЛІВ X5X5XH18-10: ОЦІНКА ЗМІНИ ВЕЛИЧИНИ ПОДАЧІ І ЇЇ ЗВ'ЯЗОК З ВІДХИЛЕННЯМИ ФОРМИ

Анотація. *Токарна обробка аустенітної нержавіючої сталі X5CrNi18-10 (еквівалент AISI 304) залишається серйозною проблемою для машинобудівної промисловості через її погану оброблюваність, спричинену високою пластичністю, схильністю до загартування та тертям між стружкою та інструментами. Дослідження, представлене в цій статті, має на меті дати уявлення про те, як параметри різання, включаючи швидкість різання, подачу та глибину різання, впливають на силу подачі та відхилення форми під час обробки валів зі сталі X5CRNI18-10. Було проведено багато експериментів на двох глибинах різання (0,5 мм і 1 мм) для вивчення впливу швидкості різання та подачі на силу подачі, округлість та хвилястість. Експериментальні випробування проводилися в контрольованих умовах з використанням токарного верстата HAAS ST-20Y-EU, динамометра та приладів для вимірювання похибки форми для збору даних про відхилення форми. Результати показали, що глибина різання є найбільш впливовим параметром на зусилля різання і відхилення форми. Збільшення глибини різу з 0,5 до 1,0 мм значно збільшувало зусилля різання і похибки форми. У той же час швидкість подачі сильно корелювала з помилками округлості та хвилястості, оскільки вища швидкість подачі збільшувала ці похибки через збільшення прогину інструменту та вібрації. Швидкість різання була менш впливовою, але все одно відігравала роль у цілісності поверхні через термічний та динамічний вплив. В цілому в даному дослідженні наголошується на необхідності ефективного контролю та оптимізації параметрів різання - швидкості подачі та швидкості різання - уточнення для збереження стабільності процесу та точності на поверхні. Підхід, застосований у цій роботі, що поєднує експерименти з аналізом, таким чином допомагає виявити роль змінних, що використовуються в процесі, щодо похибок розмірів і, отже, встановлює деякі рекомендації для отримання вищої точності та кращої якості поверхні під час токарної обробки аустенітної нержавіючої сталі.*

Ключові слова: *параметри різу; округлість; хвилястість; відхилення форми; токарна обробка.*

ISSN 2078-7405 Cutting & Tools in Technological System, 2025, Edition 103

UDC 519.711, 621.923.6 **doi: 10.20998/2078-7405.2025.103.06**

MODELING THE IMPACT OF NONLINEAR OSCILLATIONS ON THE QUALITY OF THE WORKING SURFACE OF PARTS IN FINISHING OPERATIONS

Anatoliy **Usov** [0000-0002-3965-7611], Maksym **Kunitsyn** [0000-0003-1764-8922], Yurii **Zaichyk** [0000-0002-8577-1095], Yuliia **Sikirash** [0000-0003-0853-582X]

National University "Odessa Polytechnic", Odessa, Ukraine
m.v.kunitsyn@op.edu.ua

Received: 11 November 2025/ Revised: 18 November 2025/ Accepted: 28 November 2025 / Published: 15 December 2025

Abstract. *To establish analytical conditions for detecting hereditary defects in ferroceramic and ferromagnetic parts and to define machining parameters that prevent crack formation. Magnetic induction scattering is modelled to estimate defect geometry and depth; thermomechanical processes during grinding are analysed using the "weakest link" hypothesis and criteria based on temperature, heat flux, forces, and stress intensity. Obtained expressions describe magnetic field perturbation and allow evaluating defect size, while derived conditions prevent their growth into main cracks. A unified analytical framework combines magnetic defect detection with crack-resistance modelling. The results support selecting grinding modes and tool characteristics for defect-free finishing of materials prone to cracking.*

Keywords: *hereditary defect; crack formation; finishing operation; ferromagnetic modeling; analytical dependencies.*

1. Introduction

For high-quality processing of ferromagnetic materials in finishing operations, it is necessary to have information about the presence of hereditary defects in the surface layer, the size and depth of which affect crack formation on the processed surfaces under the influence of thermomechanical phenomena accompanying these operations. Magnetic methods of quality control of ferromagnetic materials and parts made of them are among the most common types of flaw detection [1]. They are based on the registration of a magnetic field on the surface of a part because of the presence of a defect. In this case, Hall sensors, magnetic diodes, or magnetic tape can be used as field indicators, as an intermediate information carrier. After being recorded on magnetic tape, the information is read using induction heads. Magnetic control methods require mandatory magnetization of parts and search for insignificant magnetic fields on their surfaces, which are called defect scattering fields [2]. These methods are used to check the blades, shafts, gear wheels, and other critical parts of the machine.

This paper considers the mathematical formulation of the problem of detecting defects in ferromagnetic parts during their magnetization. Mathematical expressions are obtained to estimate the geometric shape and depth of a defect beneath the surface of a part based on the results of measuring the distribution of magnetic induction on its surface.

When ferromagnetic parts are magnetized with alternating current, a defect of non-magnetic material located deep inside the part distorts the magnetic field pattern and partially displaces it above the surface of the part. The following task was set: based on the results of measuring the distribution of the magnetic field induction on the surface of the part and specifying the magnetic field induction value for magnetization, calculate the depth of placement and give an estimate of the shape of the defect under the surface of the part.

2. Analysis of sources and problem description

The critical challenge in manufacturing high-quality components from ferroceramic materials lies in managing defects, particularly those inherited from previous processing stages (hereditary defects), which can develop into critical cracks during final finishing operations. Addressing this requires a unified approach encompassing both reliable non-destructive testing (NDT) and robust thermomechanical process control.

Magnetic Nondestructive Testing (NDT) methods are widely acknowledged for their role in quality control, especially for detecting subsurface defects in ferromagnetic materials [3]. Recent advancements, such as phase-extraction-based Magnetic Flux Leakage (MFL), have significantly improved the subsurface detection depth, with reported limits up to 12 mm in steel plates [3]. Techniques utilizing pulse magnetization or chirp-waveforms further enhance sensitivity and reliability for detection [4].

However, significant limitations persist, particularly concerning the reliable detection and quantification of small, deep, or hereditary defects. Most magnetic techniques are inherently constrained by the skin effect and signal attenuation, which restrict reliable detection to moderate depths [3], [5]. Crucially, many existing NDT methods, even advanced hybrid systems, struggle with the accurate quantification of a defect’s geometric size and depth [6], [7]. The over-reliance on complex signal processing and the variability introduced by material properties or environmental interference often diminish the intuitiveness and repeatability of quantitative results [6]. This gap highlights the necessity for a rigorous mathematical formulation that can directly link the measured distribution of the magnetic field to the precise geometric shape and depth of an internal hereditary defect.

In brittle materials like ceramics and ferroceramics, failure during processing is predominantly modeled through the weakest link hypothesis [8], [9]. This statistical framework posits that material strength is governed by the single most critical flaw present in the loaded volume, often formalized through Weibull statistics to predict failure probability based on the distribution of flaws [10], [11], [12]. Modern fracture research continues to rely on this concept, integrating it with advanced models to predict crack initiation influenced by both intrinsic and extrinsic defects [8].

To achieve defect-free finishing during high-stress operations like grinding, researchers have proposed various process criteria [13], [14]. These criteria typically focus on controlling thermal fields, mechanical loads, and the local stress intensity to ensure they remain below the material's fracture toughness (K_{IC}) or intrinsic strength thresholds [11], [15]. Extending this foundation, the concept of the hereditary defect (R_0) provides a specific, deterministic criterion within the weakest link framework, allowing process optimization to be tied directly to the size of the largest known inherited flaw [15], [16]. This specific focus on an inherited, process-traceable defect is essential for establishing safe technological windows during finishing.

To operationalize defect-free processing, numerous studies have focused on linking grinding parameters to the resulting thermomechanical fields. Phenomenological and mathematical models have been developed that relate variables like cutting force, wheel speed, and depth of cut to the local temperature and stress state of the surface layer [16].

Central to this work is the establishment of limiting inequalities or criteria for key thermomechanical parameters, which must not be exceeded to prevent crack formation [15], [17]. For instance, research explicitly defines maximum allowable heat flux and tangential stress based on material properties and defect characteristics [15], [17]. Experimental validation has confirmed that by keeping these thermomechanical fields below the critical thresholds for crack initiation—such as by establishing explicit process windows—surface quality can be guaranteed, even in materials prone to cracking [18]. The integration of such robust limiting criteria with the quantification of the specific hereditary defect (R_0) forms the basis for a comprehensive technological assurance methodology for precision finishing.

3. Research objectives

The objectives of this study are as follows:

1. To develop a mathematical model for detecting hereditary subsurface defects in ferromagnetic parts by analysing magnetic induction distributions and estimating defect geometry and depth.

2. To investigate the mechanisms of technological crack formation in ferroceramic materials based on the “weakest link” hypothesis and the influence of inherited structural defects.
3. To derive analytical conditions and limiting inequalities for thermal, mechanical, and fracture-related parameters that prevent the growth of structural defects into main cracks during finishing operations.
4. To determine optimal grinding modes and tool characteristics that ensure defect-free machining of ferroceramic products and to establish technological guidelines for improving the quality of machined surfaces.

4. Research methods

Consider the mathematical basis of the problem. Fig. 1 schematically shows the location of a part of the ferromagnetic material under the surface at a depth h of a cylindrical defect with radius R. The part is magnetized by a magnetic field source. Typically, defects have a shape similar to an elongated ellipse along one axis. If magnetization occurs along this axis, the magnetic field dispersion will be insignificant compared to magnetization across the axis. Therefore, it is important to determine the most effective direction of magnetization. The resistance of the defect to the magnetizing field should be as high as possible. Therefore, a cylinder that resists the magnetizing magnetic field, the cross-section of which is a circle (Fig. 1), was chosen as the calculation model.

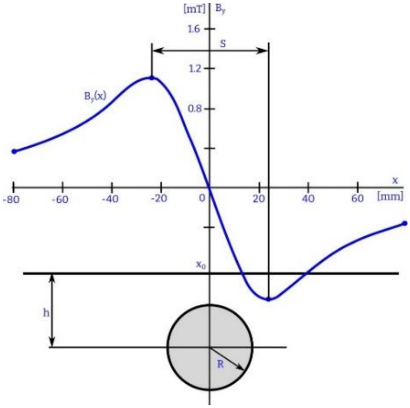

Fig. 1. Distribution of the normal component of the magnetic induction vector $\vec{B}_y(x)[mT]$ on the surface of the part along the x-axis, [mm] from the center of the defect

The magnetic induction of the magnetizing magnetic field B_0 is set by the magnetizing source. The magnetic permeability of the material of the part is μ_F. It is necessary to establish the distribution of the induction of the magnetic field displaced by the defect to the surface of the part. The problem is described by Laplace's differential equation, which in polar coordinates for the vector magnetic potential $A(\varphi, r)$ has the form [19]:

$$\frac{\partial^2 A(\varphi,r)}{\partial r^2} + \frac{1}{r} \cdot \frac{\partial A(\varphi,r)}{\partial r} + \frac{1}{r^2} \cdot \frac{\partial^2 A(\varphi,r)}{\partial \varphi^2} = 0 \tag{1}$$

The solution to the problem was obtained using Fredholm integral equations of the second kind and the principle of mirror reflections [20]. First, let us consider the problem without taking into account the influence of the surface of the part. The cylindrical defect is located in an unlimited ferromagnetic space (Fig. 2).

In polar coordinates, we will seek the expression for the vector magnetic potential in the following form: $A(\varphi, r) = C(\varphi) \cdot r + D(\varphi)/r$, where $C(\varphi)$ and $D(\varphi)$ are unknown functions of the argument φ. For the region occupied by the defect, we write:

$$A_1(\varphi,r) = C_1(\varphi) \cdot r + \frac{D_1(\varphi)}{r} \tag{2}$$

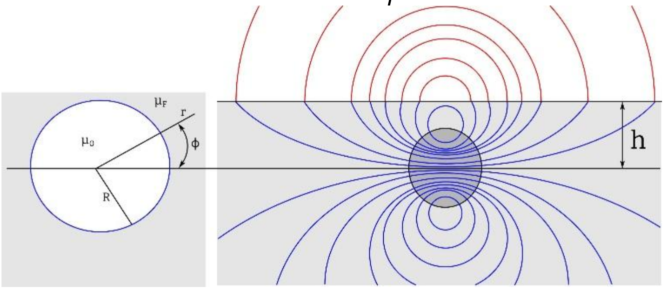

Fig. 2. Cylindrical defect in unlimited space and the pattern of magnetic field scattering by the defect in the form of magnetic field lines

For the region occupied by the ferromagnet:

$$A_2(\varphi,r) = C_2(\varphi) \cdot r + \frac{D_2(\varphi)}{r} \tag{3}$$

Components of the magnetic induction vector:

$$B_r(\varphi,r) = \frac{1}{r} \cdot \frac{\partial A}{\partial \varphi} = \frac{\partial C(\varphi)}{\partial \varphi} + \frac{1}{r^2} \frac{\partial D(\varphi)}{\partial \varphi} \tag{4}$$

$$B_\varphi(\varphi,r) = -\frac{\partial A}{\partial r} = -C(\varphi) + \frac{1}{r^2} \cdot D(\varphi) \tag{5}$$

The unknown functions $C_1(\varphi)$, $C_2(\varphi)$, and, $D_1(\varphi)$, $D_2(\varphi)$ for each of the regions, respectively, are found through boundary conditions, taking into account the physical characteristics of the magnetic field at individual points. At the point $r = 0$, the vector magnetic potential cannot reach infinity. Therefore, $D_1(\varphi) = 0$. In polar coordinates, the components of the magnetic induction vector will be: $B_r = B_0 \cdot cos\, \varphi$ and $B_\varphi = B_0 \cdot sin\, \varphi$.

Therefore, in the ferromagnetic region: $C_{2\varphi} = B_0 \cdot sin\, \varphi$. At the boundary between the two regions, the following boundary conditions must be satisfied: $B_{1r} = B_{2r}$ and $H_{1\varphi} = H_{2\varphi}$. After taking into account the above conditions in (4) and (5), we obtain a system of equations for two unknown functions:

$$\frac{\partial C_1(\varphi)}{\partial \varphi} = \frac{1}{R^2} \cdot \frac{\partial D_2(\varphi)}{\partial \varphi} + B_0 \cdot cos\, \varphi$$

$$-\frac{1}{\mu_0} \cdot C_1(\varphi) = -\frac{1}{\mu_F} \cdot B_0 \cdot sin\, \varphi + \frac{1}{\mu_F} \cdot \frac{1}{R^2} \cdot D_2(\varphi)$$

Omitting detailed mathematical calculations, we write expressions for the vector magnetic potential and the components of the magnetic induction vector of the magnetic field scattered by the defect.

For the region inside the defect:

$$A_1(\varphi, r) = \frac{2 \cdot \mu_0}{\mu_F + \mu_0} \cdot B_0 \cdot r \cdot sin\, \varphi \tag{6}$$

$$B_{1r}(\varphi, r) = \frac{2 \cdot \mu_0}{\mu_F + \mu_0} \cdot B_0 \cdot cos\, \varphi \tag{7}$$

$$B_{1\varphi}(\varphi, r) = -\frac{2 \cdot \mu_0}{\mu_F + \mu_0} \cdot B_0 \cdot sin\, \varphi \tag{8}$$

For the area outside the defect:

$$A_2(\varphi, r) = B_0 \cdot r \cdot sin\, \varphi - \frac{\mu_F - \mu_0}{\mu_F + \mu_0} \cdot B_0 \cdot R^2 \cdot \frac{1}{r} \cdot sin\, \varphi \tag{9}$$

$$B_{2r}(\varphi, r) = \frac{1}{r} \cdot \frac{\partial A}{\partial \varphi} = B_0 \cdot cos\, \varphi - \frac{\mu_F - \mu_0}{\mu_F + \mu_0} \cdot B_0 \cdot R^2 \cdot \frac{1}{r^2} \cdot cos\, \varphi \tag{10}$$

$$B_{2\varphi}(\varphi, r) = -\frac{\partial A}{\partial r} = -B_0 \cdot sin\, \varphi - \frac{\mu_F - \mu_0}{\mu_F + \mu_0} \cdot B_0 \cdot R^2 \cdot \frac{1}{r^2} \cdot sin\, \varphi \tag{11}$$

The tangential component in the ferromagnetic region has the following form:

$$B_{1sx} = B_0 + \frac{(\mu_F - \mu_0) \cdot R^2 \cdot B_0 \cdot [h^2 - (x - x_0)^2]}{(\mu_F + \mu_0) \cdot [(x - x_0)^2 + h^2]^2} \tag{12}$$

In the non-ferromagnetic region $B_{2sx} = \mu_0/\mu_F \cdot B_{1sx}$. The value of this component will be two, or even three orders of magnitude smaller. That is, its influence can be neglected externally. However, the normal component is continuous:

$$B_{2sy} = B_{1sy} = \frac{2 \cdot (\mu_F - \mu_0) \cdot (x - x_0) \cdot h}{(\mu_F + \mu_0) \cdot [(x - x_0)^2 + h^2]^2} \cdot R^2 \cdot B_0 \tag{13}$$

Analysis of expression (13) shows that at the point $x = x_0$ the normal component passes through zero. The maxima of the normal component are located symmetrically around zero at a distance $s = 2 \cdot h/\sqrt{3}$ one from another. At these points, the value of the normal component is equal to:

$$B_{xm} = \frac{(\mu_F - \mu_0)}{(\mu_F + \mu_0)} \cdot \frac{9 \cdot R^2}{8 \cdot \sqrt{3} \cdot h^2} \cdot B_0 \tag{14}$$

The results of the analysis of the normal component allow us to estimate the depth of the defect location:

$$h = 0.5 \cdot s \cdot \sqrt{3}$$

and, based on the maximum value of the normal component, its radius:

$$R = \frac{2}{3} \cdot \sqrt{2 \cdot \sqrt{3} \cdot \frac{\mu_F + \mu_0}{\mu_F - \mu_0} \cdot \frac{B_{ym}}{B_0}} \cdot h \tag{15}$$

The mechanism of formation of technological cracks on the machined surface of parts made of ferroceramic materials can also be studied from the standpoint of the "weakest link" hypothesis, which should be understood as a structural parameter, the size of which is selected as a criterion for defect-free machining according to the formula [21]:

$$R_0 < \frac{K_C^2}{\pi[GT_k(1 + \nu)\alpha_t]^2} \tag{16}$$

where G is the modulus of elasticity of the second kind of ferroceramic material; K_C^2 is the crack resistance of the ferroceramic material of the blank after sintering; α_t is a temperature coefficient of the blank material; T_k is the contact temperature in the grinding zone of the blank; ν is the Poisson's ratio.

Formula (16) provides a simple sufficient criterion under which a crack-like defect R_0 will not turn into a main crack.

If the inclusions are elliptical in shape, instantaneous local heating of the surface layer of the magnet in the contact zone may result in the formation of a disk-shaped crack. This is because during grinding, under the influence of both thermoelastic stresses and cutting forces on the edges of a disk-shaped defect with radius R, forces P arise along the axis of this defect [22]:

$$P = G(1 + \nu)\alpha_t T_k \iint_{(S)} (\vec{n}_z, \overline{ds}) = G(1 + \nu)\alpha_t T_k S_0 \tag{17}$$

where S_0 is the area of the defect boundary projection on the crack plane.

The stress intensity factor is determined for this case using the formula:

$$K_I = \frac{P}{(\pi R)^{3/2}} \tag{18}$$

Using viscosity, the destruction of ferrites at the radius of the disk-shaped defect found is achieved, which, when the conditions are met:

$$R \leq \frac{1}{\pi}\left[\frac{G(1+\nu)\alpha_t T_k S_0}{K_{1C}}\right]^{2/3} \tag{19}$$

will not develop into a main crack. In the case of an ellipsoidal shape, we have the following:

$$S = 4ab, \qquad R = \frac{1}{\pi}\left[\frac{4G(1+\nu)\alpha_t ab T_k}{K_{1C}}\right]^{2/3} \tag{20}$$

Here, a and b are the major semi-axes of the ellipse in the cross-section of the ellipsoid of the disk-shaped crack.

The obtained analytical conditions (16), (19), (20) for the equilibrium of structural defects, the size R (in the case of the "weakest" link) depend on the crack resistance coefficient K_{1C}, the coefficients ν, G, α_t as well as the value of the contact temperature T_k, which is determined by the operating part in the finishing operations.

5. Research results

When developing technological criteria for controlling the defect-free machining process, it was taken into account that this process is multifactorial. The quality of the surface layer during the processing of parts is influenced by the physical and mechanical properties of the material being processed, its structure, grinding modes, and wheel characteristics, the conditions of preliminary treatment with lubricating and cooling media (LCM) for the tool, as well as the characteristics of the cooling and lubricating fluids used.

Therefore, to ensure the quality of the processed surfaces, it is necessary to select the processing modes, LCM, and tool characteristics based on the functional relationships between the physical and mechanical properties of the materials and the grinding process parameters, so that the current values of the grinding temperature $T\ (x, y, \tau)$ and heat flux $q(y, \tau)$, stress $\sigma_{p\,max}$ and grinding forces P_Y, P_Z stress intensity factor $К_1(S, \alpha, \sigma_{p\,max})$ do not exceed their specific values for defects of certain geometric dimensions, ensuring the required quality of the surface layer [23], [24].

Consider the following system of boundary inequalities which allows us to proceed to the construction of an algorithm for selecting technological parameters that ensure the required quality of the machined surfaces.

When studying the kinetics of the temperature field of a part, taking into account the peculiarities of cutting with single grains of the tool, it was found that it consists of regular (constant) and instantaneous (pulse) components. The impulse component T_m describes the temperature state of the machined surface directly under the cutting grain. The constant component, T_k, characterizes the heating of the product surface in the machining zone as a result of the combined action of many tool grains.

Despite its short duration, instantaneous temperature on the treated surface, and rapid decay in depth, it nevertheless participates in the formation of a structurally stressed state of the thin surface layer of the part. Therefore, the limiting inequalities of the temperature itself and the depth of its propagation will be equal [25]:

$$T(x,y,\tau)=\frac{C}{2\pi\lambda}\sum_{k=0}^{n}H\left(\tau-\frac{kl}{V_s}\right)H\left(\frac{L+kl}{V_s}\right)\int_{\gamma_1}^{\gamma_2}f(\tau,\tau')d\tau'\leq[T]_M \tag{21}$$

$$T([h],0,\tau)=\frac{C}{2\pi\lambda}\sum_{k=0}^{n}H\left(\tau-\frac{kl}{V_s}\right)H\left(\frac{L+kl}{V_s}\right)\int_{\gamma_1}^{\gamma_2}\psi(\tau,\tau')d\tau'\leq[T]_{avg} \tag{22}$$

where

$$\psi(\tau,\tau')=exp\left[-\frac{V_d(kl-V_s\tau')}{2a}-\frac{V_d^2(\tau-\tau')}{4a}-\frac{(kl-V_s\tau')^2+[h]^2}{4a(\tau-\tau')}\right] \tag{23}$$

and $[T]_{avg}$ is the permissible temperature for the functional properties of this material; $[h]$ is the maximum permissible depth of loss of their properties.

In some cases, the loss of surface layer quality becomes significant only when structural transformations spread to a certain depth, the value of which is determined by the operating conditions of the products and, possibly, indirectly, by technical conditions. The limit values of this depth are determined by the zone of deeper heating, i.e., the constant component of the temperature field. The limit inequalities in this case are as follows [26]:

$$\begin{aligned}T_k(o,y,\tau)=\frac{CV_s}{\pi\lambda l\sqrt{V_\mathrm{d}}}\int_0^{\tau}\int_{-e}^{e}\frac{x(r,t)e^{-\frac{(y-r)^2}{4(\tau-t)}}}{2\sqrt{\pi(\tau-t)}}\left\{\frac{1}{\sqrt{\pi(\tau-t)}}\right.\\ \left.+\gamma e^{y^2(\tau-t)}\left[1+\Phi(\gamma\sqrt{\tau-t})\right]\right\}drdt\leq T_{str}\end{aligned} \tag{24}$$

$$\begin{aligned}&T_k([h],0)\\&=\frac{CV_s}{\pi\lambda l\sqrt{V_d}}\int_0^{\sqrt{Dt_{gr}}}\sqrt{[h]^2+y'^2}e^{-\frac{V_dy'}{2a}}K_{1/2}\left(\frac{V_d}{2a}\sqrt{y'^2+[h]^2}\right)dy'\leq[T]_{pr}\end{aligned} \tag{25}$$

$$T_k^{max}(L,0)\frac{CV_sa}{\lambda lV_d^2}\sqrt{\frac{a}{\pi}}\left[1-exp\left(-\frac{V_d\sqrt{Dt_{gr}}}{a}\right)\right]\leq[T] \tag{26}$$

In the last inequality, the limiting temperature at the surface ($X=0$) is used as the limiting coefficient.

The formation of grinding cracks depends on the magnitude of temporary stresses formed in the surface layer under the influence of thermomechanical phenomena accompanying this process. Maximum stresses occur in the zone of intensive cooling. Therefore, the structure of the control inequality for defect-free processing in this case will be as follows [23], [24]:

$$\sigma_{max}(x,\tau) = 2G\frac{1+\nu}{1-\nu}\alpha_t T_k^{max} erf\left(\frac{x}{2\sqrt{a\tau}}\right) \leq [\sigma] \tag{27}$$

The phenomenological approach to assessing metal cracking phenomena during grinding does not take into account many technological factors, in particular, the influence of the heat treatment modes of these metals and the defectiveness of their structure associated with previous types of mechanical processing. Therefore, a more "sensitive" limit parameter is needed, the structure of which would include functional links between the technological parameters of diamond-abrasive processing and take into account technological inheritedness [13], [27].

As such, the stress intensity factor limit can be used, with its established ratios to technological parameters, as the main criterion for the crack resistance of metals – the K_{1C} coefficient, i.e. [24], [27]:

$$K_1 = \frac{1}{\pi\sqrt{l}}\int_{-l}^{l}\sqrt{\frac{l+t}{l-t}}\{\sigma_{xx},\sigma_{yy}\}dt \leq K_{1C} \tag{28}$$

where $2l$ is the characteristic linear size of the structural defect.

Defect-free processing of materials with low mechanical characteristics is possible if the cutting forces, in particular the tangential component – P_Z, are limited and the friction coefficient between the tool and the processed metal – ρ is reduced.

Thus, based on studies of the effect of cutting forces on the stress state of the surface layer, another additional condition for defect-free processing can be formulated [24]:

$$P_z \leq \frac{\pi\sqrt{Dt_{gr}}}{KP^2 \sin\pi\,\theta}\left[[\tau]_C - \frac{E\rho\sqrt{Rt}}{2(1-\nu^2)\sqrt{R}}\right] \tag{29}$$

where $[\tau]$ is the limit value of the tangential shear stress; $\theta = \frac{1}{\pi}arctan\frac{1-2\nu}{2\rho(1-\nu)}$; ρ is the minimum possible value of the friction coefficient between the abrasive and the metal being processed, which is ensured by the use of a heat transfer medium and impregnating substances; K is the ratio coefficient, P_Y/P_Z.

To verify criterion (29) for the absence of grinding cracks on the machined surface of ferroceramic materials, we will determine the contact temperature in the grinding zone. Taking into account that the dominant factor among the grinding modes affecting the thermal stress of the grinding process is h - the grinding depth, the dependence $T = f(h)$ was found (Fig. 3). The remaining modes were selected from the conditions of maximum productivity while maintaining the required quality and were selected as follows: $V_d = 0.17$ m/s; $V_s = 30$ m/s; $S_{non} = 5$ mm. The following grinding wheels were selected for the study: wheel 1 – the ACP B1 diamond wheel with grain size 100/80, represented by its European analogue Tyrolit

4BT9 D91; wheel 2 – the ASK synthetic diamond wheel 250/200 MO16 (100% concentration), substituted with the DIAMOS metal-bond diamond wheel 1A1R DIA126 C100 BX; and wheel 3 – the electrocorundum wheel 24A 25 CM/8K5, replaced by the aluminium-oxide wheel Flexovit A24 V-BF42 (e.g., article 66252831164).

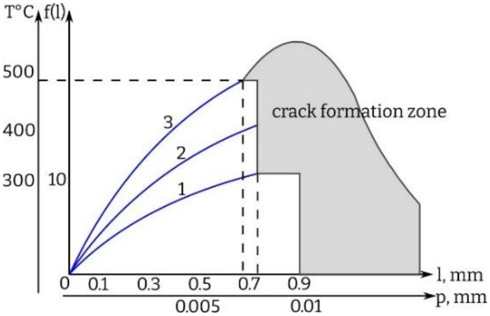

Fig. 3 Calculated and experimental values of the maximum sizes of crack-like defects when grinding ferroceramic products with wheels

Experimental studies have shown that wheels made of natural and synthetic diamonds have stable cutting ability, high dimensional stability, and a relatively low temperature in the grinding zone, which also affects the absence of cracks at large grinding depths (compared to 24A25CM18K5 wheels).

It was found that the most productive way to maintain the required quality of grinding the working surface of ferroceramic products is with ACPB1 diamond wheels with a grain size of 100/80 (curve I, Fig. 3).

Since porosity (size and density) during sintering of the workpiece is regulated by the temperature regime, as well as the speed of passage through the tunnel kiln [28], it is possible to avoid the appearance of grinding cracks on the machined surface by selecting the appropriate grinding modes and wheel characteristics.

The results of studying the microhardness of the treated surface and the microstructure of the surface layer indicate that in the range of modes studied, there are no cracks or chips during the grinding of ferroceramic products.

The nature of crack formation in ferroceramic products depending on the characteristics of the wheels and cutting modes can be traced using the criterion of the limiting heat flux q^* [29]:

$$q^* = \frac{P_z V_s \alpha_s}{\sqrt{D t_{gr}}} \le \frac{\sqrt{3}\lambda K_{1c}}{H l \sqrt{\pi l} \sigma} \tag{30}$$

The heat flow entering the part during grinding is not only a function of the cutting modes, V_d, V_s, t_{gr}, P_Z, but also of the characteristics of the wheels – the hardness of the bond, the grain size of the cutting grains, their hardness, etc. Therefore, it should be expected that each wheel has its own limit heat flow value at which the machined surface of a ferroceramic product containing pores of size $2l$ will not be subject to cracking.

The following studies were conducted to rank the wheels according to the maximum heat flux criterion. Products made of ferroceramic MnFe2O4 materials containing air pores were ground with different wheels at grinding depths at which cracks appeared on the surface. At the same time, the heat flux q was measured by cutting power, the contact temperature T_K (using a semi-artificial thermocouple), and the instantaneous temperatures T_M and specific grinding work were recorded. It was found that the intensity of crack formation on the machined surfaces for different wheels was fairly well corrected with the limit values of the heat flux. The lowest heat flux q^* is possessed by diamond wheels with a grain size of 100/125 on organic bonds, which can be recommended for grinding ferroceramic products.

Diamond wheels with a grain size of 200/250 can be recommended for preliminary grinding operations, which ensures better quality and productivity.

The resulting irregularities are related to the limiting characteristics of the temperature and force fields with the controlling technological parameters. They determine the range of combinations of technological parameters (modes, cooling lubricant medium, tool characteristics) that ensure the required quality of the working surfaces of products made of ferroceramic materials [14], [30].

6. Conclusions

As a result of the research, information support for technological capabilities for defect-free processing of ferroceramic materials prone to cracking has been created, which consists in establishing calculated dependencies for determining the influence of hereditary defects formed at the stage of sintering the blank on the crack resistance of the surface layer in the finishing operations. technological processing conditions, taking into account the accumulated defects in the surface layer of ferroceramic parts, which are particularly prone to cracking during processing, which is of great economic importance for reducing defects in finishing operations and improving the operational properties of parts made of these materials.

References: **1.** *M. Brown et al.*, ‘Destructive and non-destructive testing methods for characterization and detection of 5.machining-induced white layer: A review paper’, CIRP Journal of Manufacturing Science and Technology, vol. 23, pp. 39–53, Nov. 2018, doi: 10.1016/J.CIRPJ.2018.10.001. **2.** *T. Chady, R. D. Łukaszuk, K. Gorący, and M. J. Żwir*, ‘Magnetic Recording Method (MRM) for Nondestructive Evaluation of Ferromagnetic Materials’, Materials, vol. 15, no. 2, p. 630, Jan. 2022, doi: 10.3390/ma15020630. **3.** *C. Ma, Y. Liu, and C. Shen*, ‘Phase-Extraction-Based MFL Testing for Subsurface Defect in Ferromagnetic Steel Plate’, Sensors, vol. 22, no. 9, p. 3322, Apr. 2022, doi:

10.3390/s22093322. **4.** *Z. Deng et al.*, ‘Magnetic Permeability Perturbation Testing Based on Pulse Magnetization for Buried Defect in Ferromagnetic Material’, IEEE Sensors J., vol. 25, no. 11, pp. 18952–18961, June 2025, doi: 10.1109/JSEN.2025.3561844. **5.** *K. Kosmas and E. Hristoforou*, ‘The effect of magnetic anomaly detection technique in eddy current non-destructive testing’, International Journal of Applied Electromagnetics and Mechanics, vol. 25, no. 1–4, pp. 319–324, Feb. 2007, doi: 10.3233/JAE-2007-826. **6.** *X. Hu et al.*, ‘Research on Quantitative Evaluation of Defects in Ferromagnetic Materials Based on Electromagnetic Non-Destructive Testing’, Sensors, vol. 25, no. 11, p. 3508, June 2025, doi: 10.3390/s25113508. **7.** Z. Qian, H. Zeng, H. Liu, Y. Ge, H. Cheng, and H. Huang, ‘A prototype method to evaluate the inner wall defects of ferromagnetic materials based on a two-stage magnetic combined detection’, *Journal of Magnetism and Magnetic Materials*, vol. 560, p. 169564, Oct. 2022, doi: 10.1016/j.jmmm.2022.169564. **8.** *D. Leguillon, E. Martin, O. Sevecek, and R. Bermejo*, ‘What is the tensile strength of a ceramic to be used in numerical models for predicting crack initiation?’, Int J Fract, vol. 212, no. 1, pp. 89–103, July 2018, doi: 10.1007/s10704-018-0294-7. **9.** *F. Hild, D. Marquis, O. Kadouch, and J.-P. Lambelin*, ‘Analysis of the Failure of Ceramics Due to Subcritical Crack Growth’, Journal of Engineering Materials and Technology, vol. 118, no. 3, pp. 343–348, July 1996, doi: 10.1115/1.2806816. **10.** *W. Weibull*, ‘A Statistical Distribution Function of Wide Applicability’, Journal of Applied Mechanics, vol. 18, no. 3, pp. 293–297, Jan. 1951. **11.** *M. Boåsen, C. F. O. Dahlberg, P. Efsing, and J. Faleskog*, ‘A weakest link model for multiple mechanism brittle fracture — Model development and application’, Journal of the Mechanics and Physics of Solids, vol. 147, p. 104224, Feb. 2021, doi: 10.1016/j.jmps.2020.104224. **12.** *F. W. Zok*, ‘On weakest link theory and Weibull statistics’, J. Am. Ceram. Soc., vol. 100, no. 4, pp. 1265–1268, Apr. 2017, doi: 10.1111/jace.14665. **13.** *A. Usov, M. Kunitsyn, D. Klymenko, and V. Davydiuk*, ‘Modeling the effect of stochastic defects formed in products during machining on the loss of their functional dependencies’, Pratsi OPU, vol. 1, no. 65, pp. 16–29, 2022, doi: 10.15276/opu.1.65.2022.02. **14.** *M. Kunitsyn, A. Usov, and Y. Zaychyk*, ‘Information technologies of the analysis for models to ensure quality characteristics of the working surfaces during mechanical processing’, in Advances in Design, Simulation and Manufacturing VI, V. Ivanov, J. Trojanowska, I. Pavlenko, E. Rauch, and J. Piteľ, Eds, Cham: Springer Nature Switzerland, 2023, pp. 274–285. doi: 10.1007/978-3-031-32767-4_26. **15.** *A. V. Usov, M. V. Kunitsyn, and Y. I. Zaychyk*, ‘An information model concept for a thermomechanical process in grinding’, HAIT, vol. 6, no. 3, pp. 250–262, Oct. 2023, doi: 10.15276/hait.06.2023.17. **16.** *A. Usov, Y. Zaychyk, M. Kunitsyn, and Y. Sikirash,* ‘Levereging technological heredity to increase production efficiency of ferrocerramic products during final machining’, Cutting & Tools, no. 100, pp. 168–185, June 2024, doi: 10.20998/2078-7405.2024.100.12. **17.** *A. V. Usov, L. A. Vorobyova, and S. G. Smirny*, ‘Research of thermomechanical effects at grinding materials and alloys apt to crack rise’, EEJET, vol. 2, no. 7(74), p. 48, Apr. 2015, doi: 10.15587/1729-4061.2015.39422. **18.** *J. Zhang, X. Shang, B. He, and B. Zhang*, ‘Towards understanding the crack suppression mechanism in brittle materials with high grinding speed at different temperatures’, International Journal of Machine Tools and Manufacture, vol. 193, p. 104088, Dec. 2023, doi: 10.1016/j.ijmachtools.2023.104088. **19.** *B. Guo, Y. Huang, F. Peng, and J. Dong*, ‘General analytical modeling for magnet demagnetization in surface mounted permanent magnet machines’, IEEE Transactions on Industrial Electronics, vol. 66, no. 8, pp. 5830–5838, Aug. 2019, doi: 10.1109/TIE.2018.2873099. **20.** *J. Y. Lee*, ‘Generic algorithm of magnetic particle inspection using finite element modeling’, AIP Conf. Proc. pp. 437–444, Apr. 2004, doi: 10.1063/1.1711655. **21.** *O. G. Diaz, D. A. Axinte, P. Butler-Smith, and D. Novovic*, ‘On understanding the microstructure of SiC/SiC Ceramic Matrix Composites (CMCs) after a material removal process’, Materials Science and Engineering*: A*, vol. 743, pp. 1–11, Jan. 2019, doi: 10.1016/J.MSEA.2018.11.037. **22.** *Y. Yin et al.*, ‘Study on thermal damage formation mechanisms and surface integrity in creep-feed profile grinding of superalloys’, Journal of Manufacturing Processes, vol. 120, pp. 28–50, June 2024, doi: 10.1016/J.JMAPRO.2024.03.114. **23.** *J. P. Davim, et al.,* Modern mechanical engineering: research, development and education. in Materials Forming, Machining and Tribology. Berlin, Heidelberg: Springer, 2014. doi: 10.1007/978-3-642-45176-8. **24.** *G. Y. Popov*, ‘On Some Integral Transformations and Their Application to the Solution of Boundary-Value Problems in Mathematical Physics’, Ukrainian Mathematical Journal, vol. 53, no. 6, pp.

951–964, 2001. **25.** *V. Gurey, P. Maruschak, I. Hurey, V. Dzyura, T. Hurey, and W. Wojtowicz*, ‘Dynamic Analysis of the Thermo-Deformation Treatment Process of Flat Surfaces of Machine Parts’, JMMP, vol. 7, no. 3, p. 101, May 2023, doi: 10.3390/jmmp7030101. **26.** *P. Ehrhard, C. Hölle, and C. Karcher*, ‘Temperature and penetration depth prediction for a three-dimensional field below a moving heat source’, International Journal of Heat and Mass Transfer, vol. 36, no. 16, pp. 3997–4008, 1993, doi: 10.1016/0017-9310(93)90150-5. **27.** *E. G. Ladopoulos*, ‘Singular integral operators method for two-dimensional plasticity problems’, Computers & Structures, vol. 33, no. 3, pp. 859–865, 1989, doi: 10.1016/0045-7949(89)90260-5. **28.** *D. O. Fedorenko, V. A. Fedorovich, E. Yu. Fedorenko, and K. B. Daineko*, ‘Ceramic-matrix composite materials for the diamond abrasive tools manufacture’, Scientific research on refractories and technical ceramics, vol. 117, pp. 212–224, July 2017, doi: 10.35857/2663-3566.117.20. **29.** *Q. Meng et al.*, ‘Modelling of grinding mechanics: A review’, Chinese Journal of Aeronautics, vol. 36, no. 7, pp. 25–39, July 2023, doi: 10.1016/j.cja.2022.10.006. **30.** *I. Pavlenko et al.*, ‘Parameter identification of cutting forces in crankshaft grinding using artificial neural networks’, *Materials*, vol. 13, no. 23, pp. 1–12, Dec. 2020, doi: 10.3390/MA13235357.

Анатолій Усов, Максим Куніцин, Юрій Зайчик, Юлія Сікіраш,
Одеса, Україна,

ВПЛИВ СПАДКОЄМНИХ ДЕФЕКТІВ, НА ТРІЩИНОУТВОРЕННЯ В ОБРОБЛЮВАНИХ ПОВЕРХНЯХ ВИРОБІВ ІЗ ФЕРОКЕРАМІЧНИХ МАТЕРІАЛІВ НА ФІНІШНИХ ОПЕРАЦІЯХ

Анотація. *Для забезпечення якості оброблюваних поверхонь, необхідно за функціональними зв'язками між фізико-механічними властивостями матеріалів і параметрами на фінішних операціях підбирати такі режими обробки, і характеристики інструменту таким чином, щоб поточні значення температури шліфування* $T(x,y,\tau)$ *і теплового потоку* $q(y,\tau)$ *напруження* $\sigma_{p\,max}$ *сил шліфування* P_Y , P_Z , *коефіцієнта інтенсивності* $K_1(S,\alpha_t,\sigma_{p\,max})$ *перевищували їх питомих значень, для дефектів певних геометричних розмірів, що містяться в поверхневому шарі і мають спадкоємний характер гарантувати необхідну якість робочих поверхонь виробів. В даній роботі розглянута математична постановка задачі по виявленню дефектів в феромагнітних деталях від попередніх операцій при їх намагнічувані. Отримано математичні вирази для оцінки геометричної форми і глибини розміщення дефекту в поверхні деталі за результатам вимірювання розподілу магнітної індукції на її поверхні. Механізм утворення технологічних тріщин на фінішних операціях поверхні деталей із ферокерамічних матеріалів розглядається з позицій гіпотези про «найслабшу» ланку, під яким слід розуміти спадкоємний дефект, розмір якого вибирається в якості критерію бездефектної обробки. У результаті виконаних досліджень створено інформаційне забезпечення технологічних можливостей для бездефектної обробки виробів із матеріалів, схильних до тріщиноутворення, що полягає у встановленні розрахункових залежностей щодо визначення впливу спадкових дефектів, сформованих від попередніх операцій на тріщиностійкість поверхневого шару на фінішних операціях. технологічних умов обробки з урахуванням накопичених пошкоджень і неоднорідностей у поверхневому шарі деталей із матеріалів і сплавів, особливо схильних до тріщиноутворення в процесі обробки, що має важливе значення для зменьшення дефектів на фінішних операціях та підвищення експлуатаційних властивостей деталей машин.*

Ключові слова*: спадкоємний дефект; тріщино-утворення; фінішна операція; феромагнітне моделювання; аналітичні залежності.*

ISSN 2078-7405 Cutting & Tools in Technological System, 2025, Edition 103

UDC 621.9.048 **doi: 10.20998/2078-7405.2025.103.07**

INVESTIGATION OF FUNCTIONAL SURFACE ROUGHNESS PARAMETERS ON STEEL SURFACES MACHINED BY ELECTRO-DISCHARGE MACHINING

Zsolt **Maros** [0000-0001-5029-3559], Krisztina **Kun-Bodnár** [0000-0003-1904-4479]

University of Miskolc, 3515 Miskolc-Egyetemváros, Hungary
zsolt.maros@uni-miskolc.hu

Received: 18 November 2025/ Revised: 26 November 2025/ Accepted: 29 November 2025 / Published: 15 December 2025

Abstract. *The surface quality produced by electrical discharge machining (EDM) nowadays allows these surfaces to be used directly as functional surfaces—often without the need for post machining—such as in the production of plastic moulding tools. This highlights the importance of surface quality assessment not only through traditional amplitude parameters but also through so-called functional roughness parameters. This paper presents the results of studies in which EDM machined tool steels were investigated using functional surface roughness parameters. Such parameters effectively characterize the operational behaviour and applicability of machined surfaces.*

Keywords: *electrical discharge machining (EDM); surface texture; functional roughness parameters; topological map.*

1. Introduction

Electrical discharge machining is widely used in tool manufacturing, particularly for producing plastic injection moulds. Fine structured surface quality (texture or pattern) is required on steel mould plates and inserts, which strongly influences the aesthetic quality of the moulded plastic components. The precision of the surface texture must be reproduced depends on several factors, including the material properties of the workpiece, the tool electrode material, the construction of the EDM machine, and numerous technological parameters.

EDM-machined surfaces consist of overlapping, irregularly located craters, whose formation is influenced by several parameters—voltage, current intensity, and pulse duration. Several authors have analysed EDM surface roughness as a function of technological parameters [1,2], but usually only in terms of traditional amplitude parameters (R_a, R_z, R_t).

Because crater formation results from pulsed melting and vaporisation, and because re-solidified material creates an irregular height distribution, amplitude roughness values are less informative. Therefore, it is more appropriate to analyse functional roughness parameters such as R_{sk}/R_{ku} and R_{mr}, which better describe whether the surface is peak- or valley-dominated and to what extent it can function as a real contact surface [3].

2. Material ratio and functional surface parameters

One of the most frequently used functional parameters is the material ratio (R_{mr}).

R_{mr} is defined as the ratio of the material cross-sections cut at a specified depth (p) below the surface peak level to the evaluation length (l_r) (Figure 1) [4]. Given as a percentage, a higher R_{mr} value generally indicates more favourable operational properties. Mathematically:

$$R_{mr(c)} = \frac{\sum_{i=1}^{n} b_i}{l_r} \qquad (1)$$

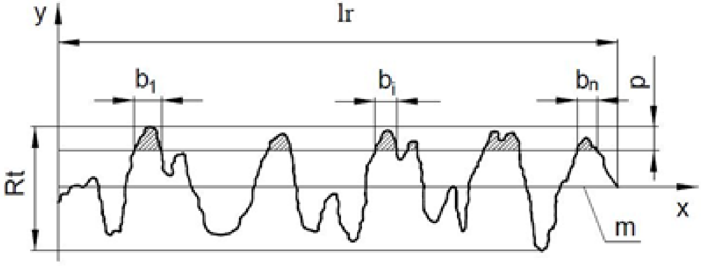

Figure 1 – Interpretation of the material ratio (R_{mr})

Skewness (R_{sk}) describes the asymmetry of the profile height distribution curve about its mean line:

$$R_{sk} = \frac{1}{R_q^3} \cdot \frac{1}{l_r} \int_0^{l_r} y(x)^3 dx \qquad (2)$$

where R_q is the root-mean-square roughness:

$$R_q = \sqrt{\frac{1}{l_r} \int_0^{l_r} y(x)^4 dx} \qquad (3)$$

Skewness (R_{sk}) indicates whether deviations are symmetric about the mean line or dominated by peaks (positive) or valleys (negative). For Gaussian surfaces—

where the distribution of height values is symmetric—$R_{sk} = 0$. R_{sk} is negative when the height-distribution curve extends more on the side above the mean plane, and positive in the opposite case (Figure 2). Negative skewness values indicate that the machined surface texture has good load-bearing capacity and is more wear-resistant. This parameter has very important technical and practical significance for real working surfaces.

Kurtosis (R_{ku}) characterizes the peakiness, sharpness, and thus the dispersion (range of dispersion) of the height distribution. Definition:

$$R_{ku} = \frac{1}{R_q^4} \cdot \frac{1}{l_r} \int_0^{l_r} y(x)^4 dx \qquad (4)$$

For the Gaussian surfaces, $R_{ku} = 3$. A high R_{ku} value usually indicates prominent peaks or valleys (or possibly both) (Figure 2). If $R_{ku} > 3$, surfaces sliding against each other will be characterized by intense wear. If $R_{ku} < 3$, the distribution of surface irregularities is much more favourable. In this case, the surface can be described as having a full, plateau-like profile.

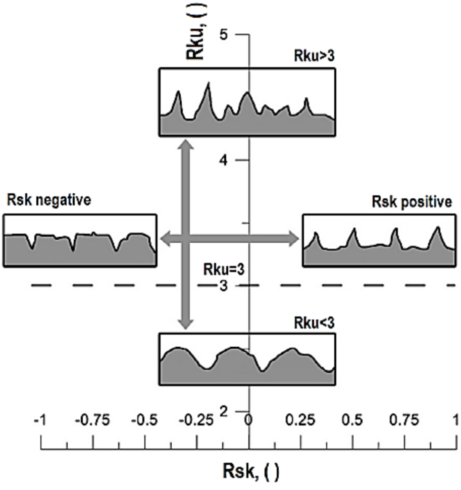

Figure 2 – Illustration of skewness (R_{sk}) and kurtosis (R_{ku})

In the present study, the material ratio, skewness, and kurtosis parameters were analysed on EDM-machined plastic mould tool steels.

3. Experimental conditions

Experiments were carried out on a Neuar CNC-C50 EDM machine-tool. Workpieces were mounted in a vise, and petroleum was used as the dielectric fluid.

Four tool steels commonly used for plastic injection moulding were investigated. Each specimen was machined by die-sinking EDM. The chemical composition of the steels is shown in Table 1.

The test pieces were rectangular plates (115 × 140 × 15 mm), pre-ground and hardened for more efficient EDM. Each sample contained 5 mm depth cavities (Figure 3), machined at different VDI grades using two electrode materials.

Table 1 – Chemical composition machined tool steels

Material	**C, %**	**Si, %**	**Mn, %**	**Cr, %**	**Mo,%**	**S, %**	**Ni,%**
40CrMnMo7	0,40	0,30	1,50	1,90	0,20		
40CrMnMoS8-6	0,40	0,40	1,50	1,90	0,20	0,08	
45NiCrMo16	0,48	0,23	0,40	1,30	0,25		4,00
C45U	0,45	0,30	0,70				

Figure 3 – Test specimen with cavities machined by EDM using two different tools

Each specimen contained five cavities produced at different VDI grades using two electrode types. On modern EDM machines, technological parameters influencing machining quality and efficiency—such as discharge current, voltage, and pulse duration—cannot be set manually; instead, the machine automatically selects them based on the chosen VDI grade (typically ranging from VDI 0 to VDI 45) [5]. The VDI grades chosen for this study were 18, 21, 25, 29, and 36..

To carry out the machining experiments, copper (red copper) and graphite electrodes were used for all test piece materials. The type of copper electrodes used was CuETP electrolytic copper and graphite of type ELOR-50-F, with a cross section of 55 x 15 mm.

The surface roughness of the machined cavities was measured in the laboratory of the Institute of Manufacturing Science at the University of Miskolc using an AltiSurf 520 three-dimensional surface topography device.

4. Experimental results

From the results of the EDM experiments, conclusions can be drawn about the effect of the set VDI grade, the different electrode materials, and the machined steel grades on the profile roughness in terms of the operational roughness parameters.

Figures 4 and 5 show the change in the material ratio parameter (R_{mr}) of the cavities made with copper and graphite electrodes at each VDI level. The material ratio (R_{mr}) is used to characterize the operating and wear properties of surfaces. The higher the percentage R_{mr} value of a given surface, the more favourable its operating properties. During the tests, the material ratio parameter values were determined at a depth of c = 10 μm.

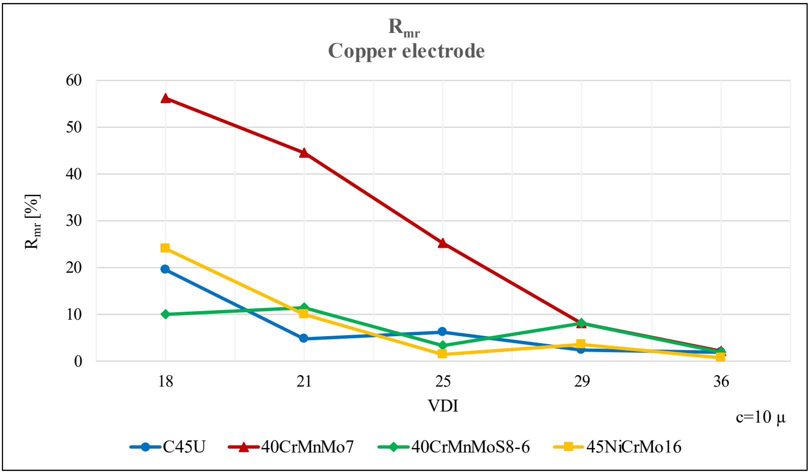

Figure 4 – Change in the R_{mr} parameter as a function of the VDI grade for copper electrodes

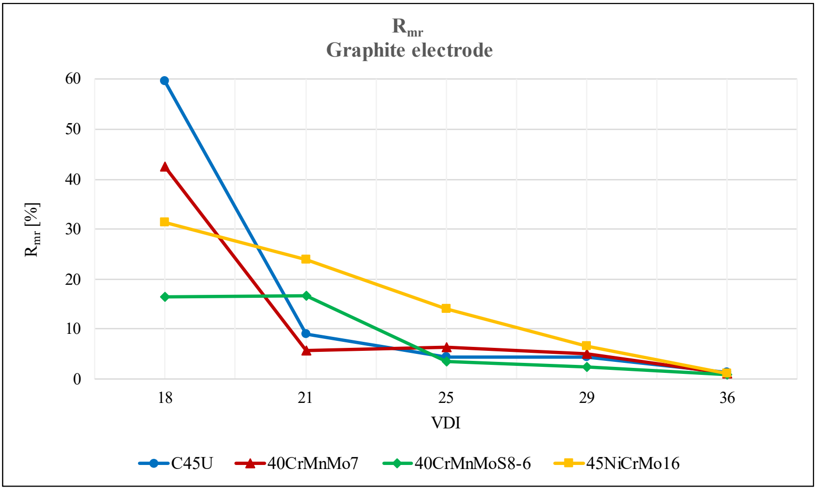

Figure 5 – Change in the R_{mr} parameter as a function of the VDI grade for copper electrodes

Figures 4 and 5 show that the most favourable operating properties are achieved at VDI grade 18 and that, as the VDI grades increase, the surface characteristics deteriorate and the difference in the material ratio parameter between the individual steels decreases, regardless of the tool and workpiece material. In the case of copper electrodes, outstanding properties can be achieved at EDM 40CrMnMo7 material, and in the case of graphite, the same can be said for C45U and 45NiCrMo16 steel. At VDI level 18, the lowest percentage values was obtained for the 40CrMnMoS8-6 material, which also contains sulphur alloying. At the other levels, the weaker values vary from level to level.

In addition to the R_{mr} material ratio parameter, the functional parameters R_{sk} skewness and R_{ku} kurtosis also have very important technical and practical significance for real working surfaces. A topological map can be created using the values of the R_{sk} - R_{ku} parameters. The topological map is a series of points plotted on an R_{sk} - R_{ku} plane, which gives the skewness and kurtosis parameters of the measured roughness of the manufactured surface. The corresponding values of R_{sk} and R_{ku} for surfaces produced using different cutting technologies form groups depending on the cutting technology (Figure 6). Surfaces produced using different technologies have different R_{sk} - R_{ku} values [6,7].

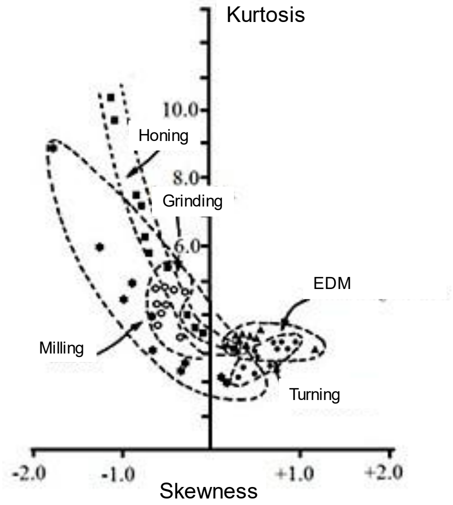

Figure 6 – Topological map of R_{sk} - R_{ku} for surfaces produced using different cutting processes [6]

To evaluate measurement results, a topological map was created from the measured data, also marking the theoretical location of EDM technology (Figures 7 and 8).

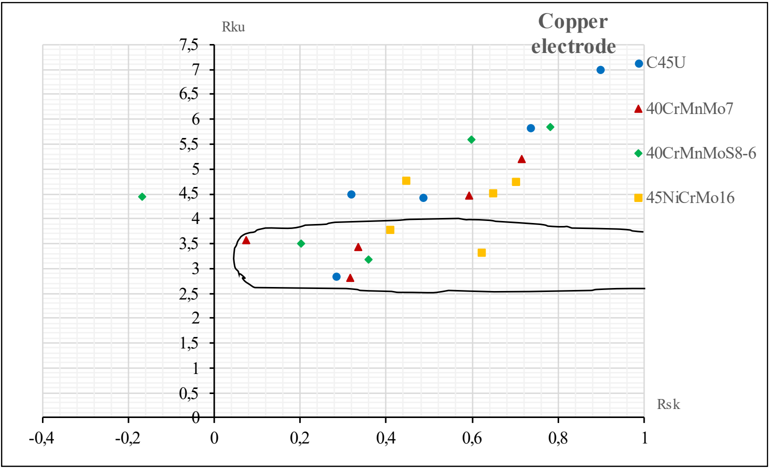

Figure 7 – R_{sk} - R_{ku} topological map for surfaces machined with copper electrodes

Considering that the most favourable properties in terms of operation are given by the parameter pairs R_{sk} - R_{ku} parameter pairs located furthest to the left and below, we can conclude from the measurement results that these data pairs were best achieved on surfaces of 40CrMnMoS8-6 steel with a copper electrode and on surfaces of 45NiCrMo16 steel with a graphite electrode.

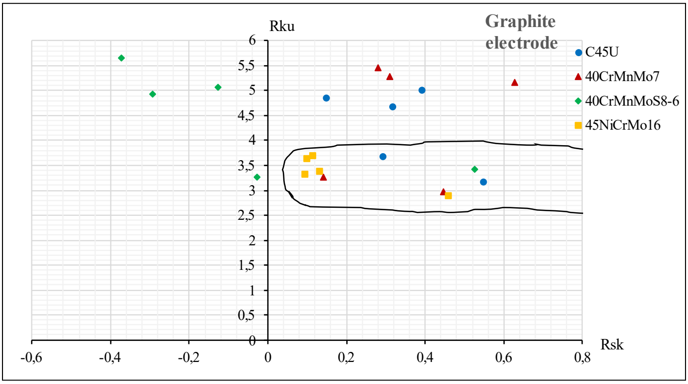

Figure 8 – R_{sk} - R_{ku} topological map for surfaces machined with graphite electrodes

No clear result was obtained for the tool steel with the most unfavourable properties. Examining the technological area of EDM as defined in the literature, it can be said based on the measured values that the measurement points of the material

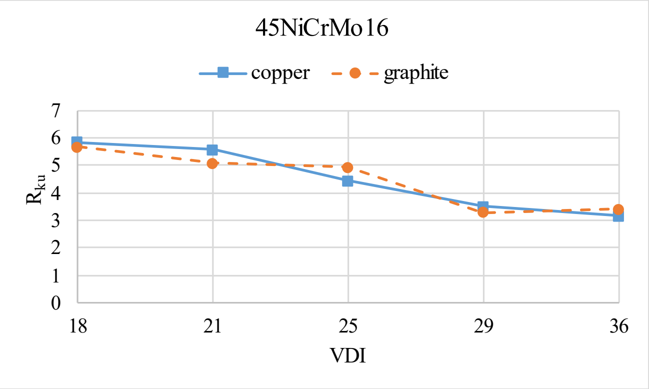

Figure 9 – Variation of R_{ku} peaking as a function of VDI grade on 45NiCrMo16 tool steel

grades with the most favourable properties did not necessarily fall within the theoretically designated area. Figures 9 and 10 show the change in R_{sk} and R_{ku} values as a function of the set VDI grades.

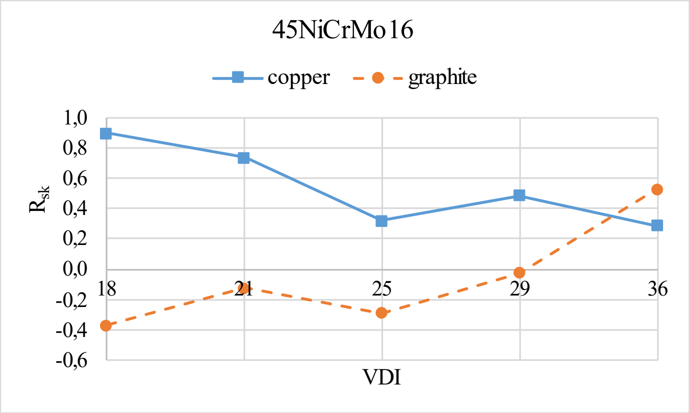

Figure 10 – Variation of R_{sk} skewness as a function of VDI grade on 45NiCrMo16 tool steel

It is interesting to note that the peak value decreases at higher VDI levels, approaching the value of 3, which is considered favourable in the literature. The two types of electrodes produce almost identical results (Figure 9). No clear conclusion can be drawn regarding skewness, as skewness decreases with copper electrodes but increases with graphite electrodes (Figure 10). Further investigation is needed to explain this phenomenon.

5. Conclusions

Based on the evaluation of the experimental results, the following conclusions can be drawn regarding the electro discharge machining (EDM) of tool steels with copper and graphite electrodes:

- With increasing VDI grade, the material ratio (R_{mr}) of the roughness of the machined surfaces clearly decreases. In the range investigated, the most favourable values are achieved at VDI grade 18.
- The machined surfaces of the different tool steels did not show any significant differences in terms of the material ratio (R_{mr}). In the case of copper electrodes, outstanding properties can be achieved when EDM

40CrMnMo7 material, and in the case of graphite, the same can be said for C45U and 45NiCrMo16 steel.

- Increasing the VDI grade reduces the surface roughness kurtosis (R_{ku}) to a favourable value of 3. In this respect, the two types of electrode materials and the different tool steel grades did not show any significant differences.
- The change in skewness (R_{sk}) as a function of the VDI grade is not clear. It clearly increases when machining with a graphite electrode, while it decreases when using a copper electrode.
- The R_{sk} - R_{ku} topological maps created based on the tests partially confirmed the ranges described in the literature as characteristic of electro discharge machining. From this point of view, the most favourable data pairs were achieved on the surfaces of 40CrMnMoS8-6 steel with a copper electrode and 45NiCrMo16 steel with a graphite electrode

Our results prove that changes in VDI grades significantly determine the so-called functional parameters of the roughness of machined surfaces. It has become clear that it is not possible to accurately describe the nature of a surface using a single parameter, so it is necessary to use these functional parameters and their combinations (topographic maps). Further studies are needed to clearly determine the effect of VDI grades.

References: **1.** I. *Puertas – C.J. Luis – L. Alvarez*: Analysis of the influence of EDM parameters on surface quality, MRR and EW of WC–Co, Journal of Materials Processing Technology, Vol. 153–154, 10 November 2004, pp. 1026-1032 **2.** *S.H. Lee – X.P. Lee*: Study of the effect of machining parameters on the machining characteristics in electrical discharge machining of tungsten carbide, Journal of Materials Processing Technology, Vol.115 (2001), pp. 344-358 **3.** *D. Bańkowski – P. Młynarczyk:* Influence of EDM Process Parameters on the Surface Finish of Alnico Alloys. Materials (Basel). 2022, 15(20):727, doi: 10.3390/ma15207277. **4.** ISO 13565-2:1996 – Surface texture: Profile method — Surfaces having stratified functional properties **5.** *Zs. Maros – K. Kun-Bodnár*, Investigation of Electro Discharge Machining of Tool Steels Based on the Roughness of the Machined Surfaces, Cutting & Tools in Technological System, 2023, Edition 99 pp. 46-57 **6.** *R. Horváth – Á. Czifra – Á. Drégelyi-Kiss Ágota*, Effect of conventional and non-conventional tool geometries to skewness and kurtosis of surface roughness in case of fine turning of aluminum alloys with diamond tools, International Journal of Advanced Manufacturing Technology, 78:(1-4) pp. 297-304. (2015) **7.** *D.J. Whitehouse*: Handbook of surface metrology, Inside of Physics Publ., Bristol (1994), p. 944

Жолт Марош, Крістіна Кун-Боднар, Мішкольц, Угорщина

ДОСЛІДЖЕННЯ ПАРАМЕТРІВ ФУНКЦІОНАЛЬНОЇ ШОРСТКОСТІ ПОВЕРХНІ СТАЛЕВИХ ВИРОБІВ, ПІСЛЯ ЕЛЕКТРОРОЗРЯДНОЇ ОБРОБКИ

Анотація. *Якість поверхні, отримана електричною розрядною обробкою (EDM), сьогодні дозволяє використовувати ці поверхні безпосередньо як функціональні поверхні – часто без* *потреби у постобробці – наприклад, у виробництві пластикових інструментів для формування. Це підкреслює важливість оцінки якості поверхні не лише за традиційними параметрами амплітуди, а й через так звані параметри функціональної шорсткості. У цій статті представлено результати досліджень, у яких EDM-оброблені інструментальні сталі вивчалися з використанням параметрів функціональної поверхневої шорсткости. Такі параметри ефективно характеризують операційну поведінку та застосовність оброблених поверхонь. На основі оцінки експериментальних результатів можна зробити деякі висновки щодо електророзрядної обробки (EDM) інструментальної сталі за допомогою мідних і графітових електродів. Зі збільшенням класу VDI співвідношення матеріалу (*R_{mr}*) до шорсткості оброблених поверхонь явно зменшується. У дослідженому діапазоні найсприятливіші значення досягаються на рівні VDI 18. Оброблені поверхні різних інструментальних сталевих виробів не мали суттєвих відмінностей у співвідношенні матеріалів (*R_{mr}*). У випадку мідних електродів видатні властивості можна досягти при використанні матеріалу EDM 40CrMnMo7, а у випадку графіту те саме можна сказати про сталі C45U та 45NiCrMo16. Підвищення ступеня VDI знижує куртоз шорсткості поверхні (*R_{ku}*) до сприятливого значення 3. У цьому сенсі два типи матеріалів електродів і різні сорти інструментальної сталі не мали суттєвих відмінностей. Зміна косості (*R_{sk}*) як функція ступеня VDI залишається незрозумілою. Вона явно зростає при обробці графітовим електродом, тоді як зменшується при використанні мідного електрода. Топологічні карти *R_{sk}-R_{ku}*, створені на основі випробувань, частково підтвердили діапазони, описані в літературі як характерні для електророзрядної обробки. З цієї точки зору найбільш сприятливі пари даних були отримані на поверхнях сталі 40CrMnMoS8-6 з мідним електродом і сталі 45NiCrMo16 з графітовим електродом Наші результати доводять, що зміни ступенів VDI суттєво визначають так звані функціональні параметри шорсткості оброблених поверхонь. Стало зрозуміло, що неможливо точно описати природу поверхні одним параметром, тому необхідно використовувати ці функціональні параметри та їхні комбінації (топографічні карти). Потрібні подальші дослідження, щоб чітко визначити вплив оцінок VDI.*

Ключові слова: *електроерозійна обробка (EDM); текстура поверхні; параметри функціональної шорсткості; топологічна карта.*

ISSN 2078-7405 Cutting & Tools in Technological System, 2025, Edition 103

UDC 621.914.1 **doi: 10.20998/2078-7405.2025.103.08**

EFFECT OF CHANGING THE MILLING HEAD DIAMETER ON THE INHOMOGENEITY OF THE MACHINED SURFACE TOPOGRAPHY

Antal **Nagy** [0000-0001-6160-4973]

University of Miskolc, 3515, Miskolc - Egyetemváros, Hungary
antal.nagy@uni-miskolc.hu

Received: 09 November 2025/ Revised: 17 November 2025/ Accepted: 24 November 2025 / Published: 15 December 2025

Abstract. *The geometry of the tool and the workpiece plays a decisive role in the formation of the topography of a machined surface. Depending on the kinematic conditions of the machining process, they influence both the magnitude of surface roughness and the irregularity of the topography. This paper presents an investigation of the variation in topographical inhomogeneity resulting from changes in the tool diameter used in face milling. The results showed that increasing the diameter – while keeping all other parameters constant – significantly increased the values of amplitude and functional roughness parameters measured on the surface at the same measurement position. The decreasing trend of the values with increasing distance from the path of the tool axis was consistent, and its magnitude gradually diminished at measurement locations taken at greater distances. However, when the distance was expressed as a proportion of the tool diameter, the values exhibited similar degrees of variation.*

Keywords: *face milling; surface roughness; distribution of roughness; tool diameter.*

1. Introduction

The components of mechanical engineering products are manufactured with the required accuracy and surface quality so that they can meet the specified structural, functional, and other performance requirements throughout their intended service life [1]. One of the most common ways to achieve this is through machining. During the process, the tool penetrates the material of the workpiece and, while removing chips, generates new surface(s) [2]. The cutting edge(s) leave an imprint on the surface, the characteristics of which are fundamentally determined by the relative motions of the tool and the workpiece, the tool edge geometry, and the feed rate [3].

Face milling is most commonly applied for producing planar surfaces due to its high productivity and the good dimensional accuracy and surface quality achievable on the machined surface (e.g., IT8 dimensional accuracy [4] and R_a = 0.8 μm surface roughness [5]). For this reason, many researchers investigate the influence of machining parameters on surface quality. In the following, the influence of several factors on the surface roughness are presented.

The influence of cutting parameters (e.g., cutting speed, feed, depth of cut) on surface roughness has been widely investigated [6]. The roughness can be decreased with decreasing feed values. In most cases, it has the highest influence on the surface roughness, followed by the cutting speed and the depth of cut [7]. However, it was reported in a study where aluminum workpieces were milled, that the feed rate had less significant effect than the the axial depth of cut [8]. A decrease of 50% in R_a parameter value was achieved with the increase of the cutting speed but only to a certain extent; in the study [8] the further increase of the spindle speed from 4000 rpm – i.e., the increase of the cutting speed – deteriorated the roughness. The nose radius of the tool is an important factor in the reduce of roughness; an increase in the radius from 0.4 mm to 1.2 mm caused a 62% decrease in the R_a value measured on the machined Ti-alloy [9]. Tool edge angles also affect the resultant roughness values on the machined surface; the roughness can be significantly decreased with an increase in the helix angle – thus a decrease in the shock load and vibrations – and minimally with the decrease of the radial rake angle [8,10]. Moreover, other characteristics of the milling tool, e.g., tool edge preparation, rounding [11], and run-out [12] also have an impact on the surface roughness [6]. However, another geometric attribute of the milling cutter – namely its diameter – may also influence the measured surface roughness values, an aspect that has been little studied so far.

In industry, larger-diameter milling tools are commonly used, as they allow for higher material removal rates, shorter machining times, and more efficient machine utilization [13]. However, an increase in surface roughness can also be expected, as observed in steel workpieces [14], influenced by factors exerting opposing effects. Although larger-diameter tools provide greater stiffness, the increased cutting forces, deflections, vibrations, and thermal loads associated with them may adversely affect the characteristics of the surface topography [15].

Due to the tool–workpiece kinematic relationships in face milling, the roughness characteristics can vary significantly across different regions of the surface, resulting in an inhomogeneous topography [16,17]. This may influence the functional properties of the surface (and their variability). The origin of such variations in roughness lies in the changes in the geometry of the cutting marks (their height, width, shape, etc.) on profiles measured at different locations and in different directions on the surface, as illustrated in Figure 1.

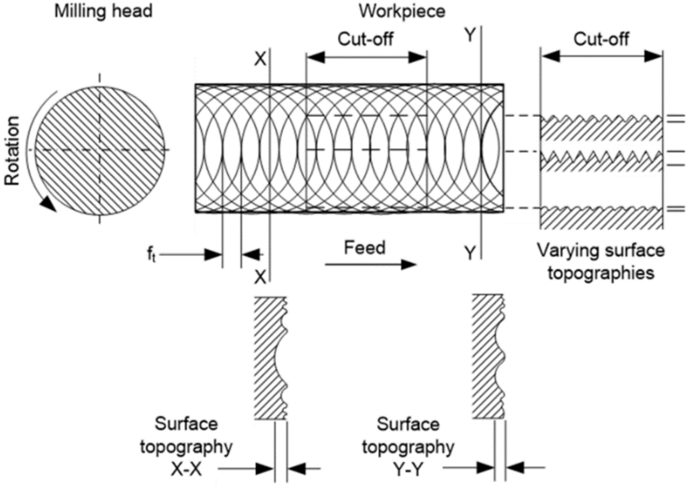

Figure 1 – Change in surface roughness with measurement direction in face milling [18]

The aim of the investigation is to experimentally determine how increasing the diameter of the milling tool affects the surface roughness and topographical inhomogeneity of a face-milled surface under identical cutting conditions.

2. Experimental conditions

For the investigation, machining experiments were carried out on a PerfectJet MCV-M8 vertical milling center. Three types of tools from Tungaloy's T2845 PM milling head series were used (050.05Z4, 063.05Z5W, and 100.05Z8). These tools share the same insert seat design and use the same mounted insert (OFEX 05T3AE, KH100 grade, $\kappa_r = 43°$, $\gamma_o = 25°$, $\alpha_o = 7°$, $r_\varepsilon = 0.4$ mm), but differ in their nominal diameters: $D_{t1} = 50$ mm (M50), $D_{t2} = 63$ mm (M63), and $D_{t3} = 100$ mm (M100). On three C45 steel workpieces, surfaces measuring 50 mm in length and 100 mm in width were prepared and machined under dry conditions. The set width of cut was equal to the tool diameter ($a_e = D_t$); 50 mm for the surface machined with the M50 tool, 63 mm for the one machined with the M63 tool, and 100 mm for the surface produced with the M100 tool. The additional cutting parameters were: $v_c = 300$ m/min, $a_p = 0{,}4$ mm, $f_z = 0.4$ mm/rev. The tool axis was positioned in the symmetry plane of the surfaces to be machined, perpendicular to them. During machining, the workpiece feed motion under the milling head continued from the start of cutting until the centers of the tool and the surface coincided, after which the tool was retracted from the cut. In this way, single milling marks were produced on the surfaces; however, unmachined areas remained within the width of cut, and double-cut surface regions were also formed during the back-cutting motion of the tool edge (Figure 2).

Roughness measurements on the machined surfaces were carried out using a CL2 confocal chromatic probe on an AltiSurf 520 three-dimensional surface topography measuring device. For examining roughness variations on the surfaces, several measurement points (marked with Roman numbers) were selected such that each of 5 defined measurement planes parallel to the feed direction, labeled **U**, **S** , and **D** (Fig. 2).

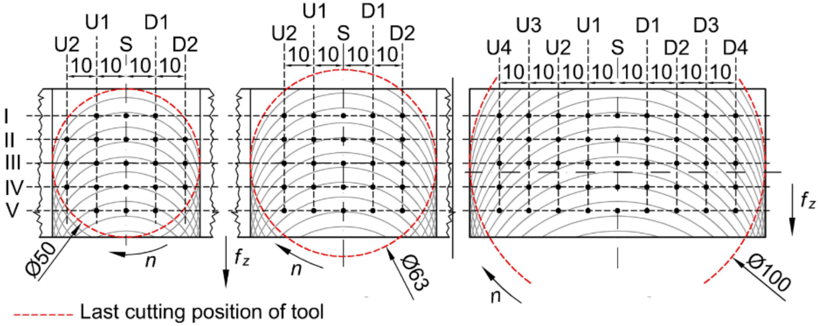

Figure 2 – Surfaces machined with tools of different diameters, along with the selected measurement planes and locations

The central plane corresponds to the path of the tool axis, which coincides with the symmetry plane of the surface. The others are positioned parallel to it, offset by 10 mm from one another on the up-milled (U planes) and down-milled (D planes) sides. Their number was determined according to the width of the milled surface (Figure 2). In the figure, the points indicate the centers of the measured profiles. The measurements were evaluated using AltiMap Premium v6.2 software. During measurement and evaluation, the requirements of the ISO 4287 standard were applied and followed. At each measurement location, profile measurements were taken in the feed direction with an evaluation length of 4 mm and a section length of 0.8 mm. No measurements were taken at positions that did not fall on the single cut region (i.e., those lying in unmachined or twice-machined areas, as shown in Figure 2).

3. Results and discussion

After measuring surface roughness at the designated measurement locations on the investigated surfaces (Figure 2), the roughness parameter values were evaluated. First, the roughness profiles measured at an identical location (**S-IV**) on each surface are shown in Figure 3. Second, the values of the most commonly used and examined roughness indicators – R_a (arithmetical mean roughness) and R_z (maximum height of the profile) – are presented and analyzed. In addition, based on our previous investigations, the values of the R_p (maximum profile peak height) and R_k (reduced core roughness depth) parameters – which express topographical inhomogeneity with the highest degree – are also provided and studied. These values are organized by measurement planes, locations, and parameter type in Tables 1–2. The tables also include the range of values measured within the planes and on the surface, the latter expressed as a ratio relative to the arithmetic mean of the values measured on the topography. The distribution of roughness values on each surface is illustrated using contour map diagrams in Figure 4. Due to the large differences observed when changing the tool diameter, the diagrams present values expressed as ratios relative to the mean, indicated with an overline above the index.

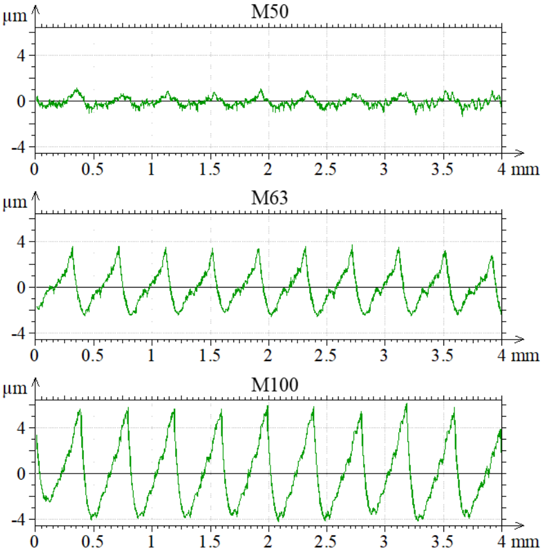

Figure 3 – Roughness profile curves recorded at position **S-IV** on surfaces machined with tools of different diameters

Table 1 – Measured R_a and R_z values and their variations on the studied surfaces

	R_a [µm]							R_z [µm]					
	I	**II**	**III**	**IV**	**V**	**Range**	**Plane**	**I**	**II**	**III**	**IV**	**V**	**Range**
Mille d		0.12	0.11	0.11		0.01	**D2**		0.48	0.49	0.51		0.03
	0.22	0.21	0.22	0.23	0.25	0.04	**D1**	1.04	0.99	1.05	1.08	1.02	0.09

	0.27	0.26	0.26	0.30	0.27	0.04	**S**	1.33	1.18	1.23	1.48	1.35	0.30
	0.22	0.22	0.21	0.22	0.21	0.01	**U1**	1.20	1.12	1.06	1.07	1.04	0.16
		0.10	0.12	0.11		0.02	**U2**		0.47	0.56	0.51		0.09
						101%	**Surface**						104%
Milled with M63	**I**	**II**	**III**	**IV**	**V**	**Range**	**Plane**	**I**	**II**	**III**	**IV**	**V**	**Range**
	0.83	0.88	0.89	0.91	0.89	0.08	**D2**	3.71	3.95	3.94	3.87	3.89	0.24
	1.12	1.11	1.11	1.11	1.12	0.01	**D1**	5.23	5.22	5.24	5.03	5.25	0.22
	1.24	1.25	1.25	1.22	1.22	0.03	**S**	5.86	5.98	5.97	5.83	5.82	0.16
	1.12	1.11	1.11	1.11	1.14	0.03	**U1**	5.37	5.42	5.13	5.23	5.20	0.29
	0.86	0.87	0.89	0.88	0.83	0.06	**U2**	3.86	3.89	3.81	3.81	3.81	0.08
						40%	**Surface**						47%
Milled with M100	**I**	**II**	**III**	**IV**	**V**	**Range**	**Plane**	**I**	**II**	**III**	**IV**	**V**	**Range**
	1.17	1.15	1.19	1.17	1.20	0.05	**D4**	4.76	4.63	4.75	4.98	4.81	0.35
	1.83	1.77	1.78	1.75	1.82	0.08	**D3**	7.12	6.85	7.06	6.77	7.12	0.35
	2.19	2.20	2.20	2.20	2.20	0.01	**D2**	8.51	8.75	8.78	8.63	8.70	0.27
	2.42	2.45	2.41	2.47	2.36	0.11	**D1**	9.61	9.82	9.60	9.76	9.29	0.53
	2.45	2.44	2.41	2.41	2.41	0.04	**S**	9.64	9.59	9.43	9.43	9.37	0.27
	2.44	2.45	2.42	2.41	2.40	0.05	**U1**	9.46	9.44	9.59	9.39	9.45	0.20
	2.22	2.20	2.22	2.22	2.18	0.04	**U2**	8.88	8.81	8.93	8.83	8.98	0.17
	1.83	1.85	1.81	1.79	1.79	0.06	**U3**	7.38	7.27	7.18	7.15	7.18	0.23
	1.20	1.20	1.22	1.18	1.21	0.04	**U4**	5.03	5.03	5.02	4.82	4.96	0.21
						67%	**Surface**						67%

First, the effect of tool diameter on surface roughness is presented. The measured roughness values increased significantly with increasing diameter. This is easily compared in the symmetry plane (**S**), where the theoretical topographies of the investigated surfaces show identical cutting mark characteristics due to the same tool–workpiece motions, tool edge position, and feed value. At the measurement locations in this plane, increasing the diameter from Ø50 mm to Ø63 mm resulted in a 3.8–5.1-fold increase in amplitude parameters and a 4.5–6.2-fold increase in R_{k}. Further increasing the tool size to Ø100 mm led to an additional 1.6–2-fold increase, nearly the same extent for the analyzed parameters. This effect is likely due to the improved rotational stability associated with the larger diameter, resulting in more regular shape of the tool marks and more favorable shearing of the workpiece material. At the same time, for the smallest-diameter milling tool, the noisy and poorly defined tool marks observed on the topography indicate that the smaller rotating mass – and consequently the weaker gyroscopic stabilizing effect – amplifies vibrations in the machine–tool–workpiece system (Figure 3). The mechanism of this effect requires further investigation.

Table 2 – Measured R_{p} and R_{k} values and their variations on the studied surfaces

№	R_{p} [μm]							R_{k} [μm]					
	I	**II**	**III**	**IV**	**V**	**Range**	**Plane**	**I**	**II**	**III**	**IV**	**V**	**Range**

		0.28	0.29	0.30		0.02	**D2**		0.32	0.29	0.28		0.04
	0.62	0.58	0.65	0.67	0.64	0.09	**D1**	0.69	0.59	0.65	0.66	0.65	0.10
	0.74	0.69	0.72	0.90	0.76	0.21	**S**	0.62	0.72	0.64	0.84	0.88	0.26
	0.72	0.70	0.63	0.63	0.59	0.13	**U1**	0.59	0.53	0.57	0.69	0.72	0.19
		0.30	0.34	0.33		0.04	**U2**		0.26	0.29	0.26		0.03
						108%	**Surface**						110%
Milled with M63	**I**	**II**	**III**	**IV**	**V**	**Range**	**Plane**	**I**	**II**	**III**	**IV**	**V**	**Range**
	2.01	2.18	2.07	2.10	2.10	0.17	**D2**	2.72	2.90	2.96	3.25	3.06	0.53
	2.97	2.94	2.91	2.85	2.93	0.12	**D1**	3.70	3.76	3.67	3.76	3.85	0.18
	3.43	3.53	3.52	3.45	3.46	0.10	**S**	3.86	3.99	3.95	3.76	3.85	0.23
	3.03	3.14	2.81	2.97	2.81	0.33	**U1**	3.55	3.61	3.70	3.62	3.92	0.37
	2.05	2.02	1.97	1.97	1.99	0.08	**U2**	2.80	2.67	2.91	2.86	2.52	0.39
						58%	**Surface**						43%
Milled with M100	**I**	**II**	**III**	**IV**	**V**	**Range**	**Plane**	**I**	**II**	**III**	**IV**	**V**	**Range**
	2.84	2.72	2.83	3.04	2.79	0.32	**D4**	3.00	2.98	2.84	2.96	3.09	0.25
	4.15	4.09	4.22	3.96	4.21	0.26	**D3**	5.12	4.64	4.65	4.69	4.97	0.48
	5.04	5.35	5.31	5.19	5.27	0.31	**D2**	5.66	5.65	5.83	5.71	5.49	0.34
	5.73	6.00	5.76	5.89	5.59	0.41	**D1**	6.67	6.24	6.43	6.46	5.96	0.71
	5.78	5.74	5.64	5.61	5.64	0.17	**S**	6.68	6.59	6.29	6.25	6.18	0.50
	5.76	5.72	5.89	5.70	5.71	0.19	**U1**	5.99	5.74	5.90	6.24	6.22	0.50
	5.51	5.41	5.53	5.40	5.58	0.18	**U2**	5.62	5.63	5.42	5.60	5.72	0.30
	4.58	4.46	4.50	4.38	4.47	0.20	**U3**	4.67	4.64	4.32	4.77	4.59	0.45
	3.09	3.09	3.15	2.95	3.01	0.20	**U4**	2.93	3.02	2.96	2.89	3.08	0.19
						70%	**Surface**						76%

Next, the variations in roughness values measured in the workpieces' symmetry plane (Figure 2, **S** plane) are analyzed. On the surfaces machined with the M63 and M100 tools, the values are nearly identical, differing by only 2–8%. In contrast, on the surface machined with the M50 tool, the differences are more pronounced: 15–28% for amplitude parameters and up to 35% for the functional parameter, due to the previously mentioned differences in rotational stability and vibrations (Tables 1–2). Within this plane, the values change randomly.

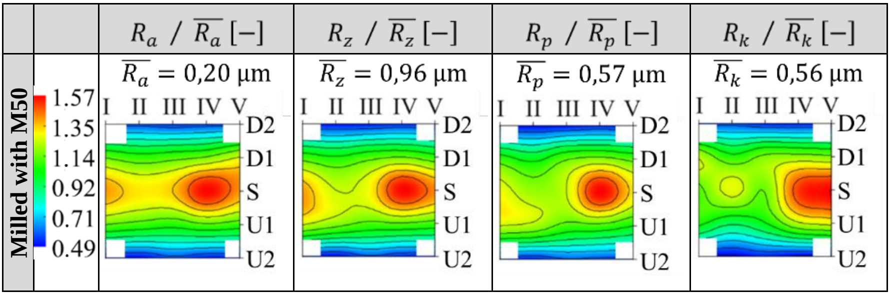

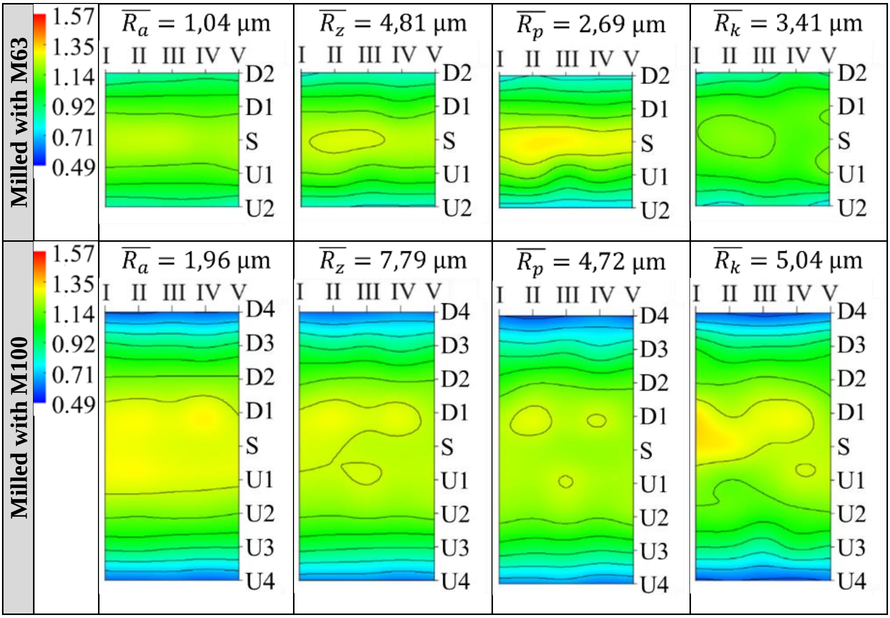

Figure 4 – Distribution of measured values on the investigated surfaces

In the following section, the variations in roughness values measured in the **U** and **D** planes – parallel to the **S** symmetry plane on the workpieces (Figure 2) – are analyzed. It can be observed that increasing the tool diameter reduced the differences in these planes for the investigated parameters (Tables 1–2). While the deviations on the surface machined with the M50 tool were mostly significant (5–28% for amplitude parameters, 11–35% for R_k), they were minor on the surface milled with the larger M63 tool (1–11% for R_a, R_z, and R_p; below 18% for R_k), and generally negligible on the surface cut with the M100 tool (ranging from 0.5–11%). The values within the planes – regardless of tool diameter – varies randomly. No trend was observed in the changes between the deviations determined in adjacent planes.

Next, the deviations and relative distributions of roughness values measured at the selected locations on the workpieces are evaluated as a function of tool diameter. The maximum differences in values determined on the investigated areas of the surfaces – the inhomogeneity of the topographies – were considerable but decreased with increasing tool diameter. On the surface machined with the M50 tool, deviations of 101–110% were reduced to 67–76% when the diameter was increased to Ø100 mm. Among the roughness parameters studied, the largest differences were observed for the R_k values.

Considering the distribution of roughness values on the topographies, it is identical that, for all tool diameters, the maximum values occur in the symmetry plane (Figure 4). The locations of the minimum values typically varied among the outer measurement planes farthest from the **S** plane, with negligible differences. On the surfaces, the values decreased with distance from the symmetry plane, by nearly the same degree on both the up- and the down-milled surface regions. Thus, the change in cutting movement direction has a negligible effect on the differences in values measured within the planes.

The changes in surface roughness values were further analyzed from two perspectives. For this purpose, the arithmetic mean of the measured values in the measurement planes was illustrated in Figure 5. First, considering a uniform-width area on the topographies (a 40 mm wide band between the **U2** and **D2** planes), increasing the tool diameter gradually reduced the deviations measured on the surface; machining with the M50 tool caused 101–110% variation, which was decreased to 4–19% when using the Ø100 mm diameter milling cutter. At the same time, in adjacent planes shifted by the same distance, the measured values decreased less with increasing tool diameter (i.e., in Figure 5a, the curves corresponding to larger diameters are less steep). This behavior can be explained as follows: for two selected measurement planes of identical width, on a surface machined with a larger-diameter tool, the span angle of the tool marks becomes smaller (Figure 2), so their height and radial width – the values of roughness parameters – differ less. On the other hand, when the ratio of the tool diameter to the distance of a parallel measurement plane from the symmetry plane remains constant (where the intersection angles of the tool marks are the same), the values are typically similar, differing by less than 20% (Figure 5b).

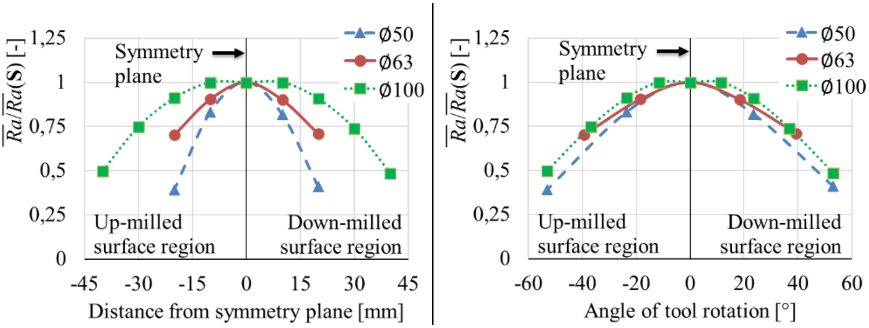

a, b,

Figure 5 – Ratio of the mean of R_a values measured in planes to the mean value in the symmetry plane on surfaces milled with cutters of different diameters as a function of the distance from the symmetry plane (a) and the rotation angle of the tool marks from it (b)

4. Conclusions

In this study, the effect of the cutter diameter on the roughness of face-milled surfaces, topographical inhomogeneity were investigated with the amplitude R_a, R_z, R_p and the functional R_k parameters. Three cutters of different nominal diameters (Ø50 mm, Ø63 mm, Ø100 mm), each equipped with the same type of insert, were analyzed. The main findings are summarized below.

- It was found that increasing the cutter diameter led to a significant increase in roughness values at identical measurement positions. Increasing the diameter from Ø50 mm to Ø63 mm resulted in a 3.8–6.2-fold increase in roughness in the workpiece symmetry plane, while a further increase to Ø100 mm caused an additional 1.6–2-fold increase.
- With increasing milling head diameter, the differences in roughness values measured in planes parallel to the feed direction decreased. While the range on the surface machined with the smallest tool was 15–28% for amplitude parameters and 11–35% for the functional parameter, the use of larger cutters reduced these differences to a similarly small extent, 1–11%.
- The range of values measured on the examined surfaces – the topographical inhomogeneity – decreased from 101–110% to 67–76% as the cutter diameter increased from Ø50 mm to Ø100 mm.
- It was observed that at points located at equal distances from the workpiece symmetry plane (in any direction), roughness values decreased progressively less with increasing milling tool diameter. For a distance of 20 mm, differences gradually reduced from 6–38% to 1–14%. However, when the distance from the symmetry plane was expressed relative to the cutter diameter, roughness values changed to a similar extent compared to the central plane, with a maximum difference of 20%.
- Among the analyzed roughness parameters, the functional R_k values exhibited the largest changes with increasing tool diameter.

References: **1.** *Youssef, H. A., El-Hofy, H. A., Ahmed, M. H.* Manufacturing Technology: Materials, Processes, and Equipment. Boca Raton, Oxon: CRC Press. 2024. **2.** *Mitsyk, A., Fedorovich, V., Grabchenko, A.* Main technological factors determining the efficiency and quality of the vibration process**.** *Cutting & Tools in Technological System.* 2022. vol. 96. pp. 131 – 137. **3.** *Felhö, C.* Investigation of surface roughness in machining by single and multi-point tools. Aachen: Shaker Verlag, 2014. 188 p. **4.** ISO 286-1: Geometrical product specifications (GPS) – ISO code system for tolerances on linear sizes. Part 1: Basis of tolerances, deviations and fits. 2010. **5.** *Whitehouse, D.J.* Handbook of Surface and Nanometrology. Boca Raton: CRC Press. 2011. **6.** *Abellán-Nebot, J. V., Vila Pastor, C., Siller, H. R.* A review of the factors influencing surface roughness in machining and their impact on sustainability. *Sustainability*. 2024. vol. 16(5). p. 1917. **7.** *Marakini, V., Pai, S. P., Bhat, U. K., Thakur, D. S., Achar, B. P.* High-speed face milling of AZ91 Mg alloy: Surface integrity investigations. International Journal of Lightweight Materials and Manufacture. 2022. vol. 5(4). pp. 528 – 542. **8.** *Bhirud, N. L., Dube, A. S., Patil, A. S., Bhole, K. S.* Multi-objective optimization of cutting parameters and helix angle for temperature rise and surface roughness using response surface methodology and desirability approach for

Al 7075. International Journal on Interactive Design and Manufacturing (IJIDeM). 2024. vol. *18*(10). pp. 7095 – 7114. **9.** *Shah, D., Bhavsar, S.* Effect of Tool Nose Radius and Machining Parameters on Cutting Force, Cutting Temperature and Surface Roughness-An Experimental Study of Ti-6Al-4V (ELI). Materials Today: Proceedings. 2020, vol. 22. pp. 1977 – 1986. **10.** *Chowdary, B. V., Sookhansingh, O.* Tool geometry and machining variables influence on the surface roughness of end-milling process: a comparative study with application of RSM and GA tools and techniques. International Journal of Process Management and Benchmarking. 2024. vol. 16(1). pp. 1 – 18. **11.** *Wang, B., Tang, M., Zhao, J., Song, C., He, S., Zhang, Q.* Effects of Cutting Edge Radius on the Surface Integrity of Milled Ti6Al4V Alloy. Journal of Materials Engineering and Performance. 2024. vol. 33(24). pp. 14001 – 14010. **12.** *Felhő, C., Kundrák, J.* Effects of setting errors (insert run-outs) on surface roughness in face milling when using circular inserts. Machines. 2018. vol. 6(2). p. 14. **13.** *Zaidi, S. R., Khan, M., Jaffery, S. H. I., Warsi, S. S.* Effect of machining parameters on surface roughness during milling operation. In Advances in Manufacturing Technology XXXIV (pp. 175 – 180). IOS Press. **14.** *Iswanto, I.* Effect of tool diameter and feeding speed on surface roughness in the AISI 1045 steel milling process. METAL: Jurnal Sistem Mekanik dan Termal. 2023. vol. 7(2). pp. 31 – 35. **15.** *Joshi, S. N., Bolar, G.* Influence of end mill geometry on milling force and surface integrity while machining low rigidity parts. Journal of The Institution of Engineers (India): Series C. 2021. vol. 102(6). pp. 1503 – 1511. **16.** *Nagy, A., Kundrak, J.* Changes in the values of roughness parameters on face-milled steel surface. Cutting & Tools in Technological System. 2020. vol. 92. pp. 85 – 95. **17.** *Nagy, A., Kundrak, J.* Roughness of Face-Milled Surface Topography in Directions Relative to the Feed Movement. Manufacturing Technology. 2024. vol. 24(2). pp. 241 – 254. **18.** *Smith, G.T.* Cutting Tool Technology: Industrial Handbook. London: Springer-Verlag, 2008. 559 p.

Антал Надь, Мішкольц, Угорщина

ВПЛИВ ЗМІНИ ДІАМЕТРА ФРЕЗЕРНОЇ ГОЛОВКИ НА НЕОДНОРІДНІСТЬ ОБРОБЛЕНОЇ ПОВЕРХНІ

Анотація. *Геометрія інструменту та заготовки відіграє вирішальну роль у формуванні топографії обробленої поверхні. Залежно від кінематичних умов процесу обробки, вони впливають як на величину шорсткості поверхні, так і на нерівність топографії. У цій статті розглядається дослідження варіації неоднорідності топографії, що виникають через зміни діаметра інструмента, що використовується для фрезерування. Результати показали, що збільшення діаметра — при збереженні всіх інших параметрів незмінними — значно підвищує значення параметрів амплітуди та функціональної шорсткості, виміряних на поверхні в тій самій позиції вимірювання. Тенденція до зменшення значень із збільшенням відстані від траєкторії осі інструменту була стабільною, а її величина поступово зменшувалася на місцях вимірювання, зроблених на більших відстанях. Однак, коли відстань виражалася як пропорція діаметра інструмента, значення мали схожі ступені варіацій. Було встановлено, що збільшення діаметра фрези призводило до значного збільшення значень шорсткості в однакових положеннях вимірювання. Збільшення діаметра з Ø50 мм до Ø63 мм призвело до збільшення шорсткості площини симетрії заготовки у 3,8–6,2 рази, а подальше збільшення до Ø100 мм — додаткове збільшення у 1,6–2 рази. Зі збільшенням діаметра фрезерної головки різниця в значеннях шорсткості, виміряних у площинах, паралельних напрямку подачі, зменшувалася. Хоча діапазон поверхні, обробленої найменшим інструментом, становив 15–28% для параметрів амплітуди і 11–35% для функціонального параметра, використання більших різців зменшувало ці відмінності до подібно невеликої міри — 1–11%. Діапазон значень, виміряних на досліджуваних поверхнях — топографічна неоднорідність — зменшився з 101–110% до 67–76% у міру збільшення діаметра фрези з Ø50 мм до Ø100 мм. Було помічено, що в точках, розташованих на однакових відстанях від площини симетрії заготовки (у будь-якому напрямку), значення шорсткості поступово зменшувалися зі збільшенням діаметра фрезерного інструмента. На відстані 20 мм різниця* *поступово зменшувалася з 6–38% до 1–14%. Однак, коли відстань від площини симетрії виражалася відносно діаметра різального інструменту, значення шорсткості змінювалися порівняно з центральною площиною, з максимальною різницею 20%. Серед проаналізованих параметрів шорсткості функціональні значення* R_k *показали найбільші зміни при збільшенні діаметра інструмента.*

Ключові слова: *торцеве фрезерування; шорсткість поверхні; розподіл шорсткості; діаметр інструменту*.

UDC 621.9 **doi: 10.20998/2078-7405.2025.103.09**

IMPROVING THE EFFICIENCY OF TOOLS FOR TURNING HIGH-STRENGTH MATERIALS

Viktor **Kovalov** [0000-0001-5091-5856], Galyna **Klymenko** [0000-0002-1022-6324], Yana **Vasylchenko** [0000-0002-4566-8827], Maksym **Shapovalov** [0000-0002-8039-8834], Roman **Boroday** [0009-0009-6730-9540], Yehor **Zakharov** [0009-0002-1320-5825]

Donbass State Engineering Academy (DSEA), Kramatorsk, Ukraine
wasilchenko.ua@gmail.com

Received: 19 November 2025/ Revised: 25 November 2025/ Accepted: 29 November 2025 / Published: 15 December 2025

Abstract. *The article presents the results of a comprehensive study of heavy turning of high-strength steels used in structural components of defense and energy engineering, particularly in the tyres and rims of railway wheelsets. The aim of the work is to improve the efficiency of cutting tools by optimizing their geometry and cutting parameters based on the analysis of thermomechanical loading, the stress–strain state of the cutting wedge, and the regularities of tool wear development. The study includes modeling of temperature fields and contact stresses, analysis of the action of elementary force components on the rake and flank surfaces of the tool, as well as experimental determination of cutting forces, wear, and surface roughness during turning of steels with hardness of 2850–3600 MPa. The obtained results show that the geometry of the cutting part is a critical factor in ensuring tool stability: the use of a shortened rake face, strengthening chamfers, and a rational nose radius reduces contact stresses and local overheating in the tool-nose zone. Optimal cutting conditions (V = 45–55 m/min, s = 1.4–2.0 mm/rev, t = 6–8 mm) were established, ensuring minimal wear intensity and a stable chip-formation process. The practical significance of the work lies in the possibility of increasing tool life, machining accuracy, and technological reliability in the production of high-responsibility components from high-strength steels.*

Keywords: *heavy turning; high-strength steels; wheelsets; cutting tool; tool geometry; thermomechanical stresses; cutting temperature; wear; tool life.*

1. Introduction

Machining steel workpieces under heavy cutting conditions is one of the most complex and resource-intensive operations in mechanical engineering, particularly during the processing of large components such as railway wheelsets or rolling mill rolls. The combination of large depths of cut, high feed rates, and increased hardness of the surface layer leads to intensive tool wear, an increase in cutting forces, and significant thermomechanical loading on the cutting edge. Under such conditions, traditional approaches to improving tool life—use of cutting fluids, wear-resistant coatings, or preheating of the workpiece—lose their effectiveness due to the sharp rise in temperature on the rake and flank surfaces. This causes plastic deformation of the carbide layer, reduces its shape stability, and decreases tool life by a factor of 2–3 compared to standard cutting conditions.

The need to reduce wear intensity and maintain geometric stability of the cutting edge has made the optimization of tool geometry a highly relevant task. It has been established that the formation of the temperature-stress state is largely determined by the rake and clearance angles, the nose radius, the configuration of micro-chamfers, and the parameters of chip–tool contact. Optimizing these elements makes it possible to reduce the temperature in the cutting zone, stabilize the chip-formation process, and minimize plastic deformation even under conditions of large undeformed chip thickness.

The aim of this work is to increase the efficiency of heavy turning of alloy steels by determining rational cutting regimes and optimizing tool geometry under conditions of intensive thermomechanical loading. This involves experimental investigation of the influence of cutting speed, feed, depth of cut, rake and clearance angles, and nose radius on tool wear, chip-formation stability, and surface quality, followed by justification of geometric parameters that ensure minimal wear at high productivity.

2. Analysis of Research and Problem Statement

Increasing requirements for the strength and service life of wheelset components in modern transport and energy engineering have intensified research aimed at improving the efficiency of heavy turning of high-strength and hardened steels. A significant body of work focuses on the analysis of temperature fields, cutting forces, and tool wear mechanisms, as elevated temperatures and intensive thermomechanical processes determine both chip formation and the degradation rate of the cutting edge [1–3]. The studies by Duc et al. [1] and Mane et al. [2] present experimental and FEM-based temperature models for machining high-strength steels, showing the influence of cutting speed, tool geometry, and cooling conditions. Work [3] highlights temperature and residual stress characteristics during machining of hardened AISI 52100 steel, confirming the complex thermal loading relevant to railway wheelset bandages as well. Studies by Zheng et al. [4] and Zhang et al. [5] emphasize the critical role of high temperatures in wear mechanisms of coated inserts under heavy mechanical loads.

Further research focuses on modelling thermal and mechanical processes within the cutting tool. Work [6] demonstrates the effectiveness of protective coatings in reducing local overheating, while Twardowski et al. [7] highlight the potential of predicting tool wear based on temperature and force parameters. The findings of Krbata et al. [8] provide insight into tribological interactions between tool materials and hard workpiece materials, which is relevant for machining hardened wheelset bandages. In parallel, intelligent wear-prediction methods are actively developing: neural-network-based models presented in the works of Guan et al. [9] and Cheng et al. [10] show high accuracy in predicting tool degradation during high-speed machining of high-strength steels.

Considerable attention is also devoted to optimizing cutting parameters. Bhemuni et al. [11] investigated the relationship between cutting conditions and temperature in the cutting zone, while work [12] offers optimal machining parameters for AISI 52100 steel considering surface roughness and cutting forces. Review articles by Shihab et al. [13] and Sivaram et al. [14] summarize recent trends in hard turning technologies, and study [15] examines the influence of cooling-lubrication conditions on the surface quality of AISI 52100 steel.

A synthesis of the literature shows that despite substantial progress in hard-turning research, significant gaps remain for the machining of steel bandages and wheelset rims. Notably, there is a lack of models capable of correctly accounting for plastic deformation of the tool tip under large stock allowances and elevated thermo-mechanical loads characteristic of heavy turning. Moreover, available data on the stress–strain state of the cutting wedge under real industrial loading conditions remain limited.

3. Object, Subject, and Research Methodology

The object of the study is the turning process of high-strength structural steels under heavy thermomechanical loading of the cutting tool. The subject of the research includes the tool materials of carbide inserts, the geometry of cutting tools, the temperature–force loads in the contact zone, the shear stresses on the rake and flank surfaces of the tool, and the wear mechanisms of the cutting wedge during machining of large stock allowances.

The research methodology is based on the combination of theoretical modelling and experimental verification. To determine the temperature on the rake and flank surfaces of the tool, a thermomechanical model was applied, accounting for heat generation due to plastic deformation in the cutting zone and friction on the contact surfaces. The average temperature was calculated considering the main technological parameters according to the generalized dependence:

$$T=f(V,s,t,\gamma,\alpha,r_{\varepsilon}),$$

where V — cutting speed, S — feed, t — depth of cut, γ — rake and clearance angles, $r_{\varepsilon r}$ — tool nose radius.

This approach makes it possible to determine heat distribution in the cutting zone and assess the conditions of local overheating, which significantly influence tool wear resistance.

To evaluate the stress state of the cutting wedge, a modified Mitchell method was used, allowing calculation of the maximum shear stresses on the rake surface through the frictional component of cutting force:

$$\tau_{\text{мах}} = \frac{F_c}{A_F}$$

F_c — component of the cutting force associated with friction, A_f— actual contact area between the chip and the rake surface.

The obtained relationships reflect the influence of chip thickness and wear-land width on the growth of shear stresses, which determines the intensity of plastic deformation of the cutting wedge.

Tool wear was analyzed by determining the wear intensity, introduced as the derivative of the wear-land width with respect to the cutting path:

$$I = \frac{dh}{dL},$$

where h — wear-land width, L — cutting path.

Using wear intensity makes it possible to characterize tool degradation not only in the steady-state stage but also at initial and transitional phases, which is particularly important when machining high-strength steels with non-uniform heat generation in the cutting zone.

Experimental investigations were performed to determine the evolution of cutting forces, thermomechanical loading, and wear intensity of the cutting tool during heavy turning of hardened and high-carbon steels. The tests were carried out on a heavy lathe model KZh1832, which provides the required stiffness of the technological system, stable feed, and the capability to machine large stock allowances under elevated loads (Fig. 1).

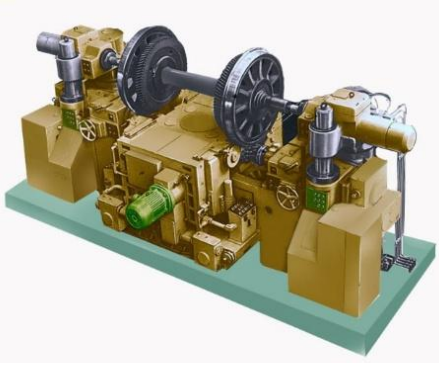

Figure 1 - Heavy-duty lathe model KZh1832 (manufactured by the Kramatorsk Heavy Machine Tool Plant)

For the experimental investigations, heat-treated specimens of steel grade 60—typical for railway wheel-set tyres—were used. The tool geometry was varied by adjusting the rake angle γ, clearance angle α, and nose radius rε, while ensuring identical microgeometry of the cutting edge. Cutting parameters were changed within the range typical for heavy turning according to a factorial experimental design, which made it possible to evaluate both the individual influence of each factor and their interactions.

Cutting forces were measured using a strain-gauge system equipped with a dynamometer, allowing the registration of tangential, radial, and axial components. The temperature in the cutting zone was monitored using a thermoelectric method. Tool wear was assessed optically by measuring the width of the flank wear land and identifying signs of edge degradation or loss of shape stability.

The obtained data were subjected to statistical processing. Based on variations in cutting forces, temperature, and wear intensity, rational cutting regimes and optimal geometric parameters of the cutting insert were determined for operating under elevated thermomechanical loading conditions.

4. Theoretical Principles of Tool Geometry Optimization for Machining High-Strength Steels

4.1. Modelling of Temperature in the Cutting Zone

Accurate prediction of temperature in the cutting zone is fundamental for the optimization of cutting tool geometry when machining high-strength steels, where the thermal load often approaches the heat-resistance limits of carbide materials. The thermal processes are described by the equations of non-stationary heat conduction, which consider the heat generated by plastic deformation of the removed layer as well as friction on the contact surfaces.

An important criterion characterizing the ratio between heat conducted into the chip and into the tool is the Péclet number:

$$\mathrm{Pe} = \frac{Vt}{a},$$

where

V — cutting speed, t — characteristic chip thickness, a — thermal diffusivity of the workpiece material.

At low Pe values, most of the heat flows into the tool, while at high Pe the primary heat flow is carried away by the chip, fundamentally influencing the temperature fields on the contact surfaces.

The general thermal balance is expressed as:

$$q=q_p+q_{fr},$$

where

q_p — heat generated by plastic deformation of the material,
q_{fr} — heat generated by friction between the chip and the tool rake face.

The subsequent distribution of heat is determined by its partition into the chip (η_c), tool (η_t) and workpiece (η_w):

$$\eta_c+\eta_t+\eta_w=1.$$

The maximum temperature on the rake face is estimated as:

$$T_{max} = T_o \frac{ql}{kA},$$

where

T_0 — initial temperature of the tool, l — chip–tool contact length, k — thermal conductivity of the tool material, A — contact area.

The geometry of the cutting part significantly affects the resulting temperature fields. Increasing the rake angle γ reduces the real contact area and lowers peak temperatures, although excessive γ decreases wedge strength. Chamfers on the rake face help stabilize chip deformation and redistribute the thermal load. The nose radius $r_{\varepsilon r}$ affects heating on the flank face and the overall mechanical stability of the cutting edge: a larger radius increases strength but also enlarges the contact zone, raising frictional heating.

4.2. Stress State and Deformation of the Cutting Edge

Evaluation of the stress–strain state of the cutting edge is a key stage in the analysis of heavy turning of high-strength steels, since the distribution of normal and tangential stresses directly determines tool durability, wear intensity, and the accuracy of surface formation. Under large feeds and depths of cut, the cutting wedge experiences significant thermo-mechanical loading, which leads to local stress concentrations on the rake-land facet and the flank surface, particularly in the tool-tip zone where the maximum wear land width is formed and peak heating occurs (fig 2).

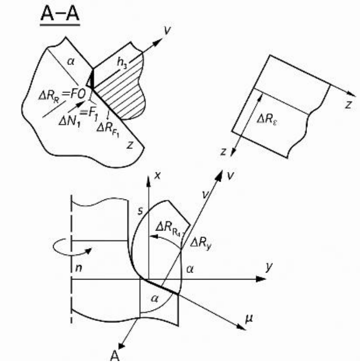

Figure 2 - Scheme of the stress state of the cutting wedge during machining of high-strength steel

In the stress–strain model of the cutting tool, individual sections of the working surfaces are considered as being subjected to elemental force components. On the rake face, within the chip–tool contact zone, an elemental tangential component ΔF_1, a normal component ΔN_1, and the resultant force component ΔR_ξ directed along the chip flow line act simultaneously. For the clearance face, where a stagnation zone is formed, a uniformly distributed normal pressure q_N is introduced, representing the contact load on the wear land.

An important element of the model is the description of the cutting edge shape in local coordinates (ξ, z), which reflects the real geometry of the edge radius and the rake chamfer. According to the geometric relations for the radius portion of the cutting edge, the coordinates of an arc element are defined as:

$$x^2+y^2=r_\varepsilon^2,\ dl = \frac{r_\varepsilon}{\sqrt{r_\varepsilon^2-x^2}}dx.$$

The elemental increment of the tangential cutting-force component is expressed as:

$$dP_y = K_V S b \frac{x}{\sqrt{r_\varepsilon^2-x^2}} dx q_N f_y sin\gamma dx + \sigma_r b h_3 dx,$$

where: K_V — coefficient accounting for the workpiece material properties, S — feed, b — contact width, q_N — normal stresses on the wear land, $h_з$ — wear-land thickness, f_y — friction coefficients, γ — rake angle.

Similarly, for the axial and radial force components:

$$dP_x = K_V S b \frac{x}{\sqrt{r_\varepsilon^2-x^2}} dx q_N f_x sin\gamma dx + \sigma_r b h_3 dx, dP_z = K_V S b \frac{x}{\sqrt{r_\varepsilon^2-x^2}} dx q_N f_z sin\gamma dx,$$

The integration limits are determined by the cutting-edge contact length:

$$x \in \left[0, \sqrt{2r_\varepsilon t - t^2}\right]$$

where t is the chip thickness.

Thus, the total components of the cutting force are obtained by integrating the corresponding differential expressions:

$$P_x = \int dP_x,\ P_y = \int dP_y,\ P_z = \int dP_z.$$

These components are then transformed into the global coordinate system (Fig. 2), enabling determination of the resultant load acting on the cutting wedge:

$$\vec{R} = P_x, P_y, P_z,$$

Additionally, using Mitchell's solution for a wedge, the shear stresses in the tool cross-section are defined as:

$$\tau_m = \frac{P_x}{be}\frac{\tan\frac{\beta}{2}}{\cos\frac{\beta}{2}},$$

where β is the wedge angle, e is the cross-sectional thickness, b is the contact width.

An increase in the wedge angle β reduces τm, confirming a lower tendency toward plastic deformation as the wedge strength increases — a typical effect for tools with a shortened rake face.

The generalized analysis shows that maximum stresses are concentrated in the edge-radius zone, where peak thermal and mechanical loads occur simultaneously. This region becomes the initiation point of intensive wear and formation of the wear land $h_{з}$, which is confirmed by experimental results and agrees with the modelling outcomes.

4.3. Wear Intensity Model

The functional efficiency of a cutting tool during the machining of high-strength steels is determined by the regularities of wear development on the cutting wedge and its ability to maintain geometric parameters under increased thermomechanical loading. To quantify this process, a wear-intensity model is used, which assumes division of the contact zone into local regions, each characterized by its own rate of cutting-edge degradation.

The local wear intensity at a point with coordinate x along the cutting edge is expressed as:

$$I(\mathrm{x}) = \frac{dh(\mathrm{x})}{dL},$$

where *h(x)* is the local wear value (micro-chipping depth or flank-wear width), *L* is the cutting path.

The highest values of *I(x)* are observed in the tool-nose region, where maximum shear stresses, workpiece-induced pressure, and localized temperature peaks coincide (Fig. 3).

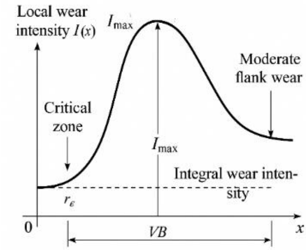

Figure 3 - Diagram of the local and integral wear intensity of the cutting edge

The boundary conditions for edge shape stability are defined as:

$$T_{max} < T_f,\ \sigma_{eq} < \sigma_p,$$

where T_f is the temperature at which the hard alloy begins to soften, σ_p is the strength limit or the conventional yield strength of the tool material.

Exceeding these parameters leads to a loss of geometric stability of the cutting wedge, accelerated wear, and the onset of plastic deformation in the tool tip.

The integral wear intensity is defined as the average degradation rate of the cutting edge:

$$I_{int} = \frac{1}{L}\int_0^L I(x)dx,$$

which makes it possible to evaluate the tool life and determine the cutting length at which the critical wear value VB_{crit} is reached.

5. Optimization of Tool Geometry for Machining High-Strength Materials on Heavy Turning Machines

Studies of thermomechanical loading during turning of steel wheel-set tyres and rims have shown that the geometry of the cutting part has a decisive influence on cutting forces, stress localization in the edge zone, and tool wear rate. For steels with hardness HB 2850–3600 MPa, the maximum loads are concentrated at the tool nose, where peak temperatures and the largest wear-land width are formed. For standard prismatic inserts, the vertical cutting-force component ***Pz*** reaches 40–45 k_N, which leads to accelerated tool degradation.

Comparison of different geometries demonstrated the advantages of inserts with a shortened rake surface: a reduced rake angle on the chamfer increases wedge strength, while a larger inclination of the main rake surface stabilizes chip formation.

Such tools promote a more uniform distribution of normal stresses and reduce peak shear stresses in the nose region. Radius inserts with ***r*** **=** 4–14 mm also effectively decrease local loads in the transition zone, provided that the clearance angle is corrected to prevent backside overheating.

Analysis of cutting forces showed that at ***t*** **=** 8 mm and feed 1.2–1.6 mm/rev, the Pz component increases by 20–25 %, accelerating wear-land development. This confirms the need to limit feed in rough turning of wheel-set tyres.

The optimal tool parameters were found to be: rake angle 12–14°**,** clearance angle 4–6°, nose radius 1.2–1.6 mm for tyres and 4–6 mm for rims. This geometry reduces shear stresses $\boldsymbol{\tau_m}$ by 15–20 % and stabilizes the stress state of the cutting wedge. Combined with rational cutting regimes (V = 45–55 m/min, S = 1.4–2.0 mm/rev, t = 6–8 mm), tool life increases by 25–30 %**.**

A rationalized tool geometry includes the use of strengthening chamfers, adaptive selection of nose radius depending on operation type, adjustment of rake angle according to tyre hardness, and minimization of the real chip-contact zone to reduce thermal loading. This approach ensures improved tool life and stable profile formation under heavy-duty machining of high-strength steels.

6. Experimental investigations

Experimental studies were carried out to verify the adequacy of the analytical models and to determine the influence of cutting tool geometry on tool life and machining quality when turning high-strength steels under heavy-duty conditions. Cutting force measurements showed that the tangential component of the cutting force Fc increases almost linearly with feed rate, which corresponds to the regularities of chip thickness formation in heavy turning. The characteristic form of this dependence is shown in Fig. 3.

As the feed increased from 1.2 to 2.5 mm/rev, the cutting force rose by approximately 25–30 %, confirming the dominance of mechanical loading over thermal effects within the tested cutting-speed range. An increased nose radius contributed to a reduction of peak stresses in the tool-tip zone, which is consistent with the analytical stress model.

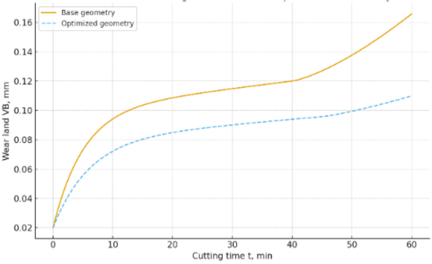

Figure 4 - Comparison of wear intensity for the baseline and optimized tool geometry

The wear of the cutting tool during heavy turning followed a three-stage pattern: rapid initial break-in, steady uniform wear, and a sharp acceleration before the catastrophic stage (Fig. 4). At the beginning, wear intensity was maximal due to micro-geometric adaptation; this was followed by an almost linear increase in flank wear VB under stable thermal conditions, and after 40–45 minutes a rapid rise in wear occurred as a result of local plastic deformation of the cutting edge and increasing temperature on the flank surface.

A comparison of the baseline and optimized geometries showed that modifying the rake angle, clearance angle, and nose radius significantly influences the degradation of the cutting edge. The optimized geometry provided a 20–35% reduction in wear intensity, delayed the onset of the catastrophic stage, and resulted in lower temperatures in the tool-tip region, which agrees with the modelling results.

Surface roughness analysis confirmed an improvement to Ra = 2.4–3.8 μm (20–30% better than the baseline tool), which is associated with reduced plastic deformation of the tool tip and lower equivalent stresses. Based on the overall results, the optimal heavy-turning cutting conditions were identified as: cutting speed 45–55 m/min, feed rate 1.4–2.0 mm/rev, depth of cut 6–8 mm, with rake angle 12–16°, clearance angle 4–6°, and nose radius 8–10 mm. These parameters ensure minimal wear intensity, stable mechanical and thermal loads, and high tool life when machining high-strength steels on heavy lathes.

7. Conclusions

The study presents a comprehensive investigation of heavy turning processes applied to high-strength and hardened steels, combining thermomechanical modelling, analysis of the stress–strain state of the cutting wedge, construction of a wear-intensity model, and experimental verification on a heavy lathe. It is shown that an accurate assessment of tool shape stability is possible only when temperature, force, and contact phenomena are considered simultaneously, as these factors govern the behaviour of the cutting edge under large depths of cut, increased feed rates, and variable hardness of the surface layer.

Thermomechanical modelling established the critical influence of the rake and clearance angles, nose radius, and the configuration of strengthening chamfers on the distribution of heat fluxes and the location of maximum temperatures. It was demonstrated that optimization of these parameters reduces local overheating at the tool nose and delays the onset of intensive wear. Analysis of the stress state using a modified Mitchell approach confirmed that tools with a shortened rake face and a properly selected nose radius reduce peak shear stresses and ensure a more uniform distribution of normal stresses on contact surfaces, thereby lowering the risk of plastic deformation and edge chipping.

The wear-intensity model made it possible to quantitatively describe the development of edge degradation and confirmed the critical role of the nose region in the formation of the wear land. Experimental studies during the turning of steels used for wheel-set tyres and rims demonstrated reductions in cutting forces, slower wear progression, and improved machining accuracy when optimized tool geometry was applied.

The generalised results enabled the formulation of recommendations: the use of strengthening chamfers, adaptation of the nose radius to the type of operation, correlation of the rake angle with material hardness, and minimisation of the real chip–tool contact zone. The optimized solutions enhance tool life, stabilise the cutting process, and improve surface quality when machining large, high-strength steel components.

References: **1.** *Pham Minh Duc P., Giang L.H., Nguyen V.T.* Analyzing Cutting Temperature in Hard-Turning Technique with Standard Inserts Through Both Simulation and Experimental Investigations. Applied Sciences, 2025, 15(2), 983. DOI: 10.3390/app15020983 **2**. *Mane S., Patil R.B., Kolhe M.L., Siddiqui M.I.H., Chan C.K., Xu Y.* Analysis of Thermal Aspect in Hard Turning of AISI 52100 Alloy Steel Under Minimal Cutting Fluid Environment Using FEM. Applied Mechanics, 2025, 6(2), 26. DOI: 10.3390/applmech6020026 **3**. *Mane S., Patil R.B., Siddiqui M.I.H., et al*. Effect of Cutting Parameters and Tool Coating on Residual Stress and Cutting Temperature in Dry Hard Turning of AISI 52100 Steel Using Finite Element Method. Frontiers in Materials, 2025. DOI: 10.3389/fmats.2025.1613630 **4**. *Zheng G., Li L., Li Z., Gao J., Niu Z.* Wear Mechanisms of Coated Tools in High-Speed Hard Turning of High Strength Steel. International Journal of Advanced Manufacturing Technology, 2018. DOI: 10.1007/s00170-017-1132-1 **5**. *Zhang H.P., Sutanto B., To S.* Tool Wear in High-Speed Turning Ultra-High Strength Steel Under Dry and CMQL Conditions. Materials and Manufacturing Processes, 2020. DOI: 10.1080/10584587.2020.1728633 **6**. *Hao G., Tang A., Zhang Z., et al*. Finite Element Simulation of Orthogonal Cutting of H13-Hardened Steel to Evaluate the Influence of Coatings on Cutting Temperature. Coatings, 2024, 14(3), 293. DOI: 10.3390/coatings14030293 **7**. *Twardowski P., Wiciak-Pikuła M*. Prediction of Tool Wear Using Artificial Neural Networks During Turning of Hardened Steel. Materials, 2019, 12(19), 3091. DOI: 10.3390/ma12193091 **8**. *Krbata M., Eckert M., Majerik J., Barenyi I.* Wear Behaviour of High Strength Tool Steel 90MnCrV8 in Contact with Si_3N_4. Metals, 2020, 10(6), 756. DOI: 10.3390/met10060756 **9**. *Guan R., Cheng Y., Jin Y., et al*. Tool Wear Prediction for Milling High Strength Steel Based on DenseNet-ResNet-GRU. Journal of Mechanical Science and Technology, 2024, 38, 3585–3596. DOI: 10.1007/s12206-024-0632-9 **10**. *Cheng M., Kim S., Zhao Y., et al*. Intelligent Prediction Model of the Tool Wear Based on Machine Learning Technique in Turning of High-Strength Steel. Proceedings of the IMechE Part B: Journal of Engineering Manufacture, 2020. DOI: 10.1177/0954405420935787 **11**. *Bhemuni V., Chelamalasetti S., Kondapalli S.* Effect of Machining Parameters on Tool Wear and Nodal Temperature in Hard Turning of AISI D3 Steel. Open Access Library Journal, 2014. DOI: 10.4236/oalib.1100627 **12.** *Umamaheswarrao P., Venkata Rao P., Srinivasa Rao M.* Achieving Optimal Process Parameters During Hard Turning of AISI 52100 Steel. Key Engineering Materials, 2019, Vol. 818, pp. 87–95. DOI: 10.4028/www.scientific.net/KEM.818.87 **13**. *Shihab S.K., Khan Z.A., Mohammad A., Siddiquee A.N.* A Review of Turning of Hard Steels Used in Bearing and Automotive Applications. Production & Manufacturing Research, 2014, 2(1), 24–49. DOI: 10.1080/21693277.2014.881728 **14**. *Sivaram N.S., Prakash S.* Recent Developments in Turning Hardened Steels – A Review. IOP Conference Series: Materials Science and Engineering, 2017, 197, 012009. DOI: 10.1088/1757-899X/197/1/012009 **15**. *Rao R., Alluru V., Kumar J.* Surface Integrity of

AISI 52100 Steel During Hard Turning Under Various Cooling/Lubrication Strategies. Advances in Materials Science and Engineering, 2020, Article ID 4256308. DOI: 10.1155/2020/4256308

Віктор Ковальов, Галина Клименко, Яна Васильченко,
Максим Шаповалов, Роман Бородай, Єгор Захаров
Краматорськ, Україна

ПІДВИЩЕННЯ ЕФЕКТИВНОСТІ ІНСТРУМЕНТІВ ДЛЯ ТОКАРНОЇ ОБРОБКИ ВИРОБІВ З ВИСОКОМІЦНИХ МАТЕРІАЛІВ

Анотація *У статті представлено результати дослідження процесів важкого точіння високоміцних та загартованих сталей, що застосовуються у конструктивних елементах відповідального призначення в транспортному, оборонному й енергетичному машинобудуванні. Робота спрямована на підвищення ефективності різального інструмента шляхом оптимізації його геометрії та режимів різання з урахуванням дії інтенсивних термомеханічних навантажень, характерних для обробки великих припусків і матеріалів з підвищеною твердістю. У межах дослідження виконано моделювання температурних полів, розподілу контактних напружень, силових взаємодій у зоні різання, а також формування локальних пікових температур, що визначають розвиток пластичної деформації різального клина та зростання інтенсивності зношування. Експериментальні випробування, проведені при точінні сталей твердістю 2850–3600 МПа, підтвердили домінуючий вплив геометрії ріжучої частини інструмента на концентрацію напружень у зоні вершини та на стабільність стружкоутворення. Показано, що застосування укороченої передньої поверхні, зміцнювальних фасок та оптимального радіуса вершини сприяє зниженню локального перегріву, рівномірнішому розподілу сил різання і сповільненню розвитку зношування. Встановлені раціональні режими різання забезпечують підвищення стійкості інструмента на 25–30 %, покращення точності формоутворення та зменшення шорсткості поверхні оброблюваної деталі. Отримані результати можуть бути використані для оптимізації технологічних процесів обробки високоміцних сталей у важких режимах, підвищення ресурсу інструмента та покращення технологічної надійності виробництва. Запропонований підхід також створює основу для подальшого удосконалення моделей прогнозування зношування в умовах змінних навантажень. Отримані напрацювання можуть бути інтегровані в системи цифрового виробництва для підвищення керованості процесів металорізання.*

Ключові слова: *надійність; знос інструменту; втома; важке машинобудування; обробка різанням; адгезійний знос; термомеханічне навантаження; пластична деформація; різальна крайка.*

ISSN 2078-7405 Cutting & Tools in Technological System, 2025, Edition 103

UDC 621.923. **doi: 10.20998/2078-7405.2025.103.10**

MODERN MATERIALS AND PROCESSING TECHNOLOGIES AS A FACTOR IN THE DEVELOPMENT OF THE AEROSPACE AND ROCKET INDUSTRIES

Lyudmila **Kalafatova** [0009-0003-0181-3193]

Donetsk National Technical University, Drohobych, Ukraine
lydmila.kalafatova@gmail.com

Received: 24 November 2025/ Revised: 28 November 2025/ Accepted: 04 December 2025 / Published: 15 December 2025

Abstract. *The article examines the impact of modern structural materials' characteristics on the advancement of the aerospace and rocket industries. The growing role of ceramic materials with unique properties is emphasized: heat resistance, high hardness and strength; resistance to oxidation and corrosion; radio transparency; lower density compared to metals. It is often the case that they are indispensable in the manufacture of elements of rocket systems and defense industry products. However, technical ceramics belong to the category of difficult-to-machine materials, which complicates the processes of manufacturing critical products from them. Possible ways to improve the efficiency of manufacturing rocket antenna fairing - thin-walled shells of complex geometric shapes made of sitalls (a type of glass ceramics) are considered. Options for improving traditional technological processes for the manufacture of fairings using CNC machines for their mechanical processing are proposed. The use of additive SLS technology in the production of antenna fairings is substantiated. A variant of an improved technological process for manufacturing antenna fairings was presented.*

Keywords: *modern structural materials; technical ceramics; rocket antenna fairing made of glass-ceramics; blank production technology; grinding processes; machining quality and accuracy; additive technologies.*

1. Introduction

The rapid development of the aerospace and rocket industries is accompanied by the emergence of challenges that require the use of modern materials with the required properties to address them. This is possible through improved manufacturing technologies for critical components of products made from these materials, including those for aircraft.

Modern requirements for defense and aerospace products include strict adherence to quality, reliability, safety, and compliance with international standards. Key standards include AS/EN 9100 — an international standard for quality management systems for the aviation, space, and defense industries; and AS9145, which incorporates APQP (Advanced Product Quality Planning) and PPAP (Production Part Approval Process) methods used in the development of new products or modifications to existing ones.

Key requirements for defense (missiles, projectiles of various calibers) and aerospace industries products include the following:

- reliability and resistance to external influences, maintaining functionality under extreme conditions: force impacts, vibrations, temperature changes, humidity, electromagnetic interference;
- high precision and reliability of components – especially for satellites, launch vehicles, and navigation systems;
- compatibility with control and guidance systems – integration with digital platforms, GPS, and other navigation systems.

The capabilities and potential of modern rocket technology are linked to the technical level of the structural materials used. Most of these materials are difficult to machine. These include high-strength alloy steels, heat-resistant alloys based on nickel, titanium, tungsten, rare earth metals, composites [1–5] and non-metallic materials such as structural ceramics [6–8]. The latter possess unique properties and are increasingly replacing metals in the production of products in this class. The efficiency of using these materials depends on the level of processing technology used to manufacture products made from them, based on the principle of ensuring the necessary performance characteristics of rocket system components while minimizing costs.

2. Current state of research in the field of increasing the efficiency of the production of antenna fairings as an element of rocket systems

The structure of rocket systems includes ballistic missiles, launch vehicles, and sounding rockets. Each of these systems consists of four basic elements: a payload (a warhead for ballistic missiles); a propulsion system; a guidance and control system; and an overall structure. Space launch vehicles and sounding rockets are used to launch satellites into orbit and collect scientific data in the upper atmosphere. An example of the design of such a system is shown in Fig. 1.

A complex, spatially shaped nose cone is mounted on the rocket's nose, connected to a cylindrical body housing the rocket engine that provides thrust. The rocket system's surface is typically made of metal or composite materials with heat-absorbing or protective coatings.

The nose cones, which protect the seeker's antenna from aerodynamic pressure and heat, are the most critical components of the warhead of a modern rocket and most high-speed aircraft. Their primary purpose is to transmit radio frequency control signals with minimal loss and distortion under conditions of high thermal (heat flux density up to 32 MW/m^2) and force loads (excess pressure greater than 50 kPa) [9].

To perform their functions, antenna fairings must also be made of a radiotransparent material. Certain types of technical ceramics possess such properties, for example: pure oxide ceramics based on Al_2O_3, Si_2O_2, and ZrO_2; carbide ceramics based on SiC; nitride ceramics based on Si_3N_4; as well as quartz ceramics and glass ceramics – sitalls [10].

Figure 1 - Example of the design of a large research rocket (payload up to 250 kg, flight range 400 km) [9]

Sitalls are produced by fine crystallization of glasses or melts of various compositions, occurring throughout the entire volume of the formed product. Their most important properties are a low coefficient of thermal expansion, low thermal conductivity, stable permittivity over a wide temperature range, high hardness, radio transparency, heat resistance (up to 1200°C), and corrosion resistance. In Ukraine, sitalls are widely used to produce rocket antenna fairings, ensuring reliable operation of products under extreme conditions due to their strength and performance characteristics.

A radio-transparent fairing is a body of revolution, a thin-walled shell of complex spatial shape (fig. 2).

Finished parts must meet requirements for mechanical strength, heat resistance, and radio technical properties [9–12], that is, prevent control signal distortion. This is ensured by the accuracy of the part's profile and wall thickness, as well as the specified characteristics of the product's surface layer—its structure, the absence of defects, and a certain roughness.

Existing workpiece technologies to produce complex-shaped ceramic products (usually slip casting or centrifugal casting) do not allow these requirements to be met without additional mechanical processing [10]. Therefore, the blank is subjected to multi-stage mechanical processing, namely grinding with diamond

Figure 2 – Left: aerodynamic fairings (Northrop Grumman). Right: Fairings used to protect the homing system of the reentry vehicles (American Technology & Research Industries) [9]

wheels, primarily in a metal bond, on both universal and specialized machines.

Mechanical processing of products of this class is very labor-intensive. This is due to the properties of the material itself, as well as the lack of technological advancement of the fairing design [10, 12]. Signs of lack of technological advancement: large dimensions of the product (maximum diameter – up to 500 mm, height – over 1000 mm); complex curvilinear profile of the contour of the inner surface of the part, variable along the length; the need for smooth mating of individual curved sections of the inner surface; the wall thickness of the finished product is 4.0 ± 0.03 mm with a wall thickness of the workpiece up to 20.0 mm, which can be variable along the length of the product; the specified deviation of the geometric dimensions of the contours along the length of the part per diameter is: internal ≤ 0.04 mm, external less than ± 0.1 mm; roughness of the treated surface no more than $R_a = 2.0$ μm; absence of a defective layer in the finished product due to mechanical processing.

However, given the properties of glass-ceramics (a combination of high hardness and brittleness), their abrasive machining at all stages of the manufacturing process (MP) — from rough grinding to diamond finishing of both shell surfaces — is accompanied by the formation of a defective layer, the depth of which, even after finishing operations, can reach 0.2–0.5 mm. This requires a combined hardening operation. The operation consists of removing the defective layer in a solution of concentrated acids, followed by hardening of the formed surfaces in liquid salts of chemical compounds (ion bombardment). This operation is environmentally harmful, labor-intensive, and expensive. Its duration is related to the depth of the defective layer formed after the fine grinding and diamond finishing operations, which occupy up to 70% of the total machining time.

Thus, the efficiency of machining ceramic rocket fairings using traditional technology depends on the following negative factors: hard and brittle workpiece material; complex curvilinear tool path; variable cutting depth caused by uneven allowance thickness along the length of the product; non-rigid processing system;

rapid and uneven tool wear; formation of a defective surface layer that must be removed after the combined hardening operation.

An analysis of existing rocket fairing manufacturing processes has revealed that their effectiveness depends on the workpiece production method. Maximizing the workpiece's configuration and dimensional accuracy to match the corresponding part parameters allows for the significant elimination of labor-intensive and costly machining operations. This is possible using modern 3D printing technologies.

3. Formulation of the purpose of the research

The research conducted demonstrates that the labor intensity of manufacturing thin-walled shells of complex spatial shapes made of glass-ceramics and sitalls, such as rocket antenna fairings, depends on the workpiece production method. The purpose of this article was to identify ways to improve the manufacturing efficiency of these parts through the implementation of modern technologies and processing methods.

4. Presentation of the main material

4.1 Traditional methods for increasing the efficiency of mechanical processing of sitall fairings

Analysis of the basic fairing machine option.

The performance characteristics of glass-ceramic components, especially rocket antenna fairings, depend on their manufacturing conditions, starting from the basic manufacturing process, from the workpiece production stages to the final step of the complex manufacturing process, namely, the combined hardening of the pre-machined surfaces.

Until recently, aircraft fairing grinding was performed on modernized lathes equipped with high-speed grinding aggregate heads and direct force copying systems (Fig. 3).

Due to the increased brittleness and hardness of glass-ceramics, their mechanical processing is difficult, and therefore, the grinding process is multi-stage [10, 12]. It includes roughing and finishing operations of grinding the inner and outer contours. This involves removing the main allowance of up to 8–10 mm per side, unevenly along the entire profile of the part. Machining is carried out using deep grinding (cutting depth of 0.5...1.5 mm), which is accompanied by the formation of a defective layer damaged by the machining due to insufficient accuracy of the fairing wall thickness, which is unacceptable.

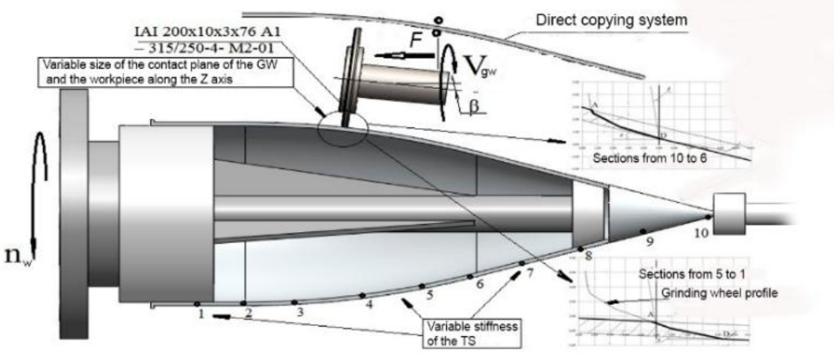

Figure 3 - Diagram of the external processing of the fairing using a representative part as an example [12]

The direct copying system does not ensure the required machining accuracy. It is significantly affected by the following factors: the accuracy of the grinding wheel installation relative to the copying device (performed by the machine operator); intensive wear of the grinding wheel and changes in its profile during operation, which requires dressing the tool during finish grinding; the high labor intensity of the internal grinding operation due to the complexity of the part profile; changing the diametrical dimensions of the internal cavity along the length of the part requires the sequential use of grinding wheels of at least three standard sizes, stopping the grinding process, and resetting the entire process system for machining with the next wheel.

The required machining accuracy of the product is achieved through the final diamond lapping of its surfaces. This part of the process is performed manually, requires many dimensional measurements, significant time investment, and highly skilled machine operators.

The sequence of stages to produce fairings from technical combined-defective glass-ceramic AC-418 (the structure of the original glass is Si_2O-Al_2O_3-Li_2O-TiO_2) is presented in Table 1.

To evaluate the effectiveness of the considered TP (see Table 1), an approximate calculation of the time spent on machining a representative part was performed. Initial data: the part (see Fig. 3) is a thin-walled shell of revolution (paraboloid of revolution) made of AC-418 sitall with dimensions: overall length L up to 750 mm, diameter of the cylindrical part of the product D_c = 200 mm, wall thickness of the product $h = 4.0 \pm 0.03$ mm with a wall thickness of the workpiece h_w = 15.0...20.0 mm.

Table 1 - Generalized basic process for manufacturing sitall fairings

The technological process of manufacturing sitall fairings		
Workpiece production technology:	Machining of the workpiece:	Combined hardening of the machined surfaces:
- synthesis of the starting material (batch production); - production of the workpiece by centrifugal casting; - crystallization of the fairing material in the workpiece.	- sequential rough and finish diamond grinding of the internal and external surfaces of the workpiece; - diamond abrasive finishing of the ground surfaces.	- removal of defective layers caused by mechanical processing by chemical etching; - strengthening of component surfaces by ion bombardment.

up to 750 mm, diameter of the cylindrical part of the product D_c = 200 mm, wall thickness of the product $h = 4.0 \pm 0.03$ mm with a wall thickness of the workpiece h_w = 15.0...20.0 mm.

The results of the time calculation indicate the low effectiveness of the basic TP. The total machining time of the fairing is T_Σ = 49 hours. The time spent on the machining process itself, T_{mp}, does not exceed 52% of T_Σ, with 20% of this time spent by the worker. Auxiliary operations of the T_{ap} also require significant time. These include interpretational inspection of the product's geometric parameters. These are performed on special measuring machines outside the machine and require the worker to reposition the workpiece. The number of repositioning reaches 8–10 and can increase if there are significant discrepancies between the workpiece and part profiles.

Thus, the main problem with the efficient processing of thin-walled parts of this type is the lack of automation in processing and inspection, coupled with the significant influence of the subjective "human" factor on the result. This problem can be partially solved by using computer numerical control (CNC) machines for abrasive machining operations.

Using CNC machines in fairing manufacturing.

The efficiency of using CNC machines increases with the increasing complexity of the workpiece profile and the need to achieve high-quality, precision-machined surfaces. However, the grinding process for fairings is characterized by a rapid loss of tool dimensional accuracy due to intense wheel wear and dynamic instability of the system [10, 12]. Therefore, CNC machines must compensate for changes in workpiece allowances, deformations in the process system, temperature effects, machine errors during coordinate movement, and other factors.

Complete machines of fairings are possible using the STUDER series machines [13].

The machining process is preceded by the preparation of a control program. For this purpose, a 3D model of the workpiece is developed, considering its configuration and all specified dimensions, after which the program itself is written [14].

These machines are equipped with the following key components:

– a GE FANUC Series 16-T CNC system, which allows scanning of the internal and external profiles of the workpiece before machining, which is necessary for the automatic calculation of grinding allowance and the assignment of rational cutting parameters in accordance with the machining program;

– a specialized system for measuring and monitoring the dimensional accuracy, geometry, and surfaces of workpieces and parts, as well as mechanical machine components, using control sensors, measuring heads, and feeler gauges, as well as for monitoring and controlling machine operation, including grinding wheel balancing;

– adjustable vibration mounts for vibration damping, which increases machining accuracy;

– self-centering devices for mounting the workpiece on external and internal surfaces;

– a universal rotating grinding head for external and internal grinding, programmable for every 1.0° of rotation, and a device for adjusting the angle of the working elements;

– a set of diamond grinding wheels and a mechanism for their automatic change according to the program;

– a device for automatic dressing of the wheels as they wear out, controlled by the CNC system.

The machine's design, using a dedicated software subsystem, allows for the integration of machining and inspection operations directly on the machine for all stages of fairing grinding, significantly reducing the overall time required for its machining.

The results of the time analysis for implementing the TP option, compared to a traditional one, revealed the following. The CNC machining option reduces the time required for intermediate operations within the T_{Σ} structure as follows: auxiliary T_{ap} – by almost 14 times; finishing, as the most complex and critical operation, by 3 times. This reduces the overall fairing machining time by 3.3 times – from 49.0 hours to almost 15.0 hours, while maintaining the specified accuracy and quality of machining.

Based on the obtained results, it can be concluded that using CNC machines is rational for the machining of complex, thin-walled components, such as glass-ceramic rocket fairings. However, even in this case, the abrasive machining process results in the formation of a defective layer on the machined surfaces, which is unacceptable from the standpoint of ensuring the fairings' performance characteristics and requires a combined hardening operation.

The results of an analysis of existing manufacturing processes for large-size shell-type parts led to the conclusion that their effectiveness depends on the workpiece production method. Maximizing the configuration and dimensional accuracy of the workpiece to the corresponding part parameters allows for the significant elimination of labor-intensive and costly machining operations.

4.2 Possibilities of implementing additive technologies to produce antenna fairings from sitall

Additive manufacturing technologies for ceramic products offer significant opportunities for creating complex ceramic shells [15, 16]. Each method is based on the gradual deposition of material or its layer-by-layer formation in accordance with a 3D model of the product.

One of the most common methods is SLS (Selective Laser Sintering) [17-19]. SLS operates by sintering polymer powders of various ceramic components with a laser beam. These powders are applied layer by layer onto a special platform, and each layer is bonded with a liquid binder. After the process is complete, the resulting product undergoes a stage of removing the remaining binder and subsequent heat treatment in a furnace to achieve the desired density and strength.

The advantage of SLS technology is that other methods, which involve applying materials during wet molding [17], require heat treatment. This leads to chipping and cracking in thin-walled ceramic parts such as antenna fairings.

A schematic diagram of a part printed using SLS is shown in Figure 4.

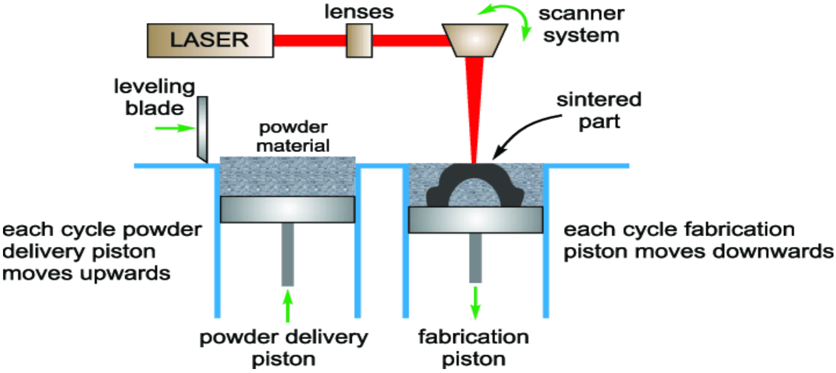

Figure 4 – Schematic diagram of the SLS method [20]

The main advantage of using additive manufacturing is its ability to solve the problem of workpiece production, where the profile of a workpiece obtained using conventional methods differeds significantly from the final product profile. This necessitated multi-stage machining (primarily abrasive machining with diamond tools), which resulted in the formation of a defective layer that must be removed during a combined hardening operation on the machined surfaces.

Additive manufacturing eliminates grinding operations, leaving only finishing operations for high-quality surfaces. This is because even with low material deposition rates during part formation, the surface quality obtained in an SLS machine will not always meet the requirements of the final product.

Based on the above, it is possible to develop an updated process for manufacturing parts such as antenna fairings from glass-ceramics using additive manufacturing as follows (Table 2).

Table 2 – Structure of the production process for manufacturing fairings from AC-418 sitall using SLS technology

Fairing manufacturing process		
Workpiece production technology:	Machining of the workpiece:	Combined hardening of machined surfaces:
- high-precision, high-quality workpiece production using SLS; - heat treatment of the workpiece to eliminate internal defects. .	- abrasive surface treatment (finishing operations – diamond finishing or lapping) to ensure the required precision and quality of the product (accompanied by the formation of a defective layer of shallow depth and rational structure).	- removal of the layer damaged by treatment with chemical etching; - hardening of the component surfaces by ion bombardment.

A comparison of two manufacturing processes for fairings made of AC-418 sitalls (basic traditional and using SLS technology) reveals the following advantages of additive manufacturing.

• The SLS method eliminates the need for traditional, consumable workpiece production technology.

• Knowing the material deposition rate during product formation on the SLS machine and the dimensions of the representative part, the total workpiece production time can be estimated at 7.5 hours.

• The precision and quality of the product surfaces formed under such conditions allow for the complete elimination of rough and fine grinding operations, leaving only the finishing abrasive operation if necessary.

- The fairing machining time is reduced to one hour when forming a defective layer with a favorable structure and shallow depth (due to gentle machining conditions at low cutting forces), which will reduce the time of the combined operation of the operation of the part.
- The total time spent on manufacturing the fairing will not exceed 10.0 hours, with lower costs for equipment and reorganization of production.

5. Conclusions

This article examines the manufacturing processes for complex-shaped shells made from difficult-to-machine materials, using a sitall-based rocket nose cone as an example. The need to improve existing manufacturing technologies for this class of components is substantiated.

This paper also includes:

1. The physical and mechanical properties of difficult-to-machine structural materials used to manufacture rocket system components, including nose cone antenna fairing, are examined.
2. The priority of using various ceramic materials for the manufacture of rocket and aerospace components, including rocket nose cone radomes, is confirmed.
3. The basic manufacturing process for the sitall nose antenna fairing is analyzed.
4. It is established and confirmed that the labor intensity of sitall nose cone manufacturing depends on the workpiece production method.
5. The need to use CNC machines to improve the efficiency of machining the sitall antenna fairing is substantiated.
6. The potential effectiveness of using additive manufacturing techniques in antenna fairing production is analyzed.
7. A rational method for blank production using additive manufacturing is presented – using SLS technology, which allows for minimizing subsequent machining requirements for the antenna fairing.
8. An improved technological process for manufacturing antenna fairing using SLS technology is presented.

References: 1. *Rahul Soni, Rajeev Verma, Rajiv Kumar Garg, Varun Sharma* A Critical Review of Recent Advances in Aerospace Materials Today, vol. 113, pp. 180-184, 2024. **2**. Materials Used in Space Shuttle: Evolution, Challenges, and Future Prospects – An Overview", Composites, Part B 303, 2025. DOI.org/10.1016/j.compositesb.2025.112540. **3**. *Shravan Kumar Korukonda* Evolution of Aerospace Materials: A Review, International Research Journal of Engineering and Technology (IRJET), vol. 09 Issue: 04, pp. 940–948, 2022. **4**. *Maria Mrazova* Advanced Composite Materials of the Future in Aerospace Industry, Incas Bulletin, vol. 5, Issue: 3, pp. 139–150, 2013. ISSN 2066–8201. DOI: 10.13111/2066–8201.2013.5.3.14. **5**. *Guanlin Hao* The Advanced Materials for Aerospace Industry, Highlights in Science, Engineering and Technology AMCCE, vol. 120, pp.364–3677, 2024. **6**. Advanced Ceramics for Aerospace Applications — Precise Ceramics, LCM Advanced Ceramic Materials, [Online]. Available: https://www.preciseceramic.com/applications/aerospace.html. [Accessed: 10. November 2025]. **7**. International Applications for Advanced Ceramics in the Aerospace Industry, Corning Incorporated. All Rights Reserved, [Online]. Available: https://www.corning.com/media/worldwide/csm/images/Macor_FA_AerospaceV7_Final_CM.pdf. [Accessed: 10. November 2025]. **8**. *Dongming Zhu* Aerospace Ceramic Materials: Thermal, Environmental Barrier Coatings and SiC/SiC Ceramic Matrix Composites for Turbine Engine Applications, NASA/TM—2018-219884, [Online]. Available: https://ntrs.nasa.gov/api/citations/20180002984/ downloads/20180002984.pdf. [10. November 2025]. **9**. Guide to the Missile Technology Control Regime Annex, 2010. [Online]. Available: https://www.mtcr.info/download/pictures/d5/zwkvd85x6nzx7xji0ktex2rxfnlofj/mtcr_annex_handbook_rus.pdf [10. November 2025]. **10.** *L. P. Kalafatova, P. G. Matyuha, D. V. Pokolenko, S. Yu. Oliinyk, S. A. Poezd*, Improving the Efficiency of Grinding Hard Alloys and Structural Ceramics: A Monograph. Pokrovsk: DonNTU, 2017 (in Ukrainian) ISBN 978-966-377-207-3. **11**. *A. G. Romashin, V. E. Gaydachuk, Ya. S. Karpov*, Radiotransparent Aircraft Fairings. Design, Structural Materials, Production Technology, and Testing: a tutorial. Kharkov: Publishing Center "KhAI Center Publ.", 2003 (in Ukrainian). **12**. *L. P. Kalafatova* Perspectives for Improving the Efficiency of Machining of Complex Profiles of Products from Brittle Nonmetallic Materials, Cutting & Tools in Technological System, 2025, Edition 91 (2019), pp. 69-77, 2019 (in Ukrainian). **13**. CNC Grinding Machine [Online]. Available: https://mach4metal.com/ua/slifuvalni-verstati/cilindricno-slifuvalnii-verstat/studer-s-40-cnc. [10. November 2025]. **14**. *N.V. Onofreychuk*, Fundamentals of Machining and Programming on Numerically Controlled Machines: textbook, Lviv: Svit, 2019 (in Ukrainian). **15**. Additive Manufacturing of Ceramics for Extreme Environments: NASA Marshall Space Flight Center [Online]. Available: https://ntrs.nasa.gov/api/citations/ 20240004693/downloads/Jamboree%202024%20-%20AM%20Ceramics.pdf. [10. November 2025]. **16**. Additive Manufacturing in Defense and Aerospace, GENESYS DEFENSE Advanced Warfare and Technology, ISSN: 3068-7160, [Online]. Available: https://genesysdefense.com/intl/additive-manufacturing-in-defense-and-aerospace/. [10. November 2025]. **17**. *Adeniyi Kehinde Adeleke, Danny Jose Portillo Montero, Oluwaseun Augustine Lottu, Nwakamma Ninduwezuor-Ehiobu, and Emmanuel Chigozie Ani* 3D Printing in Aerospace and Defense: A Review of Technological Breakthroughs and Applications, World Journal of Advanced Research and Reviews, 2024, 21(02), pp. 1149–1160. doi.org/10.30574/wjarr.2024.21.2.0558. **18**. *Nikolina Kovacev, Sheng Li, Weining Li, Soheil Zeraati-Rezaei, Athanasios Tsolakis and Khamis Essa,* Additive Manufacturing of Novel Hybrid Monolithic Ceramic Substrates, Aerospace 2022, *9*(5), 255; https://doi.org/10.3390/aerospace9050255. **19**. Selective Laser Spinning (SLS), [Online]. Available: https://3ddevice.come.ua/selektivnoe-lazernoe-spekanie-sls/. [10. November 2025]. **20**. Implementation of Technology SLS, [Online]. Available: https://www.researchgate.net/figure/A-schematic-diagram-of-the-SLS-machine_fig6_260094770. [10. November 2025].

Людмила Калафатова, Дрогобич, Україна

СУЧАСНІ МАТЕРІАЛИ І ТЕХНОЛОГІЇ ЇХ ОБРОБЛЯННЯ ЯК ФАКТОР РОЗВИТКУ АЕРОКОСМІЧНОЇ ТА РАКЕТНОЇ ПРОМИСЛОВОСТЕЙ

Анотація. *У статті розглядається вплив характеристик сучасних конструкційних матеріалів на розвиток аерокосмічної та ракетної промисловості. Підкреслюється зростаюча роль використання керамічних матеріалів, що мають унікальні властивості: термостійкість; високі твердість та міцність; стійкість до окислення та корозії; радіопрозорість; меншу щільність проти металів. Однак технічні кераміки відносяться до категорії важкооброблюваних* *матеріалів, що ускладнює процеси виготовлення відповідальних виробів з них, в тому числі головних обтічників ракет, літальних апаратів (ЛА). Обтічники ЛА - тонкостінні складно-профільні оболонки, до яких пред'являються підвищені вимоги щодо точності геометричних розмірів і форми, а також якості поверхонь. Вони виробляються з радіопрозорих крихких неметалевих матеріалів, в тому числі з різновиду склокераміки – ситалів. Сучасні заготівельні технології (здебільшого це шлікерна технологія або відцентрове литво) не дозволяють забезпечити точність форми виробу і потрібну якість його поверхонь на етапі отримання заготовки. Тому виріб піддається трудомісткій багатоетапній механічній обробці, а саме операціям чорнового і чистового шліфування алмазними інструментами, які супроводжуються крихким руйнуванням оброблюваного матеріалу і формуванням порушеного обробкою дефектного шару. Це є неприпустимим з точки зору забезпечення експлуатаційних характеристик обтічників і передбачає наявність заключної операції - комбінованого зміцнення порушеного обробкою шару. Запропоновано варіанти вдосконалення традиційних технологічних процесів виготовлення обтічників за рахунок використання для їх механічної обробки верстатів з ЧПК, що дозволяє підвищити продуктивність операцій абразивного обробляння. Встановлено, що максимальне наближення конфігурації і точності розмірів заготовки до відповідних параметрів деталі дозволяє у значній мірі відмовитися від трудомістких і витратних операцій механічної обробки. Це можливо за рахунок використання сучасних 3D-технологій друку. Виходячи з цього, обґрунтовано використання адитивної технології SLS при виробництві головних антенних обтічників ракет і представлений варіант удосконаленого технологічного процесу їх виготовлення.*

Ключові слова: *сучасні конструкційні матеріали; технічна кераміка; антенні обтічники ракет із ситалів; заготівельні технології; процеси шліфування виробів; якість і точність обробки; адитивні технології.*

ISSN 2078-7405 Cutting & Tools in Technological System, 2025, Edition 103

UDC 621.7 **doi: 10.20998/2078-7405.2025.103.11**

PROJECT MANAGEMENT BASICS FOR 3D CONCRETE PRINTING: TIME CALCULATION STANDARDS FOR DESIGN AND TECHNOLOGICAL PREPARATION AND QUALITY ASSURANCE

Yaroslav **Garashchenko** [1][0000-0003-2568-4763], Andrii **Malyniak** [1][0009-0001-5837-414X], Ruslan **Kucher** [2][0009-0000-5835-4600]

[1]National Technical University «Kharkiv Polytechnic Institute», Kharkiv, Ukraine
[2]Mykolaiv National Agrarian University, Mykolaiv, Ukraine
yaroslav.garashchenko@gmail.com

Received: 24 November 2025/ Revised: 30 November 2025/ Accepted: 07 December 2025 / Published: 15 December 2025

Abstract. *This research establishes the first comprehensive project management framework for 3DCP through quantitative standards for design preparation, technological setup, and quality management. Based on systematic analysis of construction projects completed during 2023-2025 by "Geopolimer" LTD (Kharkiv, Ukraine), we developed mathematical models for time estimation incorporating perimeter length, geometric complexity, and feature count parameters. Regression analysis of project data enabled formulation of predictive equations: design preparation time accounts for base setup, perimeter-dependent modeling, and complexity coefficients (complex curved surfaces with architectural details). Technological preparation time integrates G-code generation, trajectory verification per meter, and build step validation. A systematic complexity classification system evaluates four geometric factors: curved surfaces percentage, architectural detail count, protruding elements, and internal cavity complexity, enabling quantitative risk assessment and resource allocation decisions. The framework incorporates a three-level quality management system with standardized defect classification (aesthetic, attention-required, critical) defining acceptance criteria for crack dimensions, surface porosity, and structural integrity. Trajectory verification methodology enables proactive defect identification, detecting 85-90% of potential issues before production begins. Economic analysis demonstrates 8-12% rework cost avoidance, 15–20% preparation time savings, and 5–10% schedule compression, with return on investment achieved within 0.5–1.5 months. Case study validation on a 174 m² residential structure demonstrates framework effectiveness: calculated preparation time of 45.1 hours versus actual 47.2 hours. The framework facilitates 3DCP transition from experimental technology to predictable industrial process, enabling evidence-based project planning, systematic risk management, and competitive market positioning. Future research directions include expansion to additional printer types, integration with Building Information Modeling workflows, real-time computer vision quality monitoring, and long-term performance tracking for continuous standard refinement.*

Keywords: *concrete 3D printing; project management; time standards; complexity classification; quality assurance; defect detection.*

1. Introduction

The construction industry faces unprecedented challenges, including labor shortages, rising material costs, and increasing demands for sustainable building practices [1, 2]. Construction 3*D* printing (3*DCP*) emerges as a transformative technology offering potential solutions through automation, material optimization, and design flexibility. However, the transition from technological capability to industrial implementation requires robust project management frameworks that address planning, resource allocation, quality control, and risk management [3].

Critical management gaps in current 3*DCP* practice include.

Absence of standardized time norms – project managers lack reliable estimates for design preparation and technological setup, hindering accurate scheduling and cost forecasting.

Insufficient resource planning tools – without systematic complexity assessment methods, labor and equipment allocation remain largely empirical, leading to inefficiencies and budget overruns.

Limited quality control protocols – the lack of standardized defect classification and verification procedures prevents systematic quality assurance and creates accountability challenges.

Process uncertainties in trajectory planning, material behavior, and geometric accuracy require structured risk management approaches.

This research establishes comprehensive technical, management tools, and software for 3*DCP* implementation.

Purpose of the article – develop quantitative standards for design and technological preparation, enabling evidence-based project planning and resource optimization.

2. Review of the literature

Technology adoption frameworks in construction have been extensively studied [4], establishing that successful implementation requires alignment of technical capability, organizational readiness, and management systems. Research on Building Information Modeling (BIM) adoption provides relevant insights: systematic standards development accelerated industry acceptance by providing predictable workflows and cost structures [5].

Critical success factors identified in construction technology literature include: standardized processes (enabling training and quality control), quantifiable performance metrics (supporting decision-making), and risk mitigation protocols (reducing adoption barriers) [6]. These factors directly inform the development approach for 3*DCP* management frameworks.

Work measurement methodologies in manufacturing provide foundational concepts applicable to 3*DCP*. Time and motion studies in additive manufacturing [7] demonstrate that preparation time correlates with geometric complexity through quantifiable parameters. However, construction-scale applications introduce unique factors: larger dimensions, material properties, and environmental influences.

Complexity assessment approaches in construction project management typically employ parametric methods [8]. Research on prefabricated construction identifies similar challenges: translating design intent into manufacturable elements, managing geometric variations, and ensuring assembly compatibility [9]. The proposed framework adapts these methodologies to 3*DCP* specifics.

Quality control frameworks for 3*DCP* remain underdeveloped compared to traditional construction [10]. Previous research [own publication reference] established relationships between process parameters (layer thickness) and quality outcomes (geometric accuracy, surface defects). However, systematic management approaches integrating defect prevention, real-time monitoring, and corrective action protocols are absent from current literature.

Computer vision applications show promise for automated quality assessment [11], but require standardized defect classification schemes and verification protocols to enable practical implementation. The integration of AI-assisted tools for trajectory verification represents an emerging research direction with significant management implications.

Process uncertainty in 3*DCP* stems from material rheology variations, environmental factors, and equipment performance fluctuations [12]. Risk management literature emphasizes proactive verification over reactive correction [13]. The proposed trajectory verification methodology addresses this principle by identifying potential issues before production begins.

Economic optimization studies in construction technology adoption [14] demonstrate that systematic planning reduces total project costs through: waste minimization (material optimization), schedule compression (efficient resource utilization), and quality improvement (reduced rework). These benefits justify investment in standardization frameworks.

3. Standards development framework

3.1 Data collection and analysis

The research analyzed completed projects spanning 2023-2025 ("Geopolimer" LTD, Kharkiv), including (data parameters collected):

– project specifications – perimeter length (L_c), area, height, geometric features;

– time records – design preparation (T_{dp}), technological preparation (T_{tp}), total project duration (T_p);

– complexity factors – curved surfaces, architectural details, protruding elements, internal cavities;

– quality metrics – defect occurrence, rework requirements.

Regression analysis identified significant correlations ($R^2 > 0.85$) between geometric parameters and preparation time. Expert validation sessions (3 technology specialists) refined coefficient values and validated practical applicability.

3.2 Design preparation (DP) standards development

Design preparation (T_{dp}) encompasses engineering work adapting architectural documentation to 3*DCP* technological capabilities.

Process stages:

– architectural documentation analysis;
– geometry verification for printability;
– design adaptation to printer limitations;
– working 3*D* model creation;
– CAM software preparation for *G*-code generation.

Time estimation model:

$$T_{dp} = T_0 \times K_{c0} + t_N \times L_c \times K_c,$$

where: T_0 – base constant (4.0 hours), initial setup, software configuration, project initialization; t_N – time per meter perimeter (20 minutes/m) – model development rate; L_c – total wall perimeter includes external, internal, partition walls, m; K_{c0} – base complexity coefficient (overall project complexity); K_c – detailed complexity coefficient (geometric feature adjustments).

This model enables project managers to:

– generate time estimates during proposal development;
– allocate engineering resources based on quantitative requirements;
– establish project milestones with defined deliverables;
– calculate labor costs for accurate pricing.

Example calculation. Residential building L_c = 85 m, medium complexity, K_{c0} = 1.0 (straight walls with connection diaphragms), K_c = 1.0 (balanced geometric features).

$$T_{dp} = 4.0 \times 1.0 + (20/60) \times 85 \times 1.0 = 32.3 \text{ hours}.$$

Time units for T_{dp} are expressed in hours throughout the model, with t_N converted from minutes (20 min/m = 0.333 h/m) for computational consistency.

Resource allocation: 2 engineers × 16 hours or 1 engineer × 32 hours (schedule dependent).

3.3 Complexity classification system

Geometric complexity assessment provides a systematic basis for coefficient determination. Base complexity coefficient (K_c) by expert assessment based on table 1.

Table 1 – The complexity coefficient

Level	Characteristics	Coefficient	Typical Applications
Low	Small-scale, straight walls, simple geometry	0.7	Standard modules, basic structures
Medium	Straight walls with structural diaphragms	1.0	Residential buildings, warehouses
High	Curved walls, complex connections, decorative elements	1.2–2.0	Architectural features, custom designs

The detailed complexity coefficient K_c is calculated as:

$$K_c = K_{c1} \times K_{c2} \times K_{c3} \times K_{c4},$$

where: K_{c1} – curved surfaces percentage (low (<10%) – 0.9, medium (10–30%) – 1.0, high (>30%) – 2.0); K_{c2} **-** architectural details count **(**low (<10 elements) – 0.95, medium (10–50 elements) – 1.0; high (>50 elements) – 1.5, K_{c3} – protruding elements count **(**low (<5 elements) – 0.8, medium (5–20 elements) – 1.0, high (>20 elements) – 1.3); K_{c4} – internal cavity complexity (low (absent/simple planar) – 0.9, medium (planar surfaces) – 1.0, high (curved surfaces) – 2.0.

This classification of the management decision support enables:

– risk assessment (higher coefficients indicate increased preparation complexity and potential delays);

– resource planning (coefficient magnitude guides team composition);

– cost estimation (systematic pricing based on quantified complexity rather than subjective assessment);

– client communication (transparent explanation of time/cost variations between projects).

3.4 Technological preparation (TP) standards

Technological preparation encompasses *G*-code generation and verification for print execution:

– 3*D* model import to CAM software;

– Print parameter configuration (extrusion speed, layer thickness, trajectory direction);

– *G*-code generation (extruder movement paths);

– Program verification (correctness, feasibility, constraint validation).

Time estimation model:

$$T_{\mathrm{tp}} = T_0 + t_{н\_L} \times L_c + t_{н\_k} \times n_к,$$

where: T_0 – time for setup and *G*-code generation, T_0 = 0.5 hours; $t_{\mathrm{н\_L}}$ – verification time per meter (1 min/m = 0.0167 h/m); L_c – total wall perimeter, m; $t_{н\_k}$ – verification per build step (2 min/step = 0.0333 h/step); $n_{\mathrm{к}}$ – number of build steps (layers/sections).

Example. Building with L_c = 85m, height H_{w} = 3.0m, layer height h_{l} = 15mm:

$$n_к = 3000\text{mm} / 15\text{mm} = 200 \text{ steps},$$

$$T_{\mathrm{tp}} = 0.5 + (1/60) \times 85 + (2/60) \times 200 = 8.6 \text{ hours}.$$

This are enables scheduling of technical specialists, equipment allocation planning, and identification of optimization opportunities through trajectory analysis.

4. Quality management system

The verification process follows a sequential logic: geometric validation – technological feasibility – optimization – quality assurance, with each stage serving as a gate for the subsequent phase.

Trajectory verification framework:

– geometric correctness (trajectory continuity, intersection detection, angle validation);

– technological validation (speed limits, layer heights, material flow rates, overhang angles);

– optimization (idle movement minimization, collision avoidance);

– quality control (dimensional compliance, structural integrity assurance).

Risk mitigation. Verification identifies 85–90% of potential defects before production, reducing material waste and rework costs by estimated 12–18% based on project data analysis.

Defect classification and control (severity) limits establish quality acceptance criteria (levels):

1 – aesthetic only (crack width <0.5mm, depth <2mm, surface pores <3mm diameter, density <5/dm²), acceptable with client approval;

2 – requires attention (crack width 0.5–1.5mm, depth 2–5mm, surface pores 3–8mm diameter, density 5–15/dm²), corrective action recommended;

3 (critical) – immediate intervention (crack width >1.5mm, depth >5mm, surface pores >8mm diameter, density >15/dm²), component rejection or mandatory repair.

KPI tracking – quality metrics monitored per project enable continuous improvement and benchmarking across project types.

5 Economic analysis

AI integration in 3*DCP* project management. The framework incorporates artificial intelligence tools at critical decision points: machine learning algorithms optimize trajectory generation by analyzing geometric complexity patterns from historical projects (reducing manual planning time by 15–20%), computer vision systems enable real-time defect detection during trajectory verification phase (achieving 85–90% accuracy in identifying potential surface defects, geometric deviations, and structural anomalies before production), and natural language processing assists operators through conversational interfaces for parameter selection and troubleshooting. AI implementation requires minimal technical infrastructure – cloud-based API access or local deployment options - making it accessible for small to medium construction enterprises. The economic analysis below quantifies investment requirements and returns from this AI-enhanced standardization framework.

Investment requirements (cost-benefit AI-framework):

- standards implementation – 40–64 hours (documentation, training),
- AI tool subscription – $20–40/month;
- process AI-optimization: 24–80 hours initial setup.

Benefits quantification (based on project database) are shows in table 2.

Table 2 – Benefits quantification

Benefit Category	Impact
Time savings (preparation)	15–20% reduction
Material waste reduction	12–18% decrease
Rework elimination	8–12% cost avoidance
Schedule compression	5–10% faster delivery
Total annual benefit	40–60%

These benefits (table 2) compound over multiple projects, with mature implementation achieving upper range values (60% total annual benefit) after 3–6 months of standardized practice.

Data in table 2 show ROI (payback period 0.5–1.5 months for typical implementation).

Key risks and mitigation strategy are presented in table 3.

Table 3 – Key risks and mitigation

Risk	Probability	Impact	Mitigation Strategy
Engineer resistance	Medium	Medium	Comprehensive training, pilot success demonstration
Tool learning curve	High	Low	Structured onboarding, ongoing support
Standard deviation from practice	Low	Medium	Flexible coefficient adjustment, continuous validation
Technology obsolescence	Low	High	Regular review cycles, modular framework design

6. Case study validation

Framework validation through real project application. To verify practical applicability and accuracy of the developed time estimation models and complexity classification system (table 1), we conducted retrospective analysis comparing traditional approach versus standardized framework on a completed residential construction project. The validation methodology involved: reconstructing actual preparation timeline from project documentation to establish baseline, applying standardized formulas with measured parameters (perimeter, complexity coefficients) to calculate predicted time, comparing predicted versus actual values to assess model accuracy, and evaluating qualitative improvements in resource allocation and defect prevention. This approach enables quantification of both temporal precision (variance percentage) and operational benefits (reduced rework, improved planning reliability).

Project profile - residential structure 174 m², L_c = 92m.

Traditional approach (no standards). Preparation time – 52 hours (estimated retrospectively). Standardized approach (framework applied) – calculated time: T_{kp} = 35.3h, T_{tp} = 9.8h, T = 45.1h. Actual time – 47.2h (variance +4.7%, within acceptable ±5% tolerance for project management standards). This accuracy enables reliable client commitments and resource scheduling.

Predictable scheduling enabled better resource allocation, trajectory verification prevented two major geometric errors (saving an estimated 18 hours of rework), and systematic quality control reduced client revision cycles.

7. Conclusions

This research establishes the first comprehensive project management framework for construction 3*D* printing, addressing critical gaps in time standardization, resource optimization, and quality assurance.

Key contributions:

- mathematical models for preparation time estimation enable accurate project planning and cost forecasting across diverse construction applications;
- systematic complexity classification provides quantitative basis for risk assessment and resource allocation decisions;
- quality management protocols with defect classification and verification methodology reduce rework costs and enable systematic process improvement;
- AI integration framework demonstrates practical application of emerging technologies in construction workflows while addressing organizational change management.

Standards enable construction companies to transition 3*DCP* from experimental technology to predictable production process, accelerating market adoption and competitive positioning.

Widespread adoption of these standards could reduce average 3*DCP* project costs by 15–25% while improving schedule predictability by 30–40%, accelerating market competitiveness against traditional construction methods.

Future research directions:

– expansion to additional printer types and material systems;

– integration with BIM (Autodesk Revit, ArchiCAD) workflows and digital construction platforms;

– development of real-time quality monitoring systems using computer vision;

– long-term performance tracking and standard refinement based on accumulated project data.

Framework designed for immediate implementation by construction companies, requiring minimal investment while delivering measurable operational improvements.

References: **1.** *Athira, R., Sathyan, D.* Review of 3d Printing Advancements in Geopolymer Concrete: Current Challenges and Future Directions. Proceedings of International Conference on Advances in Materials, Modeling, and Analysis for Sustainable and Resilient Infrastructure Volume 1. AMMA SRI 2025. Lecture Notes in Civil Engineering, vol 719. 2025. https://doi.org/10.1007/978-981-95-0229-5_39. **2.** *Garashchenko, Y., Harashchenko, O., Kucher, R.* Additive technologies in construction: technical, economic and management analysis. Cutting & Tools in Technological System, (101), 2024. 103–115. https://doi.org/10.20998/2078-7405.2024.101.10. **3.** *Alhaidary, H.* Three-Dimensional Concrete Printing as a Construction Automation Strategy and Assessments from a Case Study Building. Journal of Architectural Engineering. Vol.30, 2. 2024. https://doi.org/10.1061/JAEIED.AEENG-1714. **4.** *Sepasgozar, S.M., Davis, S.* Modelling the Construction Technology Implementation Framework: An Empirical Study. Proceedings of the 32nd ISARC. p. 1–8. 2015. https://doi.org/10.22260/ISARC2015/0103. **5.** *Waqar, A., Othman, I., Hayat, S., Radu, D., Khan, M.B., Galatanu, T.F., Almujibah, H.R., Hadzima-Nyarko, M., Benjeddou, O.* Building Information Modeling – Empowering Construction Projects with End-to-End Life Cycle Management. Buildings 2023, 13, 2041. 2023. https://doi.org/10.3390/ buildings13082041. **6.** *Yucel, B., Azhar, S.* Investigating critical success factors and risks of construction technology startups: a systematic literature review. International Journal of Construction Management, 24, p. 1655–1667. 2023. https://doi.org/10.1080/15623599.2023.2286109. **7.** *Bos, F. P., Wolfs, R. J. M., Ahmed, Z. Y., Salet, T.A.M.* Additive manufacturing of concrete in construction: potentials and challenges of 3D concrete printing. Virtual and Physical Prototyping, 11(3), 209–225. 2016. https://doi.org/ 10.1080/17452759.2016.1209867. **8.** *Hossny, H.E., Ibrahim, A.H. and Elnady, A.* Assessment of construction project complexity. The Open Civil Engineering Journal, 15(1), pp.414–423, 2021. https://doi.org/10.2174/1874149502115010414. **9.** *Lu, W., Tan, T., Xu, J., Wang, J., Chen, K., Gao, S. & Xue, F.* Design for Manufacture and Assembly (DfMA) in construction: The old and the new. Architectural Engineering and Design Management, in press. 17p. 2020. https://doi.org/ 10.1080/17452007.2020.1768505. **10.** *Wolfs, R., Bos, D., Caron, J., Gerke, M., Mesnil, R., Buswell, R., Ducoulombier, N., Hack, N., Keita, E., Kinnell, P., Mawas, K., Mechtcherine, V., Miranda, L., Sokolov, D., Versteege, J., & Roussel, N.* On-line and in-line quality assessment across all scale levels of 3D concrete printing. Cement and Concrete Research. 2024. https://doi.org/10.1016/j.cemconres.2024.107646. **11.** *Balakrishna, K., Tiwari, D.V., Deshpande, D.A., Patil, S.R., Garg, D.A., & Geetha, D.B.* Computer Vision for Automated Quality Inspection in Manufacturing. 2024 International Conference on Advances in Computing, Communication and Applied Informatics (ACCAI), 1–6. 2024. https://doi.org/10.1109/ACCAI61061.2024.10601894. **12.** *Jeyifous, O.A., Schönsee, E., Strangfeld, C., & Hüsken, G.* Investigating the impact of material rheology on geometric accuracy in 3D concrete printing using real-time monitoring. e-Journal of Nondestructive Testing. 2025. https://doi.org/10.58286/31704. **13.** *Pena, N.M., Vieira, J.G., & Mano, A.P.* Systematic Review on Risk Management on maintenance. 2021. http://dx.doi.org/10.14488/ENEGEP2021_TI_ST_354_1822_42829. **14.** *Senouci, A., Bowlekar, U.N., Khalafi, S.A. and Eldin, N.*, A multi objective scheduling model for minimization of construction project duration, total cost and environmental impact. In Proceedings of the Creative Construction Conference. (2019) 025. https://doi.org/10.3311/ccc2019-025.

Ярослав Гаращенко, Андрій Малиняк, Харків, Україна, Руслан Кучер,
Миколаїв, Україна

ОСНОВИ УПРАВЛІННЯ ПРОЄКТОМ ДЛЯ 3D-ДРУКУ БЕТОНОМ: СТАНДАРТИ РОЗРАХУНКУ ЧАСУ НА

КОНСТРУКТОРСЬКУ ТА ТЕХНОЛОГІЧНУ ПІДГОТОВКУ ТА ЗАБЕЗПЕЧЕННЯ ЯКОСТІ

Анотація. *Дане дослідження встановлює першу комплексну систему управління проєктами для 3D друку бетоном через кількісні стандарти конструкторської підготовки, технологічного налаштування та управління якістю. На основі систематичного аналізу будівельних проєктів, завершених протягом 2023-2025 років ТОВ "Геополімер" (Харків, Україна), розроблено математичні моделі оцінки часу з урахуванням периметра, геометричної складності та кількості елементів. Регресійний аналіз проєктних даних дозволив сформулювати прогнозні рівняння: час конструкторської підготовки враховує базове налаштування, моделювання залежно від периметра та коефіцієнти складності. Час технологічної підготовки інтегрує генерацію G-коду, верифікацію траєкторії на метр та перевірку кроків побудови. Систематична класифікація складності оцінює чотири геометричні фактори: відсоток криволінійних поверхонь, кількість архітектурних деталей, виступаючі елементи та складність внутрішніх порожнин, забезпечуючи кількісну оцінку ризиків та прийняття рішень щодо розподілу ресурсів. Система включає трирівневу систему управління якістю зі стандартизованою класифікацією дефектів (естетичні, що потребують уваги, критичні), що визначає критерії прийнятності для розмірів тріщин, пористості поверхні та структурної цілісності. Методологія верифікації траєкторії забезпечує проактивне виявлення дефектів, виявляючи 85-90% потенційних проблем до початку виробництва. Економічний аналіз демонструє зменшення відходів матеріалів на 12-18%, уникнення витрат на переробку на 8-12%, економію часу підготовки на 15-20% та скорочення графіку на 5-10%, з окупністю інвестицій за 0,5-1,5 місяця. Валідація на прикладі житлової структури 174 м² демонструє ефективність системи: розрахований час підготовки 45,1 години проти фактичних 47,2 години становить відхилення 4,7% для стандартів управління проєктами. Система сприяє переходу 3D друку бетоном від експериментальної технології до передбачуваного промислового процесу, забезпечуючи науково обґрунтоване планування проєктів, систематичне управління ризиками та конкурентне позиціонування на ринку. Майбутні напрямки досліджень включають розширення на додаткові типи принтерів, інтеграцію з робочими процесами інформаційного моделювання будівель, моніторинг якості в реальному часі з використанням комп'ютерного зору та довгострокове відстеження продуктивності для постійного вдосконалення стандартів.*

Ключові слова: *3D-друк бетоном; управління проєктами; нормування часу; класифікація складності; забезпечення якості; виявлення дефектів.*

CONTENT

Scientific edition

CUTTING AND TOOLS
in technological systems

Collection of scientific papers

Issue No 103

Compiled by *Doctor of Technical Sciences, Prof. I.M. Pyzhov*
Original-model *by A.M. Borzenko*
Responsible for the graduation *of Candidate of Technical Sciences, Prof. Y.V. Ostroverkh*

In the author's edition

Materials reproduced from the author's originals

Subpara. to print 10.12.2025.Format 60x84 1/16. PaperSoruRareg.
Printing - risography. The Times Typeface. Conditions.print.p. 10,93. Accounting.vid.ark. 11.0.
Circulation 30 copies.
1st Plant 1-100. Deputy. № 1149. The price is negotiable.

Publishing Center of NTU "KhPI"
Certificate of state registration DK No. 116 dated 10.07.2000
61002, Kharkiv, st. Kirpichova, 2